Aslak Skjeldestad

Electrode paste behavior in Søderberg electrodes in ferroalloy production

Aslak Skjeldestad

Doctoral thesis

NTNU
Norwegian University of Science and Technology
Thesis for the Degree of
Philosophiae Doctor
Faculty of Natural Sciences
Department of Materials Science and
Engineering

NTNU
Norwegian University of
Science and Technology

NTNU
Norwegian University of
Science and Technology

NTNU

Aslak Skjeldestad

Electrode paste behavior in Søderberg electrodes in ferroalloy production

Thesis for the Degree of Philosophiae Doctor

Trondheim, November 2019

Norwegian University of Science and Technology
Faculty of Natural Sciences
Department of Materials Science and Engineering

NTNU
Norwegian University of
Science and Technology

PREFACE

This work has mainly been carried out at the Department of Materials Science and Engineering at the Norwegian University of Science and Technology (NTNU), and at Elkem Carbon in Kristiansand. The industrial measurements were carried out at Eramet Norway. The work is part of an industrial PhD funded by the Research Council of Norway and Elkem Carbon.

ACKNOWLEDGEMENTS

ABSTRACT

The main goal of this work has been to study the melting behavior of electrode paste used in Søderberg electrodes in ferroalloy production. It has been done by first measuring temperatures in an industrial electrode and identifying the temperature profiles the electrode paste goes through before baking. In the second part flow of electrode paste has been studied in a parallel plate viscometer.

Long thermocouples were used to measure the temperature in steel cylinders following the electrode casing, from a couple of meters above the molten paste level down to below the contact clamp tip. The temperature measurements show that the molten paste has a temperature of 80° C, and that temperatures of up to 280° C are reached above the contact clamp. The high temperatures above the contact clamp are caused by induced currents from the current tubes coming close to the electrode casing before entering the contact clamps.

A COMSOL model was used to model the effect of increased heating above the contact clamps, where after the model was compared to the experimental temperature measurements done. The model shows that by reducing the induced heating from the current tubes, the temperatures can be significantly lowered in the area above the contact clamps. Installing copper shields or increased flow of electrode air can be used to reduce the heating from induced currents in casing.

The flow measurements in the parallel plate viscometer showed that electrode paste is a non-Newtonian liquid with shear thinning characteristics in the temperature range 20-80° C. The electrode paste starts to flow at temperatures 25° C below the softening point of the binder. The electrode pastes tested in this work reach half the original height at around 75° C.

The viscosities measured in the parallel plate viscometer are apparent viscosities as many of the assumption in the underlaying equations are not followed in the measurement set-up used. Among other things the shear rate varies during measurements and is not even throughout the sample. Thus, apparent viscosity found in this work is only applicable under the same conditions as the experiments done, but can be used, with awareness of the measurement limitations, in industrial electrodes as measurement conditions are close to what is observed in industrial electrodes.

A mix of coal-tar pitch and fines were found to behave non-Newtonian liquid behavior above 30 % addition of anthracite fines. Increased fines content increases the viscosity of the mix and at 73% fines content the system is "locked" and does not flow.

The influence of coarse particles on electrode paste flow has also been studied in the parallel plate viscometer, where increased coarse content was found to increases apparent viscosity. Apparent viscosity of electrode pastes with more than 60 % coarse particles are heavily influenced by particle-particle interactions, as apparent viscosity does not increase much with more addition of coarse material. Paste with 70 % coarse particles have very little flow up to temperatures of 120 °C.

CONTENTS

CHAPTER 1   INTRODUCTION

Using Søderberg electrodes is an efficient way of adding energy to metal producing processes, and hence Søderberg electrodes are used in numerous different processes such as production of ferrosilicon, ferromanganese, ferrochromium, platinum, and nickel matte. The furnace process and temperature will be different for each process, and the Søderberg electrode is robust enough to handle the range of different process environments.

Around the turn of the nineteenth century, the pre-baked carbon electrodes used in metal production had to be replaced by stopping and cooling the furnace. Thus, the use of a continuous process for replacing consumed electrode in the furnace process was sought after. When the Søderberg electrode was invented in 1919 (Søderberg [1]) it made it possible to continuously produce metals in an electric furnace. The Søderberg electrode is made from an electrode paste, which is a mixture of carbon aggregates (anthracite, coke or scrap graphite) and a binder (coal-tar pitch). The electrode paste is added into a steel casing on top of the electrode as cylinders or briquettes. As the electrode is consumed, the casing with electrode paste moves towards the furnace, and the electrode paste is gradually heat-treated as it is lowered. The solidification of the electrode paste into a solid carbon body is called baking, an in a typical Søderberg electrode the electrode is predominantly solid at 475° C.

Another advantage of the new Søderberg self-baking electrode was that they offered an increase in electrode diameter, with Søderberg electrode diameters of up to 850 mm compared to prebaked electrodes of 650 mm at the time of commercialization of the Søderberg electrode. As technology has evolved over the years, the diameter of Søderberg self-baking electrodes can now be over 2000 mm and transformer capacities up to 120 MVA (Larsen, et al. [2]). The increase in diameter and load requires a better understanding of the Søderberg self-baking process, as this knowledge is critical to avoid electrode breakages.

Investigations of electrode breakages by Nelson and Prins [3] and Ord, et al. [4] show that poor understanding of temperature and raw materials addition in the upper part of the electrode can lead to breakages. Nelson and Prins [3] found that excessive temperatures and increased pressure from raw materials cylinders could cause segregation in the electrode paste, which would make a weak electrode. Ord, et al. [4] used computer modelling to prove that electrode paste temperatures in the contact clamp area needs to be stable to ensure a good transition from electrode paste to solid carbon electrode. A good understanding of the influence of electrode equipment on temperatures, and how electrode paste properties change under these conditions is important to achieve control of the electrode process.

1.1. SØDERBERG SELF-BAKING ELECTRODE

One of the reasons for the successful invention of the Søderberg electrode in 1919 was the use of fins in the steel casing (Søderberg [1]), as can be seen in Figure 1-1 marked as 1. The fins anchor the paste to the casing, increase heat transfer to the center of the electrode during baking, and distribute current into the baked electrode. As the electrode is consumed it needs to be lowered into the furnace, and this is done by two hydraulic or pneumatic slipping rings (2), which move and open/close independent of each other to lower the electrode into the furnace. Moving the electrode into the furnace is called slipping.

Further down the electrode column, fans (3) blow heated air alongside the casing, inside the suspension mantle (4) to start heating the electrode paste. In some furnaces (e.g. FeSi, FeMn), the air that in the upper part of the electrode is heating the paste, will cool the paste in the area above the contact clamp as the paste is heated. Depending on the furnace the air will exit somewhere in the area of the contact clamps (6). The current enters the electrode via current tubes (5), which comes from the transformers, and goes down into the contact clamp. The paste is added as either cylinders, blocks or briquettes (7), then melts (8), before it bakes to a solid carbon body (9) in or below the contact clamps, depending on the ferroalloy melting process.
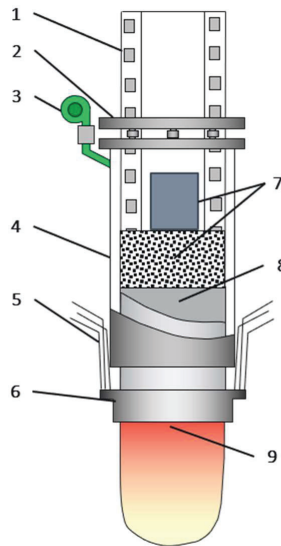
Figure 1-1: Illustration of the Søderberg electrode with numbering of the most vital parts, adopted from Schei, et al. [5]. The electrode equipment is shown to the left, as casing (1), slipping rings (2), air fan (3), suspension mantle (4), current tubes (5) and the contact clamps (6). The different stages of paste is numbered to the right, as electrode paste added as either briquettes or cylinders (7), molten paste (8) and the baked paste (9) as the electrode leaves the contact clamps.

The paste is heated by two mechanisms; the electric current entering the steel casing and fins at the contact clamps, and the heat conducted by the electrode from the furnace. The electrode paste softens as it heats and will fill the whole casing between 50-100 °C. As temperature increase the coal-tar pitch (or other binder) will lose volatiles and carbonize, and the paste is finished baking to a solid carbonaceous body at about 475 °C (Shoko, et al. [6]). At the baking isotherm, the electrode paste is transformed to a self-sustaining carbon body, which will be able

to carry the current into the furnace. Green electrode paste is thermally and electrically non-conductive, however after baking the thermal and electrical conductivity increases with heat treatment.

The electrode should be slipped in small increments to keep the baking isotherm well inside the electrode holder area, and to keep the baking process as constant as possible. For optimum electrode baking, electrode movement should be kept as small as possible. Nevertheless, as the electrode tip position is governed by metallurgical conditions in the furnace process zone, movement of the electrode column is vital for the furnace process. The operating conditions of a ferroalloy furnace will influence the baking conditions and in the end affect the electrode quality (McDougall [7]). Furnace shut-downs causes most electrode failures, however with good operating procedures breakages can be avoided or minimized (Larsen, et al. [2]). If the electrode breaks, long slips are usually required to lengthen electrode. After a long slip, the electrode must run on reduced current to avoid the current burning through the steel casing as the carbon paste bakes to form a new solid carbon electrode.

1.2. CARBON ELECTRODE PASTE

Carbon pastes are used extensively in the metal producing industry, as e.g. in anodes and cathodes in aluminum electrolysis cells, graphite-, prebaked-, and Søderberg- electrodes in electric arc furnaces, and graphite crucibles. In Norway, Alcoa produce Søderberg anode paste at Lista and prebaked anodes in Mosjøen, Hydro produce prebaked anodes for their smelters and Elkem Carbon produces Søderberg electrode paste. The use of carbon artifacts is large, as most metal producing furnaces use some of the products mentioned above.

The production of the carbon paste is quite similar for all of the above, i.e. a carbonaceous filler and binder is mixed to produce the "green" paste, where a green paste is a paste which has not been heat-treated yet. The filler is carbon particles, such as calcined petroleum coke or anthracite, anode butts, or scrap graphite, which is crushed and sieved into several different particle size fractions. The different fractions are weighed according to a recipe to give the density and/or flow properties desired for the carbon paste. One of these fractions is the fines fraction, where at least 50 % of the particles are below 100 µm. The size of the biggest particles depends on the product but is usually in the range of 10 mm in diameter. The binder used for carbon artifacts in the metal producing industry has historically been coal tar pitch, a byproduct from the production of metallurgical coke. Other binders are petroleum pitches and resins, but for Søderberg electrode paste coal-tar pitch is the preferred binder. Raw materials and binder content are listed for some carbon products in Table 1-1. Note that the binder amount in Søderberg type applications are higher than the pre-baked products, as the Søderberg pastes must flow and fill the casing before baking takes place.

Table 1-1: The raw material fillers and binders of different carbon pastes, adopted from Foosnæs and Naterstad [8]. ECA – electrically calcined anthracite, TCA – thermally calcined anthracite, TCC – thermally calcined petrol coke, SG – synthetic graphite.

Carbon Product	Filler	Binder	Binder content (%)
Søderberg anode paste	Petrol/Pitch coke	Coal tar pitch, Petroleum pitch	26-33
Prebaked anode paste	Petrol/Pitch coke	Coal tar pitch, Petroleum pitch	13-18
Søderberg electrode paste	ECA, TCA, GS, TCC	Coal tar pitch	18-30
Graphite electrodes	SG, Petrol/Pitch coke	Coal tar pitch	14-18
Ramming pastes	ECA or TCA & SG	Pitch, Tars, Synthetic Resins	12-20

A flow chart of the production of carbon products for the metal producing industry is shown in Figure 1-2, starting with the raw materials and going through mixing, heat treatment and graphitization for the graphitized products. Products are marked with dashed lines, and the products for Søderberg electrodes and Søderberg anodes are the only ones who are made without a heat treatment of the green carbon body. Graphitized products may go through a second heat treatment after pitch impregnation to increase the density of the finished product.

Properties of electrodes in the metal producing industry are listed in Table 1-2. The graphitized electrodes have superior electrical- and thermal conductivity, and higher mechanical strength, but a higher cost, thus the choice of electrode is governed by the metal producing process and its requirements. In ferroalloy production, the Søderberg electrode is usually preferred.

Table 1-2: Typical properties of electrodes in ferroalloy production, data from McDougall [7].

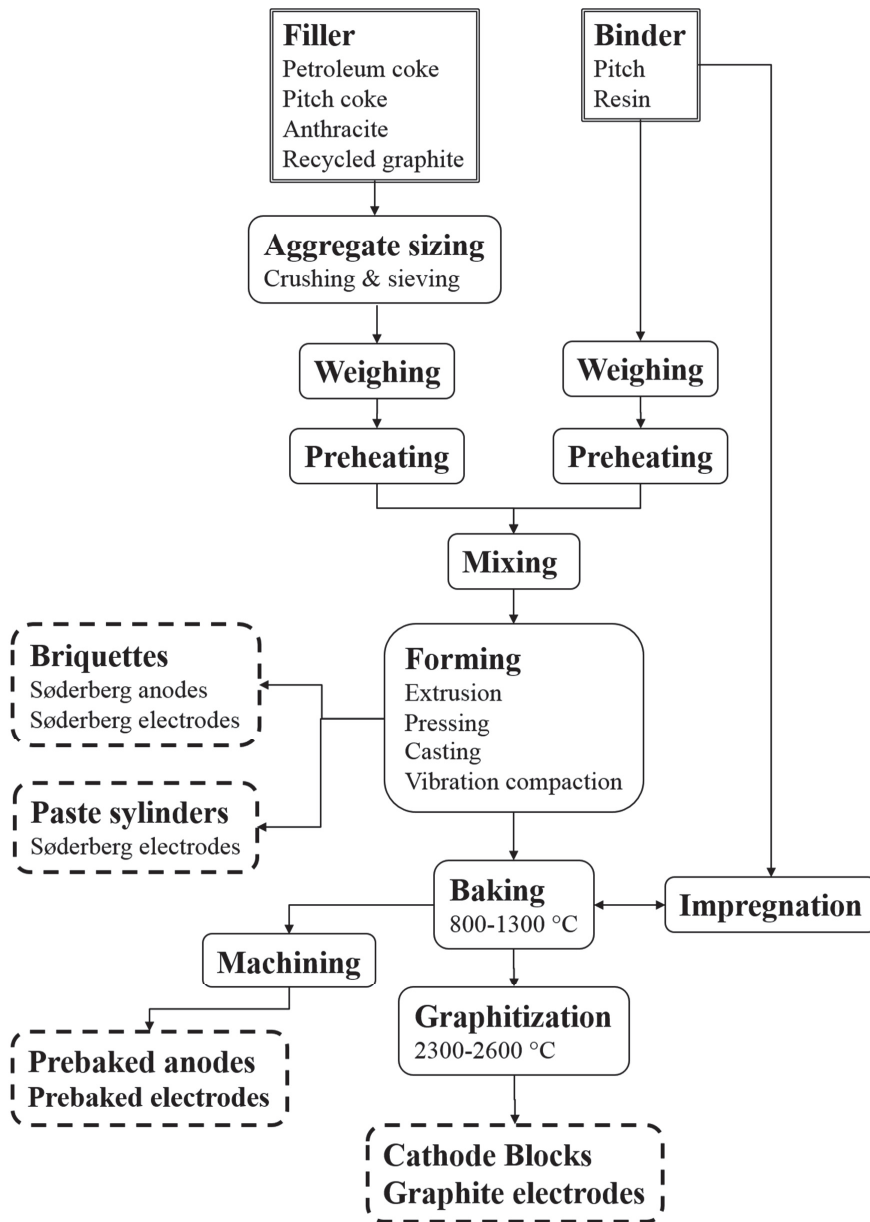| Electrode	Diameter [mm]	Electrical resistivity [$\mu\Omega m$]	Current Carrying Capacity [kA]	Maximum Current Density [A/cm^2]
Søderberg electrodes	700-2200	70	30-150	7
Prebaked anthracite electrodes	700-1400	37	30-100	9
Semi-graphite electrodes	700-1000	29	36-70	11
Graphite electrodes	550-700	5	65-146	28

Figure 1-2: Flow chart for manufacturing of carbon artifacts used in metal production, inspired by chart in Foosnæs and Naterstad [8].
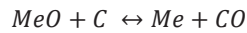
1.3.FERROALLOY PRODUCTION

Ferroalloys are alloys where iron is one of two or more metals, where the most common alloying elements are Mn, Si and Cr. The most abundant element, except iron, is commonly called the leading element. A list of the most conventional ferroalloy elements is given by Jalkanen and Gasik [9] and include Ca, Ba, Sr, and REM (Rare Earth Metals) among many others. Steelmakers use about 85-90 % of the ferroalloys produced and are by far the biggest consumer. Nonferrous alloys (e.g. nickel and titanium based) and the chemical industry are the other major consumers of ferroalloys. In Norway, the two most common ferroalloys produced are FeSi and FeMn (SiMn). FeSi is produced by Finnfjord and Elkem, whereas FerroGlobe and Eramet produce FeMn and SiMn. The FerroGlobe plant in Mo i Rana previously produced FeCr, showing that the production of some ferroalloys can be interchanged (Tangstad [10]).

There are usually a number of reasons why the leading element is produced as a _ferro_alloy; the first is where the leading elements are found in nature as ores containing large amounts of iron (among other elements). As iron is reduced before chromium and manganese, and chromium and manganese ores contain iron, the iron content of the ferroalloy is determined by the iron content in the ore. Secondly, the FeMn and FeCr are most widely used in the production of steel, there is no point in removing excess iron. In addition, scrap iron, iron oxide pellets or mill scale are sometimes added to facilitate the reduction process (e.g. FeSi). Also, adding iron may reduce the melting point (e.g. ferrotungsten and ferromolybdenum according to Rosenqvist [11]), reduce activity and help the dissolution of the leading element (Jalkanen and Gasik [9]). Lastly, ferroalloys are produced because it is cheaper to add 1 kg of an alloying element as ferroalloy in steel if compared to the pure form.

As most ferroalloys are used as alloying elements and deoxidizing agents in steel production their history is tied to the history of steel. "Iron age" steel was produced through direct reduction at low temperatures and the iron was formed in the solid state, thus no alloying elements were added. The blacksmiths of the time used carburizing/decarburizing treatments to adjust the only alloying element of the time, carbon. As the blast furnace was discovered in the medieval age in Central Europe, the carbon-saturated iron melted in the process. The cast iron contained small percentages of silicon and manganese, depending on the ore composition. The next breakthrough came with the Bessemer process, where Henry Bessemer in 1855 understood that oxygen in air blown into the hot carbon rich metal burned the dissolved carbon. Around the same time, Robert Mushet discovered that addition of the manganese-containing ferroalloy spiegeleisen prevented "boiling" in the steel melt. The "boiling" observed was carbon-oxygen reaction forming CO gas, and thus manganese was used as a deoxidation agent in steel (Holappa [12]). Production of ferroalloys started in small-scale graphite crucibles, where coal and ores where heated to high temperatures to get FeCr and FeMn alloys. As early as 1826, Prieger produced 80 % FeMn in this way (Tangstad [10]). Later in the 19th century FeMn, FeSi and low-content FeTi and FeV where produced in blast furnaces. However, as the electric furnace was developed most ferroalloys were produced by electric smelting, and the first electric arc FeSi furnace was started in 1907 by Paul Héroult in United States (Tangstad [13]).

Most ferroalloys are produced by reducing the oxide ores with carbon, in a carbothermic reaction at temperatures above 1000 °C. Usually the reaction can be expressed by the equation

$$MeO + C \leftrightarrow Me + CO$$

where Me is the leading metal.

1.4. SØDERBERG ELECTRODES IN FERROALLOY PRODUCTION

Søderberg electrodes are used in most ferroalloy furnaces, however the furnace processes vary. In this section, three different processes will be considered to show the different conditions the electrode experience. The ferronickel process is an example of a slag furnace, whereas the in FeMn production the electrode connects to a coke bed, and in FeSi production, an electric arc is present. The differences in electrode consumption is listed in Table 1-3, where the high silicon FeSi production is by far the highest consumer by produced metal.

Table 1-3: Søderberg electrode consumption in different ferroalloy processes; from Elkem-Carbon [14]

Ferroalloy	Electrode consumption [kg/ton metal]
FeSi 90	120-130
FeSi 75	45-55
FeMn	12-14
SiMn	25-30
FeCr	15-25

In FeNi production from laterite type (oxide-silicate) raw materials, the nickel content varies from < 1% up to 3%. Calcination of the nickel ore with limestone, coal and recycled dust is done at about 800 °C in a rotary kiln or rotary drum furnace. The hot calcine is then transferred to the closed electric furnace. Decomposition of crystalline water, hydroxides and carbonates in the calcination save energy and lowers electrode consumption caused by reduction off H_2O and CO_2.

The electric furnace can be operated in two modes, as either a shielded arc or an immersed-electrode. In immersed electrode smelting, shown in Figure 1-3, the electrode is immersed in the slag and the heat is produced by the current going through the slag (resistive heating). The electrode will be heated by the slag and furnace gasses above the calcine. In the shielded arc mode, the electrode is kept above the slag and an arc goes from the electrode into the slag. The arc will heat the slag, the calcine and the electrode. The baking isotherm is usually somewhere around the roof of the furnace for both modes of operating. Since the clamps are above the baking isotherm, the casing must carry the current from the clamps to the baked electrode below

the roof. The electric power of the furnace is limited by the current carrying capacity of the steel casing.
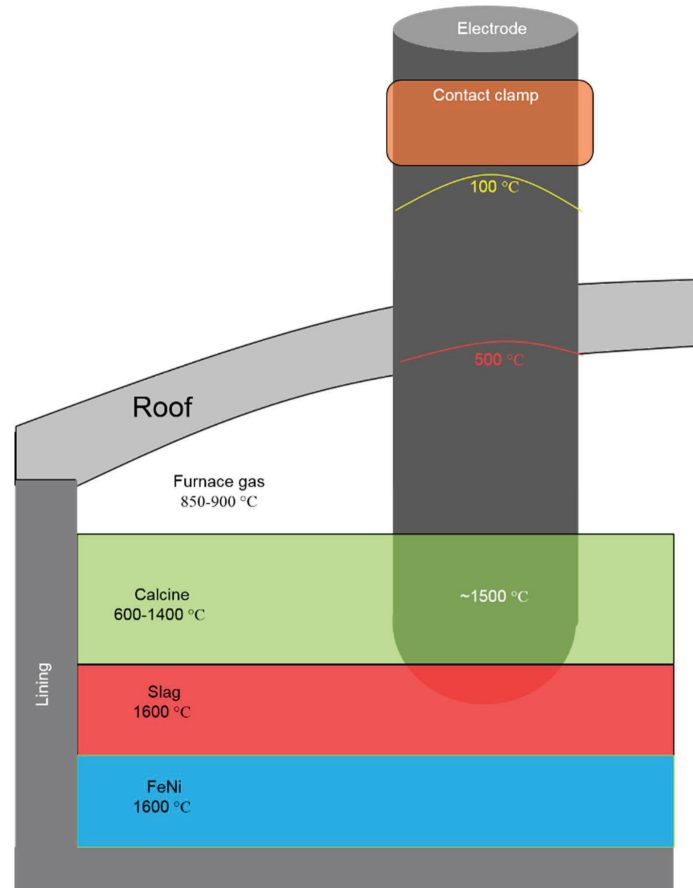
Figure 1-3: Sketch of the FeNi slag process with conditions around the electrode

Ferromanganese is usually produced in a circular three-phase closed AC submerged electric furnace. The industrial ferromanganese furnace is usually divided into two different zones, the pre-reduction zone and coke-bed zone. In Figure 1-4, the pre-reduction zone can be seen to the left of the electrode where CO gas go up and raw materials down. In the pre-reduction zone, the higher manganese oxides are easily reduced by the ascending CO gas seen in Figure 1-4. Complete reduction of iron oxides may take place parallel to reduction of the manganese oxides. In the coke-bed zone shown in Figure 1-4 as the grey area below the electrode, the manganese oxide (MnO) will react with the coke to produce manganese metal according to reaction shown in the figure.
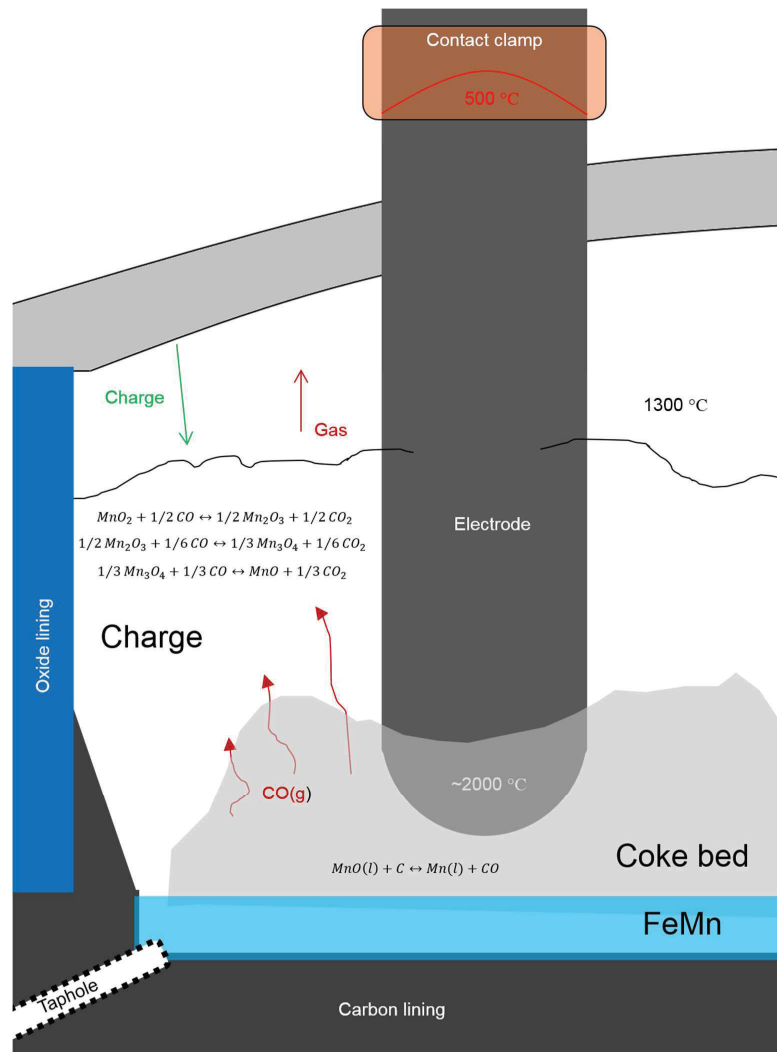
Figure 1-4:Sketch of the FeMn process with conditions around the electrode and some of ore reducing reactions.

The reduction will start when the slag, coexisting with solid MnO phase, is sufficiently fluid and enters the coke bed. The temperature for which the slag is viscous enough to enter the coke bed depends on slag chemistry, which in turn is dependent on raw materials chemistry. The metal producing reaction is endothermic, and consume some of the electric energy supplied. The heat is produced by the resistive heating in the coke bed as the current go from the electrode to the cokebed. The electrode is heated by the heat in the furnace and the off-gases. However, the electrode paste has baked to a solid carbon electrode as the electrode leaves the clamps. The resistive heating from the current in the electrode just below the clamps will also supply energy for electrode baking.

Ferrosilicon and metallurgical grade silicon are produced in similar furnaces to FeMn, however the furnaces are usually open or semi-closed due to mechanical feeding of raw materials (stoking). The open furnace lets air in at the top, and the top of the furnace will be quite hot with a high oxygen pressure. The contact clamp is usually shielded to minimize heating and dust/particle settling between the contact clamps and electrode.

The overall chemical reactions in a silicon furnace can be expressed with the simplified carbothermic reduction reaction

$$SiO_2 + 2\,C \leftrightarrow Si + 2\,CO$$
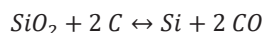
However, the chemical reactions happening in the furnace is more complicated as both SiO gas and SiC forms stable compounds in the temperature range of the furnace. The reactions in the high temperature zone are often described by the unbalanced equation shown below the electrode in Figure 1-5. Addition of too much carbon to the charge, i.e. overcoking, will lead to production and accumulation of SiC in the high temperature zone. Adjusting the fixed carbon (carbon content) is hence one of the key parameters in industrial silicon furnaces as the goal is not to produce any excess SiC in the lower zone of the furnace. In Figure 1-5, the cavity around the electrode is shown with approximate temperatures and structure of the furnace. The SiO gas produced in the crater will move upwards and react with the carbon in the charge material and form SiC. The SiO gas may also condensate to produce silicon and silica, as shown in reaction equations in Figure 1-5. The crater shown in Figure 1-5, is formed as the charge material move down and quartzite starts to melt around 1700 °C. The melt is mixed with SiC, formed by the SiO gas reacting with the carbon in the charge, and the solids from the condensate reaction of SiO. This mixture will behave as a bridge in above the crater and stop raw materials moving down. FeSi and Si furnaces are therefore stoked on a regular basis to break up these bridges and let new raw materials enter the lower parts of the furnace.

In ferrosilicon production, there is an electric arc supplying heat to the silicon producing reactions. The arc is very hot, ~ 20 000° C, thus heat is transferred to the electrode tip. As in FeMn furnace the electrode is baked to solid carbon as it leaves the contact clamps and the heat required for baking comes from the heat in the furnace and the resistive heating in the carbon electrode.

In ferrosilicon production, Søderberg self-baking electrodes are used, but in production of silicon, the steel casing of the Søderberg electrode contaminate the silicon and cannot be used. For smaller furnaces, a prebaked electrode is commonly used, and for larger furnaces, the composite electrode is used. The composite electrode, invented by Persson [15], consists of a graphite core, within a steel casing without fins, and carbon electrode paste in between the casing and core. The graphite core and baked carbon electrode is slipped independent and quicker (up to 100 cm/day) than the steel casing (3 cm/day), thus reducing the iron in the metal coming from the electrodes from 1.5 % to 0.05 %. Even with improvements in the prebaked electrodes and new electrode concepts (e.g. composite electrodes), Søderberg self-baking electrodes are still the preferred technology for ferroalloy production, mainly due to cost.
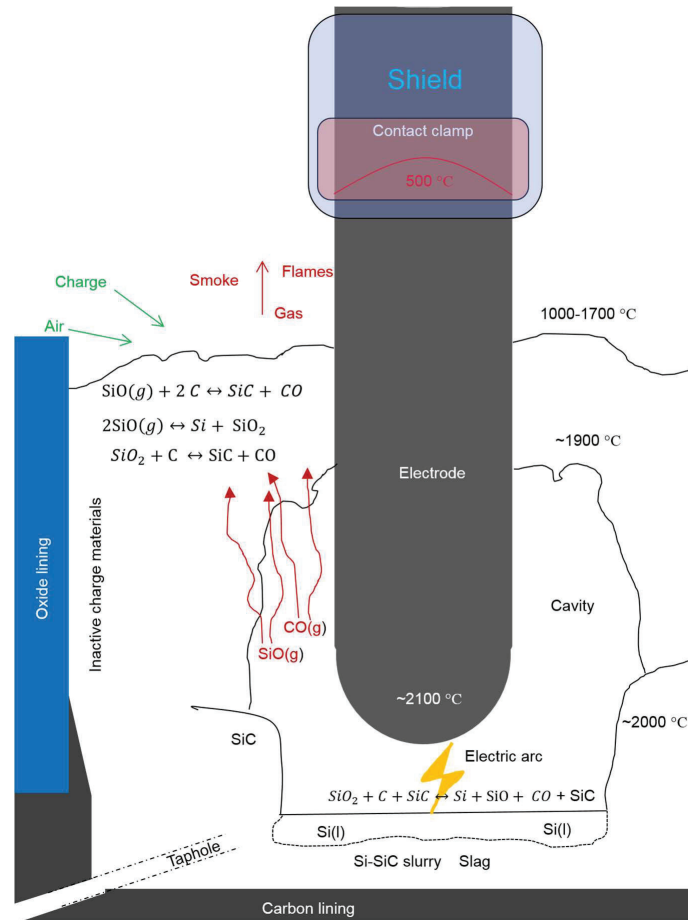
Figure 1-5: Sketch of the (Fe)Si process with conditions around the electrode and the reduction reactions creating silicon.

1.5. GOALS AND OUTLINE OF THESIS

Electrode problems, such as breakages and spalling, limit the efficiency of a ferroalloy producer. Segregation of electrode paste is often mentioned as a factor that can cause failures of the electrodes. The top of the electrode paste is thus inspected from time to time to check for signs of segregation. One such sign could be liquid paste as seen in Figure 1-6, where the briquettes in center rests on a paste cylinder and the paste close to the casing seems liquid. Temperature measurements on the electrodes in a circular three-phase furnace can help find underlying causes for the liquid paste problem on one of the electrodes. By measuring temperatures along the ribs of the casing, the impact of electrode equipment on temperatures above the contact clamp can be found. Measurements will be compared with computer models, and the models will quantify the heating/cooling affects from e.g. cooling water or heating air.
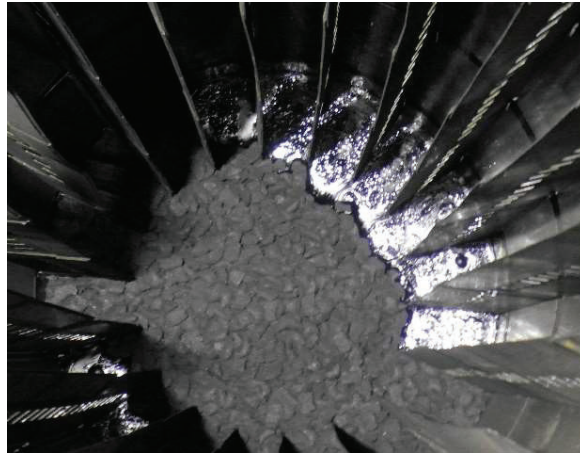
Figure 1-6: Molten electrode paste on top of a Søderberg electrode

A better understanding of how the electrode paste softens and fills the electrode casing will give insights into how to avoid liquid paste on the top of the electrode. By first knowing the temperatures in an industrial electrode, the temperature range for how the electrode paste softens is known. The apparent viscosity of electrode pastes can then be measured at temperatures, temperature gradients, and pressures similar to that of an industrial electrode. The calculation of viscosity of pastes with large particles is non-trivial, therefore simplifications are needed to calculate an apparent viscosity. By comparing different electrode pastes, the influence of coarse particles on paste flow will be determined.

In the following chapter, the basic theory of carbon materials will be presented with a focus on materials used in electrode paste. The basic theory for rheological measurements on pastes will be given, with a literature survey on rheological measurements of carbon materials as a part. In chapter 3 result from measurements of temperature in an industrial FeMn furnace will be given, with a discussion and conclusion of the results. Computer modelling will be a vital part of the discussion of the results in this part. Rheological measurements of carbon pastes will be presented in chapter 4, with a description of methods used and discussion of results. All laboratory scale tests are presented in this chapter. To sum up the thesis the main conclusions will finalize the thesis in chapter 5.

CHAPTER 2   THEORETICAL BACKGROUND

2.1.CARBON

Carbon is one of the most versatile elements in the periodic table with respect to bonding to itself and other chemical elements. The reason for its versatility in chemical bonding is the ability to form sp^3, sp^2 and sp^1 hybrid bonds. For more on hybridization the reader is referred to standard inorganic chemistry textbooks, e.g. Shriver and Atkins [16]. The different hybridization of carbon can be illustrated with the three organic molecules ethane (C_2H_6 - sp^3), ethylene (C_2H_4 - sp^2) and acetylene (C_2H_2 - sp^1). In ethane, a σ bond is formed between the two carbon with one of the sp^3 orbitals, and three σ bonds are formed with three hydrogen atoms for each carbon with the remaining sp^3 orbitals. In ethylene, the carbon atoms form a σ bond with each other with one of the sp^2 orbitals and a π bond with the remaining p-orbital. Since the sp^2 orbitals are coplanar and oriented 120° to each other, the hydrogen atoms will be bound to the carbons in a plane. In sp^1 hybridization, the two carbon atoms form a σ bond with the sp^1 orbitals, and two π bonds with the hybridized p-orbitals. The hydrogen atoms bond to the remaining sp^1 orbital making the acetylene molecule linear.

The three different hybridizations of carbon also make different crystalline forms of carbon, where diamond (sp^3) and graphite (sp^2) are the most known allotropes. Fullerenes, carbon nanotubes and latest graphene have in recent years become well known with Nobel prizes in Chemistry (1996 – Fullerenes) and in Physics (2010 – Graphene). Graphene is a one-layer two-dimensional sheet of sp^2-hybridized carbon, and carbon nanotubes can be regarded as the 1D rolled up form of graphene (Wallace, et al. [17]). Fullerenes are a graphene sheet wrapped to form a ball, e.g. C_{60} – the football molecule. Carbynes is an allotrope of carbon with sp^1-hybridization, but since production of carbynes have been very limited they have not been characterized as much as other carbons (McEnaney [18]).

As diamond is sp^3 hybridized each carbon atom is connected to four other carbon atoms in a tetrahedral configuration. The carbon tetrahedrons can be arranged in two different structures, where the base triangles in two neighboring tetrahedrons are placed directly on top of each other (hexagonal) or one is 60° rotated on the other (cubic). Most diamonds crystals are cubic. The strong covalent bonds between carbon atoms make diamonds very hard, electrically insulating and a high thermal conductivity. Thermodynamically diamonds are not stable at room temperature as the reaction

$$C_{diamond} \leftrightarrow C_{graphite}$$
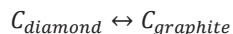
has a ΔG^0 of – 3 kJ/mol. In this work the more graphite like carbons are of interest.

2.1.1.   GRAPHITE

Graphite deposits in nature are found as big pieces, in flakes or as powders. The concentration of graphite in these deposits range from 20-50 %, and further processing is determined by the type of deposit and graphite concentration. Several steps of crushing, milling and floatation is usually done to separate graphite from the rock, and in some cases chemical methods like hydrochloric- or hydrofluoric acids are used. Norway has a large producer of natural flake graphite, Skaland Graphite, that produced about 9000 tons in 2013, or about 2 % of the world's production of natural graphite. Graphite is used in processes like electrodes for arc furnaces, cathodes in aluminum production, crucibles in metallurgical industry, anodes in Li-ion batteries, and moderators in nuclear reactors.

In graphite, graphene sheets are stacked either in an ABABAB hexagonal stacking or in an ABCABC rhombohedral stacking (Edwards [19]). The hexagonal structure is the more stable of the two and the rhombohedral structure transforms to hexagonal structure above 2000 °C.

In graphite, the sp^2 hybridized carbon is connected to three other carbons with σ bonds and a delocalized π bond from the p_z-orbital (Bourrat [20]). The bond length of 142 pm within the graphene sheet is between the bond length of the sp^3 hybridized carbon-carbon bond in ethane (153 pm) and the sp^2 hybridized carbon-carbon bond in ethylene (132 pm) . Consideration of the resonance structure between carbon atoms in the graphene layer show that the carbon-carbon bond has about one-third double bond character (McEnaney [18]). The bonding between layers is of the weak van der Waals type and the distance between the graphene sheets is 335 pm. The delocalized π electrons make graphite a good conductor in the xy-plane (parallel to the graphene sheets), but along the z-axis the electronic conductivity is like an insulator as electrons cannot move across the "gap" between graphene sheets. Graphite properties, in both xy- and z-direction is shown in Table 2-1 and show the anisotropic nature of graphite.

Table 2-1: Anisotropic features of graphite, data from Krueger [21] and Bourrat [20]

Property	Parallel to xy-plane	Parallel to z-axis
Electrical resistivity [μΩm] [20, 21]	0.4 – 0.5	200 – 1000
Thermal conductivity [W/m·K] [20, 21]	3000	6
Thermal expansion [·10^{-6} K^{-1}][20]	-1	29
Hardness [Mohs][21]	1	4,5
Elastic moduli [GPa] [20]	1060	36,5

Commercial graphite materials consist of many grains, which are composed of crystallites of graphitic units, therefore the material is often called polycrystalline graphite. As the crystallites are highly anisotropic, the properties of the graphite material will depend on the statistical distribution of grains and crystallites within the grain. The bulk properties will be governed by the alignment of grains and texture within the grains, and the thermal history (heat treatment temperature) of the polycrystalline graphite. Inagaki [22] has listed the characteristics of polycrystalline graphite as follows;

- High thermal resistance in non-oxidizing atmosphere
- Chemical stability
- Non-toxic, biocompatible
- High electrical and thermal conductivity
- Small thermal expansion and high thermal shock resistance
- Low bulk density; light weight
- Mechanical strength at elevated temperatures
- High lubricity
- Reductive at high temperatures, dissolves in iron
- Radiation resistant
- Low absorption cross-section and high moderating efficiency of neutrons

The thermal expansion coefficient is very anisotropic, as seen in Table 2-1, with a negative value within the graphene plane from room temperature and up to around 500 °C. The thermal expansion anisotropy of crystallites will be spatially averaged in graphite materials and depends strongly on the arrangement and size of crystallites. The thermal expansion in graphite fibers is governed by the expansion along the layer planes and is rather small. As mechanical properties are very texture sensitive, graphite materials will have large variations. The measured mechanical properties of polycrystalline graphite will be inferior to the theoretical value of the graphite layer, part because of difference in grain orientation and by various defects such as grain boundaries.

The natural graphite production is not large enough for the demand and synthetic graphite is produced in large amounts. In the graphitization process, carbon-containing raw materials are heat treated to temperatures up to 3000 °C. To understand graphitization, knowledge of the crystal structure of graphite is needed, and x-ray diffraction is usually used to find graphite lattice parameters such as d_{002}, L_c and L_a. In x-ray diffraction the monochromatic x-rays are scattered by the atom lattice and according to Bragg's law the distance between two atomic layers (e.g. the distance between two graphite sheets, d_{002}) can be found by the equations; (from Bragg and Bragg [23])

$$n\lambda = 2d_{hkl}sin(\theta) \qquad \text{(2-1)}$$

Where n is the order of reflection, λ the wavelength of the x-ray, *hkl* the miller indices and θ the angle of the incoming x-ray. The crystallite sizes (L_a and L_c) can be found using the Scherrer equation. The Scherrer equation (from Scherrer [24] and Patterson [25]) relates the full width at half maximum intensity (FWHM) with the wavelength, λ, the diffraction angle and the crystallite size.

$$L = \frac{K_S\lambda}{(FWHM)cos(\theta)} \qquad \text{(2-2)}$$

K_S is a constant. A standard for x-ray diffraction measurements on carbon materials is given by Iwashita, et al. [26], among the points is that L_c should be calculated both from the 002 and 004 reflection and an internal silicon standard should be used. With knowledge about the crystal structure of graphite, the changes in structure in carbons during heat treatment can be examined.

Warren [27], one of the pioneers in studying carbon structure, found layer planes of graphite-like structure in carbon black by applying Fourier transforms to the x-ray diffraction patterns. Later, Biscoe and Warren [28] showed that the graphite like layers in carbon black are stacked in parallel groups, but lacking any common orientation. These groups were called turbostratic, and when examined with x-ray diffraction only the 00*l* peaks and *hk0* bands give reflections. Since there is no trace of the *hkl* (l≠0) graphite lines, the three-dimensional structure of graphite is not present (Warren [29]). Bourrat [20] states that the minimum d_{002} distance in turbostratic carbons is 344 pm, compared to the pure graphite value of 335.4 pm.

Franklin [30] studied the evolution of graphitic structure with heat treatment and divided carbons into groups according to their ability to graphitize, see Figure 2-1. She showed that the non-graphitizing carbons do not develop any homogeneous three-dimensional graphite structure upon heat treatment up to 3000 °C. Examples of such carbons are oxygen-rich low rank coals, sugar charcoal and products from pyrolysis of polyvinylidenechloride. The non-graphitizing carbons do graphitize to some small extent with heat treatment, but is limited by the small geometrical domains with homogeneous orientation in the precursor carbon. Also cross-linking atoms such as Sulphur and Oxygen decrease the ability to graphitize (Oberlin [31]). The current understanding of graphitization is that three-dimensional growth only happens after the graphene layer have adopted near perfect two-dimensional structure. Inagaki and Kang [32] divide the graphitization process in two, one before d_{002} reaches 342 pm (pre-graphitization) and one after (graphitization), based on experimental results on cokes. Increase in L_a and L_c happens in the graphitization as d_{002} decreases towards the graphite interlayer distance of 335.4 pm.

Graphitizing   **Non-Graphitizing**
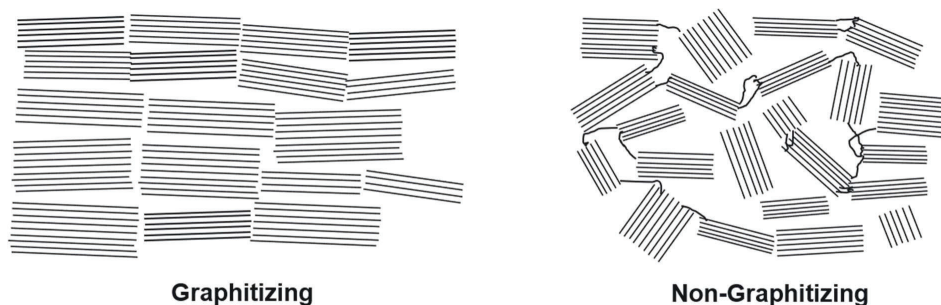
Figure 2-1: The illustration of graphitizing and non-graphitizing carbons redrawn from Franklin [30].

2.1.2.   ANTHRACITE

The carbon raw material for the filler in electrodes in ferroalloy production are usually anthracite or coke. Anthracite is a coal with high carbon content, relatively low ash and volatile matter. For commercial purposes coals are classified according to ASTM (American Society for Testing and Materials) by rank (ASTM [33]), and anthracite is ranked second. Fixed carbon is between 92% and 98% and volatile matter between 2 % and 8 % for anthracite. Another

important characteristic for anthracite is the ash content. The ash is the incombustible residue that remains after burning the anthracite to constant weight in air. Ash content should be low for anthracites used in ferroalloy production, as the ash will end up as slag in the produced ferroalloy.

Before anthracite can be used in electrode paste it is heat treated to become electrically conducting and remove volatiles. The anthracite is either gas calcined or electrically calcined, the difference being the source of heat to warm up the coal. Gas calcination reaches temperatures in the range 1400 – 1600° C, while electrical calcination is done in a shaft furnace with temperatures ranging from 1200 – 3000° C.
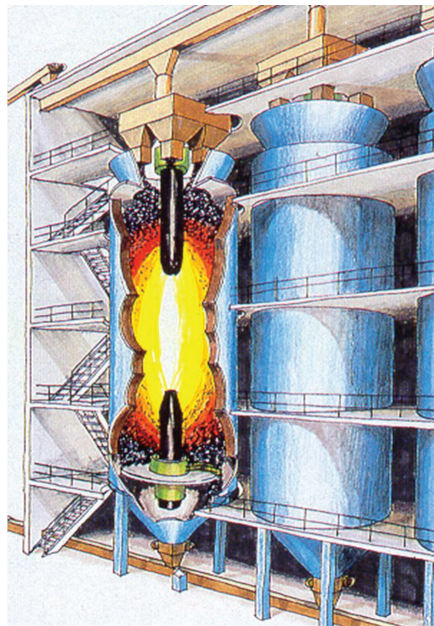
Figure 2-2: Electrical calcining of anthracite in shaft furnace, used with permission from Elkem Carbon

Anthracite was described by Franklin [30] as a semi-graphitizing carbon, meaning it will graphitize to some extent. In Figure 2-3 the anthracite structure is sketched, showing some cross linkage between graphite sheets. The anthracite structure is thus an intermediary between the graphitizing and the non-graphitizing structures in Figure 2-1. Up to 2000 °C anthracite does not graphitize, compared to graphitizing cokes. However, above 2500 °C the cross linkage in the anthracite can be broken and they will graphitize like graphitizing carbons. The electrical calcination will hence produce some anthracite that has been partially graphitized, while in gas calcination the anthracite will not have been graphitized.
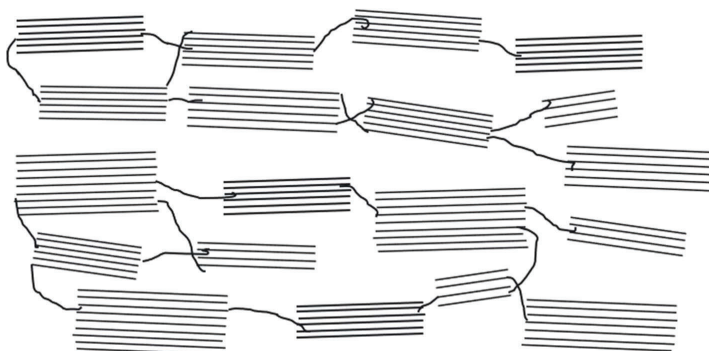
Figure 2-3: Representation of the structure of low-temperature anthracite char, redrawn from Franklin [30].

2.1.3.   PETROLEUM COKE

In aluminum anodes, petroleum coke is used almost exclusively as it is more easily graphitized and has a much lower ash content compared to anthracite. Petroleum coke can also be used in Søderberg electrodes, usually mixed with scrap graphite. Petroleum coke is produced in a process called delayed coking, where the residue from cracking of crude oils is fed to one of two drums at 485 – 515° C, and kept at $4 \cdot 10^5$ Pa for 16 – 24h. The product of this process is called a green coke, which has an apparently amorphous, very weak structure with 8 – 12 % hydrocarbon volatiles (Foosnæs and Naterstad [8]). The green coke is heat treated in a rotary hearth or rotary kiln calciner to 1250 – 1370° C to become an electrode grade coke. In this process, the volatiles are removed from the coke and properties like electrical conductivity and strength are improved.

In Table 2-2 some properties of raw/calcined anthracite and coke is shown. Notice that the heat treatment temperature of the anthracite is higher than that of the petroleum coke. The temperatures used are temperatures used in industrial calcination processes. The electrical resistivity of a petroleum coke heat-treated to the same temperature as an anthracite will be lower, as the petroleum coke is easier graphitized.

Table 2-2: Properties of anthracite and coke, data from Foosnæs and Naterstad [8].

	Anthracite	Calcined Anthracite (1800 °C)	Petroleum coke	Calcined Petroleum coke (1250-1350 °C)
Real density [kg/dm³]	1.4 – 1.6	1.72 – 1.85	1.5 – 1.8	2.0 – 2.13
Electrical resistivity[μΩm]	-	350-630	-	350-550
Volatiles [%]	6-13	-	6-14	< 0.3
Hydrogen [%]	2.3 – 3.7	0.03 – 0.3	3.0 – 4.5	< 0.1
Nitrogen [%]	-	-	0.1 – 0.5	< 0.1
Sulphur [%]	0.1 – 1.0	0.3 – 0.9	0.2 – 4.0	0.2 – 0.4
Ash [%]	3 – 12	3.5 – 11	0.04 – 0.5	0.04 – 0.6

2.1.4.   COLE TAR PITCH

Coal tar is a by-product from the production of metallurgical coke from coal for use in the blast furnace production of steel. In the coking process, the coal is heated to 1000 – 1200° C with a holding time of 14 – 20h. The yield of coke is about 75% and the yield of coal tar 3 – 4%. Water and chlorides are then removed before the crude tar is distilled to give coal-tar pitch. From 1 metric ton of coal about 15 – 20kg coal tar pitch is produced, (Menéndez, et al. [34], Madshus [35]). Coal-tar pitch is the distillation residue after naphthalene-; creosote- and anthrecene-oils are boiled of. Anthracene oils are the heavier of the mentioned oil fractions and have boiling point above 300 ° C. Coal-tar pitches consist of many individual organic compounds, mostly polycyclic aromatic hydrocarbons with 3-6 rings (Rand, et al. [36]). The molecular mass of compounds in coal-tar pitch range from about 200 to over 2500 u, and the number of different compounds probably exceeds 10 000 (Zander and Collin [37]). Examples of some of the polyaromatic hydrocarbon compounds is shown in Figure 2-4.

Pyrene	Benzo(c)phenanthrene	Triphonytene
Phenanthrene	Benz(a)anthracene	Chrysene
Naphtalene	Anthracene	Tetracene
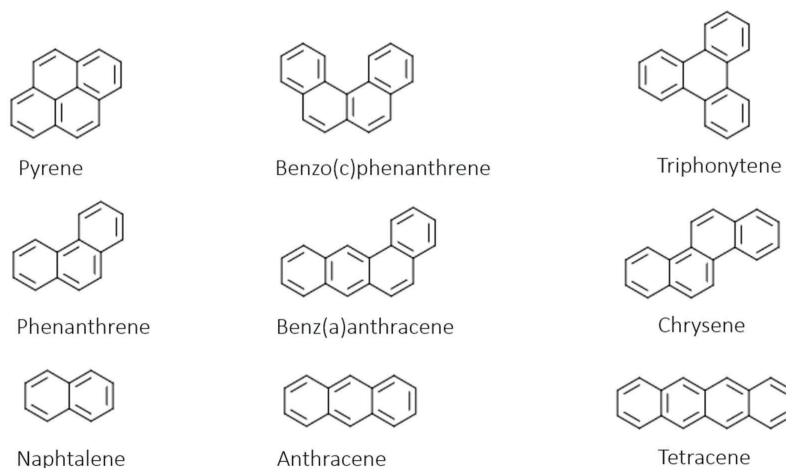
Figure 2-4: Examples of polyaromatic hydrocarbons, redrawn from Osman [38].

The high molecular mass molecules of coal-tar pitch are predominantly heterocyclic, i.e. rings containing N, O, or S. The different compounds in coal-tar pitch belong to a few similar classes where structural differences become less important with molecular size. The difference in chemical properties of each constituent will even out as the pitch consists of many compounds. The properties of pitch are thus quite homogeneous, but change steadily with increasing mean molecular weight.

Important properties of pitches for electrode pastes are softening point, coking value, pitch viscosity, distillation, and quinoline (and toluene) insolubles. Pitches have no definite melting point and change from solid to a thick viscous liquid gradually as they are non-crystalline materials. The softening point is a point to describe the change from solid to liquid and several methods exist to determine this temperature. The two most common methods are Ring and Ball

(ASTM [39]) and Mettler (ASTM [40]), and typical softening points for electrode paste coal-tar pitches range from 50 – 134° C, Shoko, et al. [41]. The Ring and Ball softening point is approximately an isoviscous temperature where the viscosity of the pitch is 1000 Pa·s.

Pitch is characterized by its solubility in solvents such as benzene, toluene and quinoline. Quinoline insolubles (QI) is often used in binder pitch specifications, and it is also called α-resin. There are two types of QI: primary and secondary, where primary QI are small particles formed in the coke oven, whereas secondary QI is formed by additional heat treatment of the coal tar and are larger than the primary QI particles (Madshus [35]). QI are quite dense particles (2.0 – 2.2 kg/dm3), and are not active binding agents and can be counted as part of the filler material (Hulse [42]). Primary QI will be good for electrode quality, whereas secondary QI is has a neutral or slightly negative impact. Benzene insolubles (BI) and toluene insolubles (TI) are soluble in quinoline, and TI is often used together with QI to characterize coal tar pitch. The difference between QI and TI is often referred to as β-resin. The TI content influence the binding ability of the pitch, i.e. increased β-resin will give better binding between pitch and coke particles (Hulse [42]).

Pitch viscosity is measured at different temperatures in the range of 50 ° C to 300° C, depending on which softening point the pitch has. The viscosity is very temperature dependent and will be important in setting the mixing temperature for the electrode paste. Coal tar pitch viscosity will be discussed later.

The coking value (/coke yield) indicates how much of the pitch will be solid carbon after baking. Some of the coal-tar pitch will be lost as volatiles, and a coking value of 55-60 % is typical for coal-tar pitches with the ISO (International Organization for Standardization) 6998 method (Hulse [42]). Distillation of the lighter fraction is also an important characteristic of coal-tar pitch used as binder for electrode paste. Distillation is usually done in the range of 270° C to 360 ° C and for electrode paste, little or no volatiles should evaporate at lower temperatures.

The glass transition temperature (T_g), which is the temperature where the coal tar pitch goes from being a glassy solid to being a viscous liquid, is used to describe how coal tar pitches softens. The viscosity of the pitch at T_g is about 10^{12} Pa·s (McNeil [43]). When compared to melting, the glass transition exhibits some fundamental differences in the thermodynamic functions and their derivatives at the temperature of change of state. At the melting temperature, there is a discontinuity in the first derivative of the molar free energy, e.g. molar volume and molar entropy, whereas in glassy solids there is no discontinuity at T_g. For the second derivatives, heat capacity and thermal expansion, there is a discontinuity at both the melting temperature and the glass transition temperature (Rand [44]).

The glass transition temperature can be measured by various techniques, such as ^{1}H NMR or differential scanning calorimetry (DSC). Lahaye, et al. [45] used DSC to find that width of the glass transition temperature is correlated to the molecular polydispersity of the coal tar pitch and that both T_g and softening point increases with heat treatment. Hatano and Torii [46] has related softening point, glass transition temperature and coke yield to toluene insolubles (TI) and light fractions in the pitch. Softening point can change by controlling the amount of both

TI and light fractions, while the glass transition temperature is controlled by adjusting the amount of light fraction, and coke yield is best changed by adjusting TI.

Pyrolysis of pitches

As temperature increase in the electrode paste during baking, the coal-tar pitch will transform to solid carbon through a process of pyrolysis. Rand, et al. [36] divide the pyrolysis of coal-tar pitches in two processes; first, the evaporation of low molecular weight species, and second the cracking and polymerization/condensation with loss of volatiles. The polymerization reaction leads to formation of oligomeric aromatic systems, and the mean molecular mass of the coal-tar pitch increases. The large aromatic sheet-like molecules (mesogens) stacks and rearrange into an anisotropic liquid crystal phase called mesophase in the temperature range of $350 - 500°$ C. With mesophase growth and coalescence, the viscosity of the coal-tar pitch increases and a green coke will be irreversibly formed as cross-linking in the mesophase increase (Madshus [35]). The structure of the resulting coke is dependent on the viscosity and the QI content, as increase in viscosity and QI particles will obstruct the growth of the mesophase. The small primary QI particles can adhere to surface of the mesophase spheres and prevent coalescence, which will give a fine mosaic texture of the coke. High intermolecular reactivity of the parent pitch will also lead to an isotropic coke. If the mesophase is allowed to grow unhindered, large anisotropic domains will be formed and physical and chemical properties of the resulting coke will be anisotropic as well.

Guillén, et al. [47] used thermogravimetric analysis (TGA) to study the pyrolysis of nine coal-tar pitches. The coke yield at 900 °C was related to the slope of the TGA curve in the temperature interval with the highest weight loss, i.e. the lower the rate of weight loss the higher the coking value. The TGA curve of the 9 pitches have the same shape and the weight loss happens in a single step starting with different temperatures for the different pitches but the maximum slope ends at 545 °C for all coal tar pitches.

Wallouch, et al. [48] used TGA and differential thermogravimetric analysis (DTG) to study the thermal decomposition of coal-tar pitches during pyrolysis. They found that the temperature range of volatilization decreases with increasing softening point of the coal tar pitch, while the temperature of initial weight loss increases with softening point, as found by Guillén, et al. [47]. With higher softening point, pitches also had higher QI and the coking value increased with softening point/QI.

Pérez, et al. [49] studied a blend of coal tar pitch and petroleum pitch and found interactions between the two pitches during pyrolysis although no interaction was found in the compositional characteristics. DTG was used to find that the temperature of initial weight loss and the temperature at maximum weight loss is modified when blending coal tar pitch and petroleum pitch. The weight loss rate in petroleum pitch has two overlapping peaks compared to one peak for coal tar pitch. When blending the two pitches it is found that the weight loss rate at low temperatures for the blends is lower than that of the pure petroleum pitch. In petroleum pitch, there is no QI particles, and addition of 5 % QI to petroleum pitch altered the DTG curve to increase the temperature of initial weight loss. Thus, the QI particles in coal tar pitch seems to drive this change in the blends.

Coal-tar pitch has for several years been listed as a "substance of very high concern" by the European Chemical Legislation REACH, due to its content of polycyclic aromatic hydrocarbons (PAHs), which are known to be carcinogenic and genotoxic. Both Eidet and Mikkelsen [50] and Becker and Leye [51] presented in 2018 work on finding PAH-free alternatives as binders for Søderberg electrodes. Eidet and Mikkelsen [50] states that finding alternative binders with similar melting and flow properties as coal-tar pitch is one of the more challenging aspects of developing alternative binders for Søderberg electrodes.

2.2. CARBON ELECTRODE PASTES

Anthracite, petroleum coke and scrap graphite are all used as solid fillers in Søderberg electrode pastes. Heat treatment of the filler raw materials used in Søderberg electrodes is important for several reasons; increased electrical- and thermal conductivity, increased strength of particles, evaporation of volatiles and reduced thermal shrinkage during heating is among the most important.

Beukes, et al. [52] used thermomechanical analysis (TMA) to examine the thermal expansion properties of raw and heat-treated anthracite. Heat threated anthracite (1400 °C) expanded 0.6 – 1.0% while raw anthracite shrinks with 6-8 % during the first thermal cycle up to 1300 °C. Thus, heat treatment of anthracite is critical for the mechanical stability of the baked electrode, and it is proposed to use TMA in the quality control of electrode paste and/or calcined anthracite.

The basic concept of carbon paste manufacture was shown in Figure 1-2, where a carbon filler and binder is mixed to form a carbon paste in an appropriate shape. For prebaked and graphitized products, a maximum packing density of the carbon filler is usually beneficial. According to Foosnæs and Naterstad [8], the size distribution of the carbon filler can have an approximate linear relationship between the cumulative mass% and the logarithm of the particle sizes from 10 μm up to 20 mm. Further, it is common in industry to achieve this relation by mixing 3-6 different particle size fractions in a specified receipt. Vidvei, et al. [53] found the best Søderberg anode properties were obtained by using the composition that gives the highest vibrated bulk density (VBD) of the coke fractions available. At this composition, the properties of the anode paste are very susceptible for changes in pitch and fines, thus it is very important to have control of the fineness of the fine particles. Properties of the baked anodes are better when moving to the finer side of the ideal VBD composition than to the coarser side.

For prebaked samples, the binder amount is determined by the amount needed to fill pores and voids and achieve maximum product density. Excess binder will expand the filler phase and decrease the baked density of the carbon product. However, for Søderberg pastes, the viscosity or flowability of the paste is determining the binder amount, as the flow of the paste is vital to achieve uniform properties of the finished product.

Several, non-standard, methods to measure the flow of Søderberg electrode paste are in use by the producers of electrode paste. Common for the methods is that electrode paste is heated and it flows under the influence of gravity or any applied force. In the *Plasticity* measurements, a cylindrical sample on a steel plate is heated to 300 °C for a specified time, after which the

increase in diameter of the sample in percent is reported as the plasticity. E.g. $Plasticity[\%] = \left(\frac{(radius\ after\ heat\ treatment\ -\ initial\ radius)}{initial\ radius}\right) \cdot 100\ \%$. The plasticity usually varies between 20-40 %. Another method was used by Bowitz, et al. [54] where paste cylinders are placed in grooves on a sloping board with a set inclination, α_{slope}. The sloping board is then inserted into an oven of either 140 or 180 °C for 60 min. The percent elongation of the cylinder is reported as the flowability. Vidvei, et al. [53] showed that anode paste with a coarser granulometry would segregate, thus the coarse particles are interlocked and a pitch and fines mixture will flow down the slope. A mixture with an excess of fines will not flow as the fines soak up the pitch and stabilized the anode paste.

The ash content of the electrode paste is determined by the filler raw material used, as anthracite usually has more ash than coke. The elemental composition of the ash is often more important than the total amount, as some ash components can be unwanted in the ferroalloy product. Whereas iron oxides in the ash will have no impact on ferroalloy production. Some typical properties of Søderberg electrode paste is shown in Table 2-3.

Table 2-3: Typical properties of Søderberg electrode paste from McDougall [7] and Wilkinson, et al. [55].

	Electrode paste
Density [kg/m³]	1600
Volatiles content [%]	12-16
Ash [%]	< 10
Plasticity [%]	15-40

2.3. SØDERBERG SELF-BAKING ELECTRODES

The electrode paste is added to the casing in the form of blocks, briquettes or cylinders, or a mix of cylinders/blocks and briquettes. The flow of electrode paste as it is heated to fill the casing is crucial to have uniform baked electrode properties. In industrial electrodes, a liquid like paste can sometimes be observed at the molten electrode paste level close to the casing in the electrode column. Measurements on segregated paste compared with normal paste shows a depletion of coarse particles in segregated paste. Measurements and a mathematical description of coarse particle depletion towards the casing has been described by Bergstrøm, et al. [56]. It is suggested that segregation is due to the stiffness of the coarse particulate mixture and its inability to deform from the pressure of the above electrode paste cylinders. Briquettes are sometimes added in segregated electrodes to add paste in between the fins to combat the effect of segregation. Adding briquettes will probably not solve the segregation problem, but can help deal with the consequences (Elkem-Carbon [14]).

The properties of a Søderberg electrode when heat treated to a temperature of 1000 °C is given in Table 2-4. Industrial Søderberg electrodes will have slightly different properties, as the baking conditions in smelting furnaces are not obtained in the laboratory. The properties of carbon will reversibly change as heat treatment temperatures increase, e.g. electrical resistivity will continue to decrease as the electrode is graphitized. Usually measurements of material

properties are performed at room temperature, however electrical resistivity is among the properties that can be measured at elevated temperatures as well.

Table 2-4: Typical Søderberg electrode properties when baked at 1000° C, from McDougall [7].

	Baked electrode
Density [kg/m³]	>1350
Electrical resistivity @25° C [µΩm]	70
Electrical resistivity @1000° C [µΩm]	40
Thermal conductivity [W/mK]	8
Bending strength [MPa]	3-5
Crushing strength [MPa]	20

The Søderberg electrode column is shown in Figure 2-5. The exact position of each type of equipment varies between different furnaces, but the figure gives a good overview of electrode equipment.

1. Electrode paste cylinder
2. Melted electrode paste
3. Baking zone
4. Baked electrode
5. Casing with fins
6. Electrode slipping equipment
7. Fan and heater
8. Suspension casing
9. Current bars
10. Cooling shield
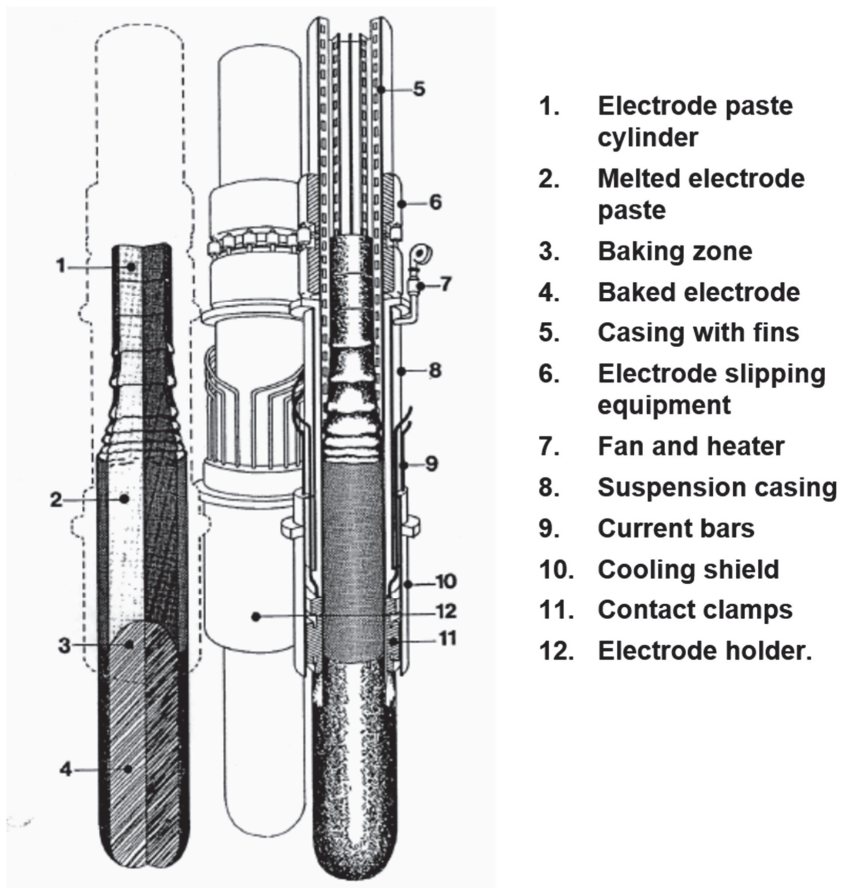11. Contact clamps
12. Electrode holder.

Figure 2-5: The Søderberg electrode column with equipment, figure used with permission from Elkem Carbon [14].

2.3.1.   CASING DESIGN

The objective of the casing and fins is to contain the electrode paste until it is baked, and provide a path for electric current into the electrode. The casing needs sufficient mechanical strength to withstand pressure from the electrode holder and slipping pressure rings. The outer casing must also be impervious to contain the liquid pitch/fines mixture at elevated temperatures. A rigid cylindrical outer casing is suitable to meet both the former and latter demand. There are two main designs, the sectional- and cylindrical casing, shown in Figure 2-6. The sectional casing comprise of a number of sections welded together, where the amount of sections equal the amount of fins. On the cylindrical casing, the fins are welded to the inner wall of the casing.

The fins of the casing conduct electrical current and heat towards the center of the electrode to improve the baking process, as steel is a much better conductor than unbaked electrode paste. The fins are often reinforced with more steel at the tip of the fins to further increase heat transfer and electric current to the center of the electrode as shown in Figure 2-6 (A-rods and D-bars).
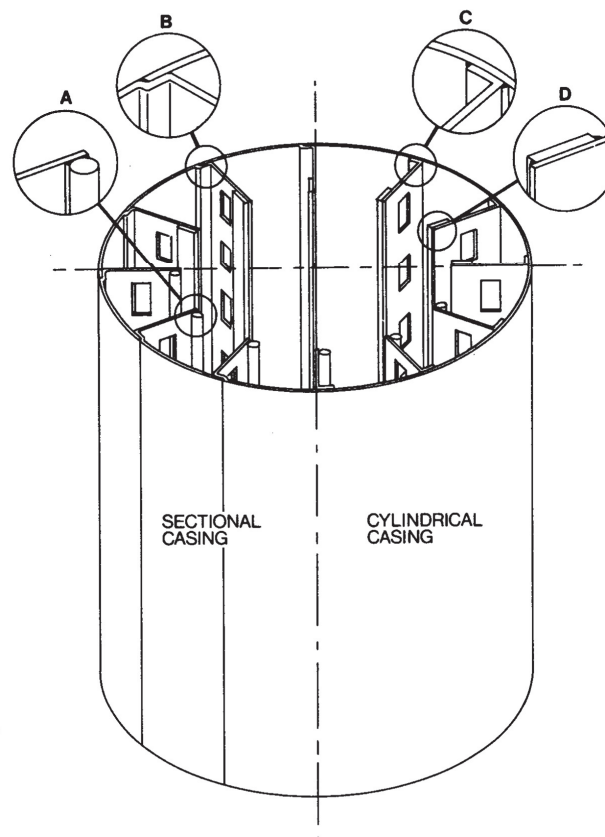

Figure 2-6: The two main types of casings; sectional casing and cylindrical casing with the different fin design (B-sectional and C-cylindrical) and reinforcements (A-rods and D-bars), used with permission from Elkem Carbon [14]

The current carrying capacity (CCC) of the casing is important when long slips are necessary and the baking zone is below the current clamps. In these situations, the steel casing must carry all of the current from the current clamps to the baked electrode below the clamps. The cross section of the casing, with fins and reinforcements minus the cut-out for anchoring, and the maximum current density in the steel is used to calculate the CCC. A value of 2.5 A/mm^2 is used in Elkem Carbon as a maximum current density for the casing steel. If the CCC is breached the casing will burn and risk leakage of molten electrode paste into the furnace, or a soft breakage. The CCC of the casing will depend on the metal production process in question, and in the slag-processes, the casing needs to carry the current as the baking zone is below the contact clamps. This is not a problem as these processes have relatively low current densities.

One important aspect of the casing and fins, which is often omitted, is the anchoring of electrode paste to the fins. The fins are produced with openings to anchor the electrode paste to the casing. To increase the area of anchoring it is favorable to increase the height of the cut-out of the fin, instead of the width, to keep as large cross-section area of the casing as possible. The tensile strength of the fins in the temperature range of 500 – 600° C needs to sufficiently high to hold the electrode. As the temperature rises under the baking zone, the steel will lose mechanical strength, while the carbon electrode strength will increase. The anchoring of the electrode paste to the casing will take place in an intermediate area, 500 – 1000° C, where both the casing and the baked electrode has sufficient strength. In furnace processes which gives a high temperature gradient between 500 – 1000° C each cut-out for anchoring needs to be sufficiently close so that there is at least one anchoring point for each fin. Without anchoring of electrode paste, it is a risk that the whole electrode can slip from the casing into the furnace.

Andersen, et al. [57] discuss the importance of the weakest point of the casing; the connection between casing sections. The quality of the joint will depend on the welding of the casing, overlap and pattern of fins and the use of reinforcement steel to increase strength of the joint. Insufficient welding may cause holes in the casing and paste may leak out in the contact clamp area. Leaked paste will increase resistance in the contact clamp and may cause arcing in the contact clamps and uneven current distribution, which can lead to soft breakages of the electrode. Poor connection of fins and lack of reinforcement steel will diminish the strength of the casing, and increase risk of soft breakages as the weak areas enters the lower part of the contact clamp.

2.3.2.   SØDERBERG ELECTRODE TEMPERATURES

The temperature distribution in Søderberg electrodes is usually found using computer models, but in the development and verification of these models, temperature measurements is used. Olsen, et al. [58] used a rig, with several thermocouples that recorded temperatures as the rig followed the electrode downwards, to find the temperature profiles found in a Søderberg electrode. Measurements were done on an open ferrosilicon furnace with electrode diameter of 1.1 m. Above the contact clamp, the temperatures are measured above 100° C, while along the casing on the upper part of the contact clamp the temperatures are below 100° C. The drop in temperature is caused by the coling water in the contact clamp. The temperature is higher in the center of the electrode than the periphery and rise to above 1000° C beneath the contact clamp. A computer model was developed to evaluate temperature profiles in different electrode conditions, e.g. higher current load and slipping rate, as it is faster to evaluate computer models compared to doing temperature measurements.

Later, Innvær, et al. [59] developed the computer model to include temperatures in-between fins, while first measuring temperature profiles. These profiles were measured on a 1.7 m diameter electrode in a ferrosilicon furnace, and the profiles are similar to those found by Olsen, et al. [58]. As the whole diameter of the electrode is measured by Innvær, et al. [59], it is evident that the side of the electrode towards the furnace center is hotter than the side towards the periphery of the furnace. In a cross section of the electrode it was also shown that temperatures are lower in-between fins compared to the positions close to the fins.

Andersen, et al. [57] discuss the use of temperature measurements to ensure that the 500 °C baking isotherm is within the contact clamps when a major change in mix of the furnace charge causes increased slipping. In this situation, a casing design change allows the slipping to be increased up to 20 % without changing the position of the baking isotherm.

2.3.3.   CARBON ELECTRODE BAKING

The position of the baking isotherm is crucial as it determines where the carbon electrode is mechanically strong enough to hold itself and it can carry the electrode current. It is widely accepted that the electrode is baked to a solid carbon body at 500 °C (McDougall [7], Innvær, et al. [60] and Innvær, et al. [61]), where the electrode has some mechanical strength and most of the volatiles has left the electrode paste. The change in density, electrical resistivity and thermal conductivity from Søderberg paste to baked electrode is shown in Table 2-5.

To specify the baking isotherm Beukes, et al. [52] used thermomechanical analysis (TMA) to investigate the dimensional change of two coal tar pitches after baking. Thermal pre-treatment to 475 °C gave a baked coal tar pitch pellet, and the TMA shows first a thermal expansion of the pellet up to the pre-treatment temperature. Above pretreatment temperature and up to 1300 °C the pellet shrinks with 12 %, and during the following thermal cycles, thermal expansion was approximately 2 %. TMA was also used by Shoko, et al. [6] to further evaluate the baking temperature of 12 coal tar pitches. Baking isotherm between 450 and 475 °C was found for all coal tar pitches, even with their softening points ranging from 65 – 134 °C.

As the electrode bake, the light components of the binder will evaporate and cause some porosity in the baked electrode. Ehrburger, et al. [62] measured porosity, i.e. pores larger than 30 µm, during baking of pitch and coke samples. There is an initial increase in porosity between 100 and 200 °C as the pitch expands above its T_g. Porosity remains the same until a marked increase at 385 °C, which match up to a weight loss of almost 20 %. The porosity may be as high as 24 % when finished heat treatment at 650 °C. Sem [63] states that the volatiles from the coal tar pitch binder may crack in the pores formed during electrode paste baking. The volatiles from the binder escapes downwards from the baking zone, passing through the pores of the baked electrode, where the volatiles are deposited as solid carbon. Sem found that an increase of carbon content of 2-3 % by cracking of volatiles increased the crushing strength in laboratory experiments. Therefor a higher pitch content can be advantageous for the Søderberg electrodes compared to the prebaked electrodes.

Table 2-5: Changes in properties during baking, data from McDougall [7].

	Søderberg paste	Baked electrode
Density	1600	>1350
Electrical resistivity [µΩm]	-	70
Thermal conductivity [W/mK]	2.5	8

The area under the baking zone have been divided into four zones depending on the carbon materials structural changes by McDougall [7]. The first zone is in the temperature region of 550-900 °C where volatiles in electrode paste will be volatilized, and the second zone from 850-1450 °C where the electrode is quite stable. In the third zone the carbon will graphitize and ash components will be reduced (1450-2500 °), and the fourth zone is the tip of the electrode where the arc may work at temperatures from 2500 °C and above.

2.3.4.   ELECTRODE BREAKAGES

The two most common types of electrode breakages are the hard- and soft breakage, where the most critical is the soft breakage. A soft breakage is a breakage in the area around the contact clamps, which results in large amounts of electrode paste being dumped into the furnace. A soft breakage is a major event and can cause serious damage to the furnace. It is usually caused by damage to electrode casing (McDougall [7]). A second cause of soft breakage can be that the electrode is slipped too much and the baking zone drops below the contact clamps. The casing will in these cases not be able to withstand a full electrode current and the casing will burn and soft paste can leak out of the casing (Innvær, et al. [60]). A third reason for soft breakages is that the baking zone has come below the contact clamps because furnace load has been reduced below normal. As the heat needed for electrode baking is proportional to the current squared, reduction in power will lower the baking zone if slipping is maintained.

Good control of electrode slipping and careful handling of electrode casings ensure that soft breakages seldom occurs in modern electrode operations (McDougall [7]). Even so high slipping can cause the baking zone isotherm to fall below the contact clamps and soft breakages

can occur as reported by Ray, et al. [64]. Ray concludes that soft breakages can be eliminated with good electrode management, which is a set of procedures concerning electrode and electrode paste that does not affect furnace operations.

Hard breakages vary in severity, from small pieces of the tip falling off to several meters of electrode breaking off. Hard electrode breakages may be caused by a number of factors from McDougall [7]:

- Thermal stresses may lead to cracking and spalling of the electrode
- Non-sufficient baking of the electrode may cause the mechanical strength of the electrode to be inadequate.
- Overbaking, where the paste dries out too much during baking making the baked electrode brittle.
- Unbalanced lateral mechanical forces on the electrode due to asymmetric feed piles.
- Paste segregation before baking may lead to anthracite particles with little binder between them, which will make a very brittle electrode.

Innvær, et al. [60] categorizes less critical unwanted electrode consumption into, small breakages on the tip of the electrode, higher consumption in fin areas of the electrode (splitting), or high surface consumption. All these can give problems in maintaining ideal electrode position.

Hard electrode breakages are commonly caused by furnace shutdowns and/or start-ups. Larsen, et al. [65] have used mathematical modeling to find furnace shut-down procedures that can minimize thermal stresses in the electrodes during shut-down. Figure 2-7 show stresses caused by thermal gradients for an electrode covered with charge material and an uncovered electrode respectively. Procedures for different furnace shutdown scenarios are proposed based on the mathematical modeling.
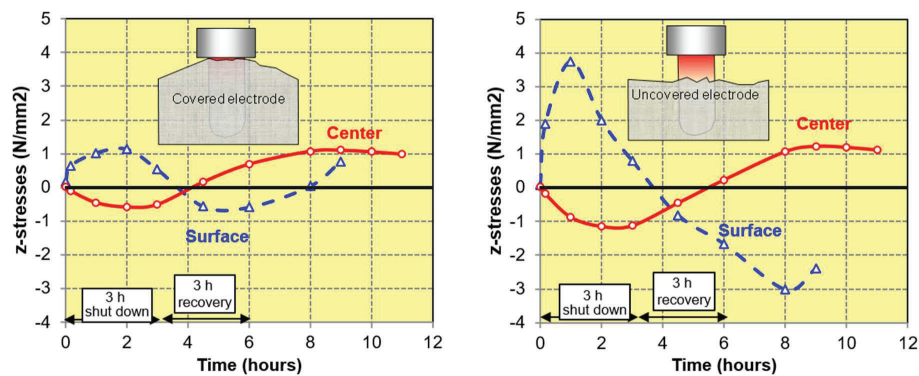
Figure 2-7: Thermal stresses in center and at the surface for a covered and an uncovered electrode during furnace shutdown, received directly from the author to use in this work (Larsen, et al. [2]).

Nelson and Prins [3] have found that hard breakages can be caused by segregation of paste as they investigated industrial breakages. Several electrodes are shown, where the paste clearly has segregated into areas rich in coarse material close to the center of the electrode and depleted

of coarse material close to the casing. By improving how electrode paste is added, regularly and with correct levels cylinder heights, electrode performance will be better. This means that conditions under which the electrode paste flows when it fill the casing is important for electrode quality.

Hard breakages caused by failure to bake the electrode sufficiently can also be avoided by implementing electrode management procedures such as regular addition of new paste and slipping electrode in small increments. Equipment such as heating fans to preheat the electrode casing and paste can warrant good baking conditions [7]. Furnace automation systems for electrode slipping and electrode baking after long slips has been adopted to avoid breakages in such situations (Strydom and McDougall [66]).

2.3.5.   ELECTRODE SLIPPING [14]

As the electrode is consumed, it is slipped in increments to sustain the desired electrode tip position. The goal is to slip the electrode as smooth and continuous as possible, with e.g. 1 slip an hour. The maximum slipping rate is determined by how fast the electrode paste bakes, which is driven by heat from the resistive heating of the current entering the electrode. If the resistance of the electrode is constant, the heat generated will be proportional to the current squared (I^2). It is suggested by Elkem Carbon [14] to base slipping on a slip index (α_{slipp}) with dimensions;

$$\alpha_{alipp} = \left[{mm}/{h \cdot A^2} \right]$$

The slip index will depend on the size of the electrode. In Figure 2-8 the slip index and slipping rate for a 1.55 m diameter electrode is calculated. The normal slipping rate should be at the "safe" slip index or below, and it is desirable to keep the slip index as constant as possible. If the slip index is kept near maximum levels the baking zone could be close to the contact clamp tip, and measurements may be needed to ensure that the baking zone is within the contact clamp.
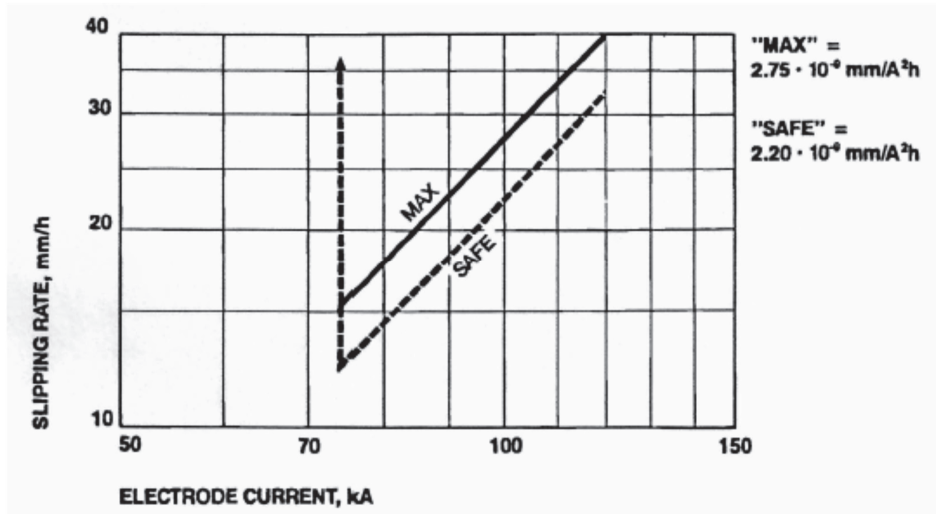
Figure 2-8: Slipping rate for a 1.55 m electrode where the current carrying capacity of the casing is 74 kA, and limits for "max" and "safe" slipping. Used with permission from Elkem Carbon [14].

Extra electrode slipping is needed if an electrode become too short and is not capable of carrying the desired current. Two methods can be applied to elongate the electrode, forced slipping and long slipping. Forced slipping is usually preferred, where the electrode current is lowered to below the current carrying capacity of the casing and slipping rate is increased up to 100mm/h. When the electrode achieves desired length, the slipping is stopped and the current is kept unchanged for one hour. The current can then be increased by 5 kA/h for forced slipping lengths lower than 1 m. For longer forced slipping lengths, the recommended rate of current recovery is 2.5 kA the first 10-20 kA.

For long slipping, the desired electrode extension is done in one step with no current. The electrode current should be lowered to 40 % of maximum when the furnace is energized. To make time for baking of the electrode paste, the current is increased at a rate that depend on electrode size and long slipping length, as shown in Figure 2-9 for a 1.55 m diameter electrode. A too rapid increase in current may give a porous electrode or in the worst case a soft electrode breakage. The soft electrode breakage will be caused by exceeding the current carrying capacity of the casing while the electrode paste has not finished baking.
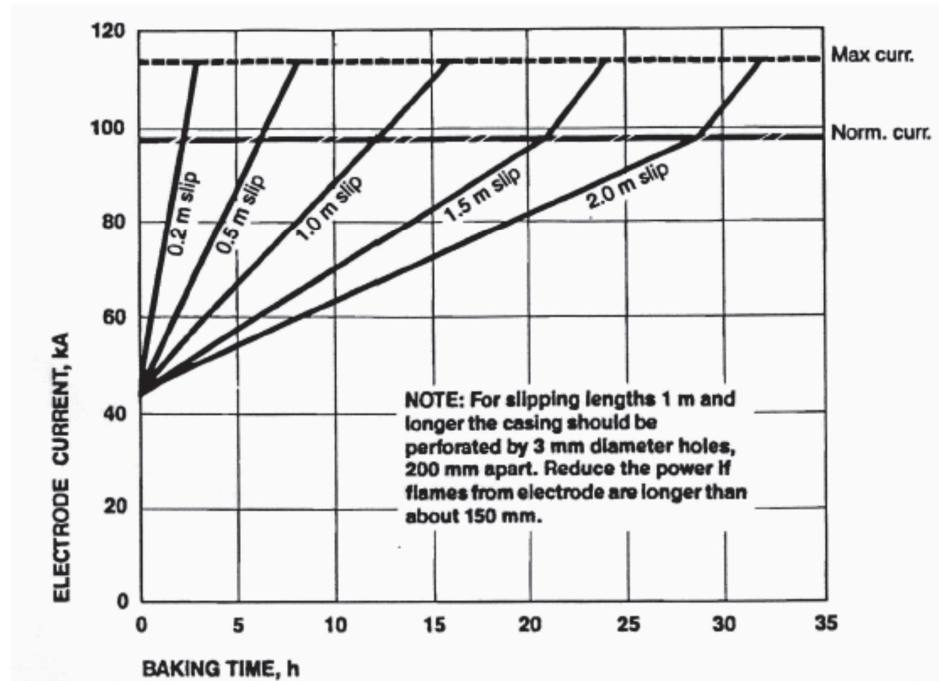
Figure 2-9: Current recovery after a long slip of a 1.55 m diameter electrode, used with permission from Elkem Carbon [14].

2.3.6.   FURNACE SHUT-DOWNS [14]

During furnace shutdowns, the electrode is cooled as the main source of heat is removed. During cooling, the baked electrode has increased risk of hard breakages due to the thermal stress caused by thermal gradients from uneven cooling (/heating) between the middle of the electrode and the surface. Elkem Carbon [14] has prepared a set of procedures for furnace shut-downs dependent on the length of the shutdown. For all planned shut-downs the electrodes should be covered with furnace charge or isolation as soon as the furnace is stopped to reduce heat loss. The electrodes can also be set in a low position, slipped 100 – 200 mm after stop and reduce water-cooling. The water-cooling can be reduced by either increasing the cooling water temperature, or reducing the flow.

For furnace shutdowns shorter than 8h, the objective of the procedure is to minimize the heat loss by stopping the furnace at full load (transformers are of course taped to first level before de-energizing) and a rapid ramping up of electrode current to normal levels after energizing. Before longer shutdowns the electrode current should be reduced in the days prior to the shutdown to lower the temperature of the electrode. Start-up procedures for longer shutdowns include ramping up the electrode current to avoid too high thermal stress in the electrode. For a shutdown above 24 h the electrode current could be adjusted down to 80 % of normal current

at least 2 days before shutdown and start at 50 % of normal current with a ramp-up depending on the electrode diameter, as shown in Figure 2-10.
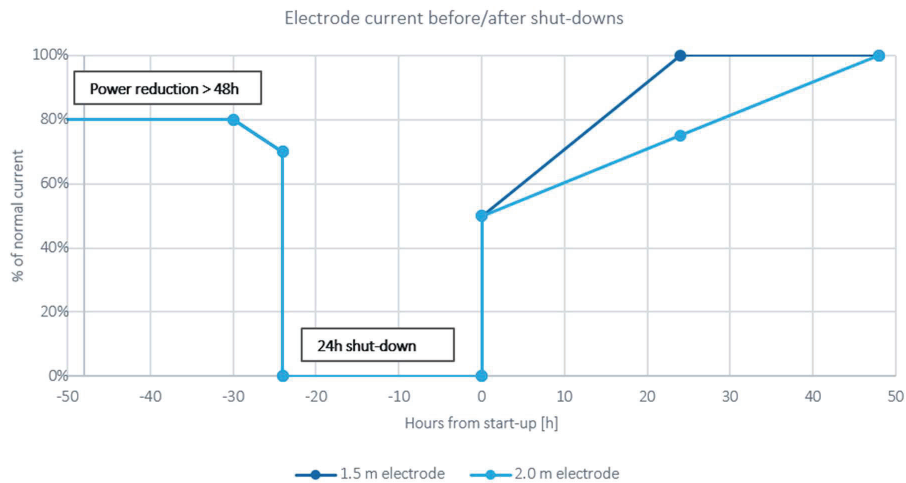

Figure 2-10: Electrode current before and after a furnace shutdown exceeding 24 h redrawn from Elkem electrode manual[14]

2.4. SØDERBERG ELECTRODE MODELLING

Computer modelling of electrodes has been used extensively to prevent and understand electrode breakages, e.g. Larsen et al. [2], Ord et al. [4] and Innvær et al. [59, 61]. In Elkem, mathematical modeling has been in use since the 1970ies, and many papers have been published during the development of these models [2, 57-59, 61, 67]. The model was first used to assess the influence of varying current and slipping on the temperature distribution in the contact clamps. The high current case increases temperature within the contact clamp, while high slipping reduces temperatures in the contact clamp, especially at the center of the electrode.

Later Innvær, et al. [61] used the electrode model to assess thermal stresses during shut-downs to reduce the risk of hard breakages of the electrode during/after shutdowns. The thermal stresses were found to be largest 8-10 hours after start up after a 6h shutdown. Lower electrode current lowered the maximum thermal stress as well. As computing power has grown the Elkem model has evolved and several later papers discuss the application of the model on thermal stresses, e.g. Andersen, et al. [57] and Larsen, et al. [2]. Andersen, et al. [57] finds that a slower recovery of current after a 12h shutdown reduces thermal stresses in the electrode. It is stated that to optimize shutdown/start-up procedures electrode equipment and size and furnace operating practices needs to be considered.

Larsen, et al. [2] states that that a model needs to apply AC current, compared to DC, to study temperature distribution and corresponding thermal stresses in large Søderberg electrodes. The temperature and current density are given in Figure 2-11 for the two cases with AC and DC current. As the current density in DC is higher in the center of the electrode compared to AC it

is also hotter in the center. As the center of the electrode is hotter in a DC model the potential cooling and the resulting thermal stress is higher. The calculated thermal stress from the Elkem electrode model is given in Figure 2-12, where there is a difference between the two cases, and the DC current case gives higher thermal stresses than the AC current.
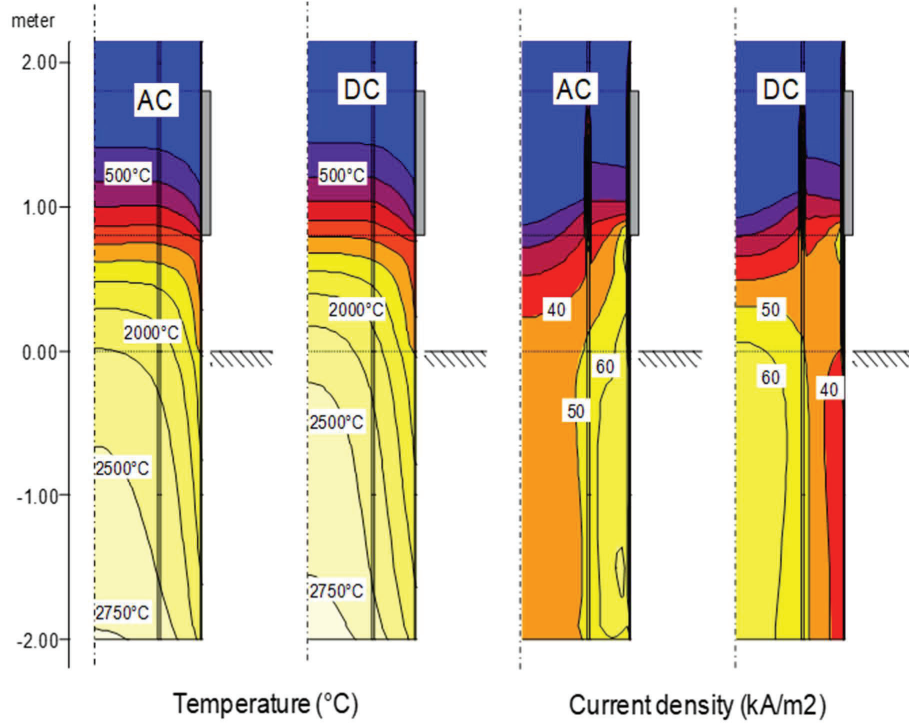

Figure 2-11: The isoplots for temperature and current density for AC and DC from the Elkem electrode model, received directly from the author to use in this work (Larsen, et al. [2]).
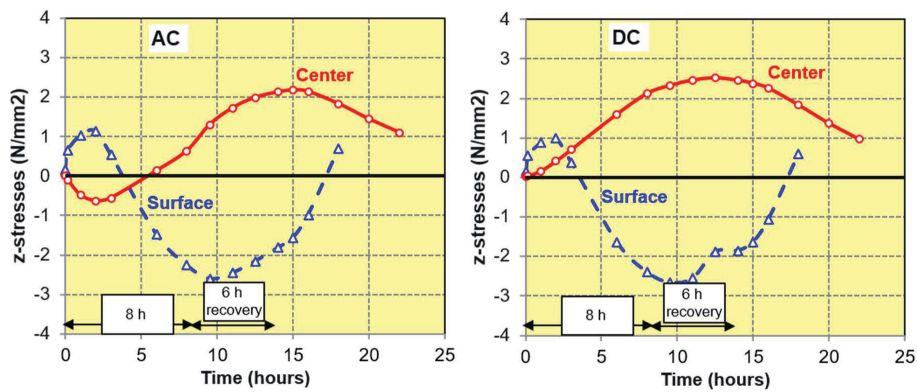

Figure 2-12: The calculated thermal stress from the Elkem electrode model for AC (left) and DC (right), received directly from the author to use in this work (Larsen, et al. [2]).

Ord et al. [4] have studied the electrode equipment influence on electrode temperature by using mathematical simulations in non-ferrous furnaces, and coupled the modelling with temperature measurements with good correlation. As modelling is much faster than a temperature measurement campaign, modelling can give fast results to problems experienced with an electrode. In this case, cold cooling water in the contact clamps had caused electrode breakages and this was realized with the help of the modelling done.

Several other authors have presented the use of computer models for specific cases, e.g. Meyjes et al. [68] have used modeling as a tool for casing and current clamp design. They choose a more complex geometrical model, but modelling with DC current. They found that increasing heating by mantle air or contact clamp cooling water has little effect on the baking temperature. The main effect on the baking temperature is the electrode current.

McDougall et al. [69] have used a 3-D model to asses different casing materials and their influence of the baking zone. The 450 °C baking isotherm was evaluated for several casing materials with a DC current being modelled. It was found that the casing material have an effect on the baking isotherm, and Chromanite steel could be used instead of the existing Grade 304 as the 450 °C baking isotherm is almost identical. For other casing material options, the baking isotherm is lowered in the contact clamp.

2.5. VISCOSITY

Isaac Newton first hypothesized the viscous properties of liquids in "Principia" published in 1687. He stated that for simple shearing flow, the resistance against flow in a liquid is proportional to the velocity which the parts of liquid are separated from one another, when the other parts of the measurement are kept constant.

Figure 2-13 shows two parallel plates, both with area A and separated by a liquid with thickness d, where the top plate moves with velocity v in x direction. The shear stress (σ) is defined as the shear force component (F) tangential to the surface per unit surface area (A). The shear stress is proportional to the velocity gradient (or shear rate) v/d and the proportionality constant η is called the coefficient of viscosity (Barnes, et al. [70]).

$$\sigma = \frac{F}{A} = \eta\frac{v}{d} \qquad (2\text{-}3)$$

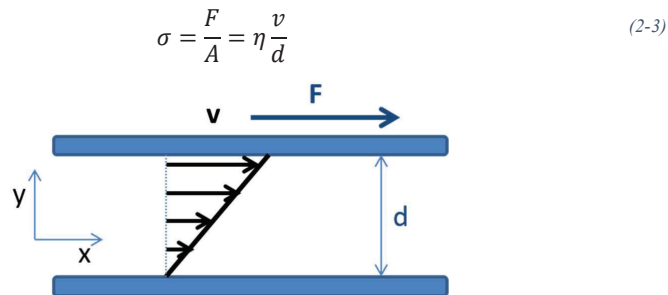Figure 2-13: Liquid between two parallel planes where F is the force working in the x direction on the upper plate, v is the speed of the plate and d the distance between the two plates.

The shear rate v/d is usually written as $\dot{\gamma}$, and equation 1 becomes $\sigma = \eta\dot{\gamma}$. This equation describes well the resistance to flow for gasses and liquids with molecular weight below about

5000 *g/mol*, and such fluids are called *Newtonian fluids*. More complex fluids like slurries, polymeric liquids and pastes are not described by this equation and are called non-Newtonian fluids (Bird, et al. [71]).

Barnes et al.[70] give the following characteristics for Newtonian behavior in experiments at constant temperature and pressure:

- The only stress generated in simple shear flow is the shear stress σ, the two normal stress differences being zero.
- The shear viscosity does not vary with shear rate.
- The viscosity is constant with respect to time of shearing and the stress in the liquid falls to zero immediately when the shearing is stopped. In any subsequent shearing, however long the period of resting between measurements, the viscosity is as previously measured.
- The viscosities measured in different types of deformation are always in simple proportion to one another, e.g. the viscosity measured in uniaxial extensional flow is always three times the value measured in simple shear flow.

For Newtonian fluids, the viscosity decreases with increasing temperature according to an Arrhenius relationship:

$$\eta = Ae^{-E_a/RT} \qquad (2\text{-}4)$$

Where T is absolute temperature and A is a constant of the liquid, E_a the activation energy and R the gas constant. The strong temperature dependency can be illustrated with water at room temperature with a temperature sensitivity of 3 % pr. K. Newtonian fluids show in general stronger temperature dependency as viscosity of the fluid increase (Barnes, et al. [70]).

The viscosity of most Newtonian fluids increases exponentially with isotropic pressure. However, changes of one bar around atmospheric pressure are usually small. The pressure dependency is assumed to be negligible for carbon paste processing (Hulse [42]) and is not discussed any further in this work.

2.5.1.   NON-NEWTONIAN FLUIDS

Non-Newtonian liquids will show deviations from the points listed by Barnes, et al. [70] in the previous section. The different types of time independent non-Newtonian fluid behavior are shown in Figure 2-14. The most common non-Newtonian behavior is shear thinning (or pseudoplastic), where the apparent viscosity decrease with increasing shear-rate. The opposite, where apparent viscosity increase with increasing shear-rate, is called shear-thickening (or dilatant) fluids.
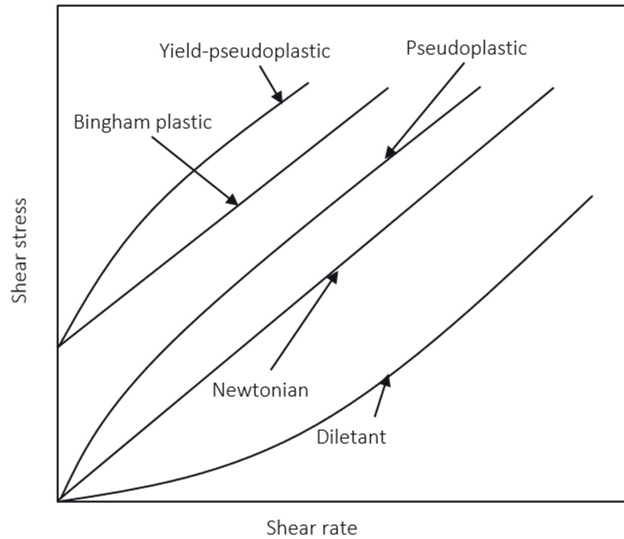
Figure 2-14: Newtonian fluid behavior compared to time independent non-Newtonian fluids (redrawn from Chhabra and Richardson [72]).

The power-law model express the viscosity of non-Newtoninan fluids, the equation is

$$\eta = m\dot{\gamma}^{n-1}$$

(2-5)

Where the two empirical found parameters m and n are known as the fluid consistency coefficient and flow behavior index respectively. For n=1 the fluid shows Newtonian behavior, for n<1 shear-thinning behavior and for n>1 shear-thickening behavior.

2.5.2.   SHEAR THINNING FLUIDS

Many shear-thinning materials have constant viscosity in the limits of very low and very high shear-rates. The resulting apparent viscosity values are called zero shear viscosity, μ_0, and infinite shear viscosity, μ_∞, respectively. These constants are used in mathematical modeling of viscosities, one such model is the Cross viscosity equation:

$$\frac{\eta - \eta_\infty}{\eta_0 - \eta_\infty} = \frac{1}{1 + k\dot{\gamma}^n}$$

(2-6)

where n(<1) and k are fitting parameters. Cross [73] originally suggested n = 2/3, but in more recent works the use of n as an adjustable parameter has improved the fit of the equation to more viscosity data (Barnes, et al. [70], Chhabra and Richardson [72]). Based on molecular network considerations by Carreau [74] the *Carreau equations* has also been used by Bird, et al. [71] and Chhabra and Richardson [72] to model shear-thinning viscosity.

$$\frac{\eta - \eta_\infty}{\eta_0 - \eta_\infty} = [1 + (k\dot{\gamma})^2]^{\frac{n-1}{2}}$$

(2-7)

The Ellis fluid model is used when deviation from the power-law model are significant only at low shear rates. The three-constant model for the apparent viscosity is as follows:

$$\eta = \frac{\eta_0}{1 + \left(\frac{\sigma}{\sigma_{1/2}}\right)^{\alpha-1}},$$
<div align="right">(2-8)</div>

where η_0 is the zero shear viscosity and the remaining two constants α (>0) and $\sigma_{1/2}$ are adjustable parameters.

2.5.3.   SHEAR THICKENING FLUIDS

When the apparent viscosity increases with increasing shear rate the fluid is called a shear thickening. Shear thickening was first observed in solutions with a high concentration of solids and an explanation is given by Chhabra and Richardson [72].

At rest, the voidage is minimum, the liquid lubricates the motion of each particle past others, and the resulting stresses are consequently small. At high shear rates, on the other hand, the material expands or dilates slightly so that there is no longer sufficient liquid to fill the increased void space and prevent direct solid-solid contacts which results in increased friction and higher shear stresses. This mechanism causes the apparent viscosity to rise rapidly with increasing rate of shear.

This explanation is only applicable to suspensions, but the term dilatant has been used for all fluids where the apparent viscosity increases with increasing rate of shear. The shear thickening region usually extends over about a decade of shear rates and the power law with n greater than unity can usually be fitted to the viscosity data. Suspensions with moderate amounts of solids and shear thickening behavior at high rates of shear usually show shear thinning behavior at low shear rates [70].

2.5.4.   VISCOSITY OF SUSPENSIONS

Barnes, et al. [75] divided the suspension viscosity into four regions depending on the shear rate, shown in Figure 2-15. At low shear rates the suspension may act as Newtonian liquids (A), but as shear rate increase the viscosity will enter a power-law region (B) where viscosity decrease with higher shear rates. With still increasing shear rate the viscosity enters a plateau region (C) before it acts shear thickening (D) at the highest shear rates.
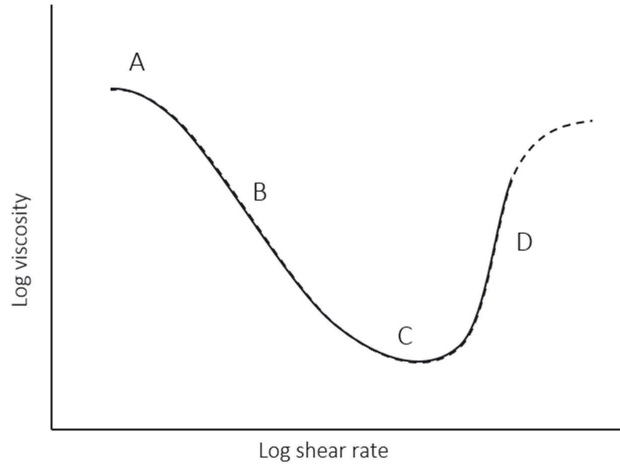
Figure 2-15: The flow curve of a suspension with the 4 (A-D) distinct viscosity regions, A – Newtonian plateau region, B – Power law region, C – Plateau region II and D – shear thickening region (redrawn from Barnes, et al. [75]).

For suspensions, it is useful to replace the two-phase system with a hypothetical one-phase system. Einstein considered a dilute suspension of rigid spheres, where the spheres do not influence the fluid flow around the neighboring spheres. The solution is sometimes called the *Einstein equation* (Einstein [76] and Einstein [77]).

$$\frac{\eta}{\eta_s} = 1 + \frac{5}{2}\Phi \qquad \text{(2-9)}$$

Where η_s is the viscosity of the suspending medium and Φ is the volume fraction of the spheres. For concentrated suspensions of spheres one of the simpler semi-empirical expressions is the Mooney equation (Mooney [78]):

$$\frac{\eta}{\eta_s} = \exp\left(\frac{{}^{5}/{}_{2}\,\Phi}{1 - {}^{\Phi}/{}_{\Phi_0}}\right) \qquad \text{(2-10)}$$

Φ_0 is an empirical constant between 0.74 and 0.52, which corresponds to Φ for closest packing and cubic packing, respectively.

Krieger and Dougherty [79] developed an expressions for concentrated suspensions where particles of any shape can be accounted for. The *Krieger-Dougherty* equation is

$$\eta = \eta_s \left(1 - \frac{\Phi}{\Phi_m}\right)^{-[\eta]\Phi_m} \qquad \text{(2-11)}$$

where $[\eta]$ is the intrinsic viscosity, which is defined as $[\eta] = \lim_{\Phi \to 0} \frac{\eta - \eta_0}{\eta_0 \Phi}$ (Scheraga [80]) and Φ_m is the maximum packing fraction. Deviations from spherical particles have strong effect on the intrinsic viscosity and maximum packing fraction. Barnes [70] provides simple empiricism for effect of discs and rods on the intrinsic viscosity for large axial ratios:

$$\text{Discs: } [\eta] = {}^{3P}/_{10}$$

$$\text{Rods: } [\eta] = {}^{7P^{5/3}}/_{100}$$

where P is the axial ratio. Allowing $[\eta]$ and Φ_m to change for different shear rates, both very high and very low shear rate fits the Krieger-Dougherty equation for monodisperse lattice (Krieger [81]). It was also found that $[\eta]$ and Φ_m are stress-dependent, but independent of particle size. Coussot [82] shows a version of the Krieger-Dougherty equation where the intrinsic viscosity is substituted with the value 5/2, which is the intrinsic viscosity of rigid spheres at maximum dilution. Another empirical equation mentioned by Coussot is:

$$\eta = \eta_s \left(1 + \frac{3}{4} \frac{\Phi}{\Phi_m - \Phi} \right)^2 \qquad (2\text{-}12)$$

Coussot states that approaches like these are problematic as the volume fraction of solids increase. E.g. as the volume fraction of solids increase the separating distance between particles decrease and interactions are not taken into account. The packing fraction is also not a single intrinsic parameter, as the packing of a materiel depends on the way it is obtained, thus it is not evident that it describes the packing in the solution.

Empirical use of the Krieger-Dougherty equation has found that Φ_m is strongly dependent on the particle size distribution, i.e. Φ_m increases with increasing polydispersity. Farris [83] found that the minimum viscosity is found when

$$\Phi_1 = \Phi_2 = \Phi_3 = \Phi_4 \ldots = \Phi_N$$
$$\Phi_m = \frac{V_m}{(V_0 + V_1 + V_2 + \cdots + V_{m-1} + V_m)} \qquad (2\text{-}13)$$

where V_m is the volume of particle-size fraction m. Mixing particle sizes can reduce the viscosity of a suspension while keeping the same amount of solids. Farris [83] found in a trimodal system the tertiary minimum viscosity to be about 85 % of the binary minimums. Total amount of solids where kept at 65 vol%.

2.5.5.   PASTES AND GRANULAR MATERIALS

Pastes are by Coussot [82] described as a soft jammed system where soft interactions predominate. When the fraction of colloidal particles (suspended particles of sizes ~1 nm – 1 µm) is low, the material can be considered Newtonian. While at higher concentrations, there exists a continuous network of interactions between particles, and the material evolves continuously from a Newtonian liquid to a soft jammed system.

Granular pastes are highly concentrated suspensions of noncolloidal particles in a liquid or paste (Coussot [82]). The fluid most be continuous with a high fraction of grains, possibly in contact, dispersed in it. Two distinct flow regimes can be found in such pastes. For slow flow-rates, there will be a continuous network of direct contact between particles and thus high frictional interaction. As flow increases, the grain interactions can be lubricated by the interstitial fluid, and the flow is governed by the interstitial fluid. For more on rheology of granular pastes see Coussot [82].

2.6. VISCOSITY MEASUREMENTS

Viscometers are by Barnes, et al. [70] divided into three broad groups; rotational viscometer, capillary viscometers and "flow around obstructions" (e.g. falling sphere). Viscometers are usually calibrated using a Newtonian oil of known viscosity, which is measured by a capillary viscometer calibrated with water at 20.00 °C. The viscosity of water at 20.00 °C is known with an uncertainty of ± 0.25 %, and thus the precision of a viscometer is worse than 0.25 %. For mechanical instruments, the uncertainty is more realistically in the area of ten times the uncertainty of water. Most viscometers are made to measure Newtonian liquids, and great care must be taken when measuring non-Newtonian liquids or suspensions. Quite complicated theoretical mathematical derivations are needed to generate consistent viscosity data for non-Newtonian liquids.

2.6.1. ROTATIONAL VISCOMETRY

There is two ways of inducing flow in a rotational viscometer, either by driving one member and measuring the resulting force couple or by applying the couple and measuring the rotation rate. The former of the two was introduced by Couette in 1888 and the latter by Searle in 1912 (Barnes, et al. [70]). The flow of a liquid between two rotating concentric cylinders is often called "Couette flow", and if the gap between the cylinders is small (i.e. $\frac{r_1}{r_2} > 0.97$) the shear rate is given by

$$\dot{\gamma} = \frac{r_2 \Omega_1}{r_2 - r_1}$$

(2-14)

Where r_2 and r_1 are the radius of the outer and inner cylinders, and Ω_1 is the angular velocity. If the couple on the cylinder is C, the viscosity of the liquid is given by

$$\eta = \frac{C(r_2 - r_1)}{2\pi r_2^3 L \Omega_1}$$

(2-15)

Where L is the effective immersed length of the liquid under the shearing force. The effective immersed length would be the real immersed height h_L if there were no end effects. End effects are likely to occur due to different shearing conditions in the liquid covering the ends of the cylinder. Usually this is solved by putting a cone at the end of the inner cylinder, where the tip of the cone touches the bottom cylindrical container. By having, the cone angle equal to $\tan^{-1}(r_2 - r_1/r_2)$ the shear rate of the liquid under the plate will be the same as between the concentric cylinders (Newtonian fluid, small gap). A schematic of the concentric cylinder viscometer is shown in Figure 2-16 where the angle of the conical end is given as α for the cone and plate viscometer shown to the right.
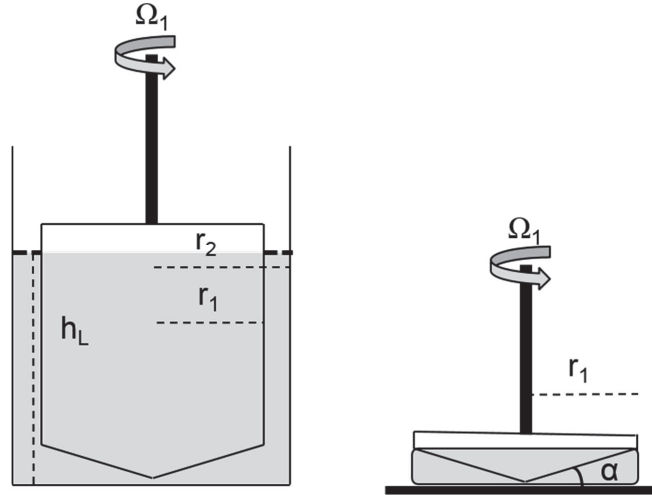
Figure 2-16: Schematic of the concentric cylinder with conical end viscometer and cone and plate viscometer.

The cone and plate geometry shown in Figure 2-16 is a common geometry used in viscometers as for low cone angels ($\alpha < 4$ °) the shear rate in the liquid is close to uniform. The tip of the cone should be placed at plate surface, but to avoid wearing of the cone tip and indentation of the plate, the tip is often truncated. The cone should then be placed such that the virtual tip is on the plate surface. Errors in the axial separation will give large errors in the shear rate Barnes, et al. [70]. The shear rate of the cone and plate viscometer is given by

$$\dot{\gamma} = \frac{\Omega_1}{\alpha} \qquad \text{(2-16)}$$

And the viscosity can be calculated by

$$\eta = \frac{3C\alpha}{2\pi r_1^3 \Omega_1} \qquad \text{(2-17)}$$

The small gap of the cone and plate viscometer is one of the largest drawbacks with the method, as it is not suitable to measure suspensions or pastes where particles will influence measurements. At low viscosity, the high rotational speeds required to produce torques big enough to measure accurately may create "secondary" flows that will absorb energy. A Newtonian liquid may then be erroneously associated with shear thickening behavior[70]. Advantages with the cone and plate method is its relative simplicity and the uniform shear rate in the liquid.

2.6.2.   CAPILLARY MEASUREMENTS

In capillary viscometers, a pressure drives the liquid through a pipe and the viscosity can be calculated when the length and diameter of the pipe is known as well as the volumetric flow rate. Measurements can be done by either constant pressure drop or constant volumetric flow rate. For a Newtonian liquid the pressure gradient (P) along the length of the pipe (l) can be expressed as

$$\frac{dP}{dl} = \frac{8Q\eta}{\pi r^4} \qquad \text{(2-18)}$$

Where Q is the volumetric flow and r is the radii of the pipe. For Newtonian liquids, the shear stress will be maximum at the wall $\left(\sigma = \frac{r}{2}\frac{dP}{dl}\right)$ and will vary linearly to zero at the center. The shear rate will also be maximum at the wall $\left(\dot{\gamma} = \frac{4Q}{\pi r^3}\right)$ and decrease to zero in the center of the capillary. Since the shear rate is non-uniform in the pipe capillary measurements can only be used to measure steady shear functions. However, capillary measurements are popular as they are similar to flow in pipes common in engineering processes and are relative simple, cheap and accurate with long capillaries (Chhabra and Richardson [72]).

2.6.3. FALLING SPHERE

The falling sphere viscometers is based on Stokes' law, where the viscous resistance on a sphere falling with uniform velocity, v, is (Oka [84]):

$$F_{stokes} = 6\pi r\eta v \qquad \text{(2-19)}$$

The forces on the sphere as it falls is given by gravity and the density of the sphere and fluid, and the viscosity can be expressed as Stokes' law:

$$\eta = \frac{2(\rho_{sphere} - \rho_{liquid})gr^2}{9v} \qquad \text{(2-20)}$$

The derivation is based on low velocity of the sphere, that the fluid is of infinite extent, no slip between sphere and fluid, and that the sphere is rigid. For high viscosity and low velocity, when the Reynolds' number $\left(Re = \frac{2r\rho v}{\eta}\right)$ is negligible compared to unity, the first assumption holds. The assumption of liquid extent being infinity is not fulfilled and corrections for wall effects can be used. The two last assumptions usually holds for falling sphere viscosity measurements.

2.6.4. SQUEEZING FLOW

A comprehensive review of squeeze flow has been given by Engmann, et al. [85], and the following is based on that review. Squeeze flow can be defined as when a material is deformed between two parallel plates that are moving towards each other, and will in this case be limited to the axisymmetric case. Squeeze flow deformation has applications within many disciplines, e.g. engineering (compression moulding of metals and polymers, lubrication), biology (diarthrodial joints), food manufacturing (chewing, texture between fingers). In rheology squeeze flows has applications to a wide range of materials, such as purely viscous, yield stress materials, viscoelastic, and elastic solids. In rheometry, two methods of squeeze flow rheometers exist; constant area between sample and plate, and constant volume of sample, see Figure 2-17 and Figure 2-18. The advantage with the constant area (Figure 2-17) case is that the contact area and the position of the sample is well known. Disadvantages are the unknown boundary conditions at the edges of the plates, which becomes more severe at low compression speeds, high sample viscosity, and if temperature gradients between test atmosphere and sample are present. With the constant volume geometry (Figure 2-18), the stresses on the edge of the

sample are better defined, but the contact area between sample and plate needs to be accounted for and the wetting behavior of plate/sample/air may affect data. The constant volume case is also usually closer to industrial compression moulding processes.
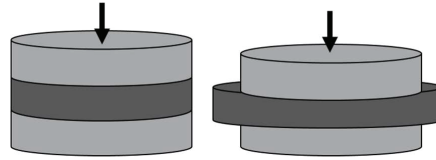

Figure 2-17: Axisymmetric squeeze flow with constant area between sample and plate, adopted from Engmann, et al. [85].
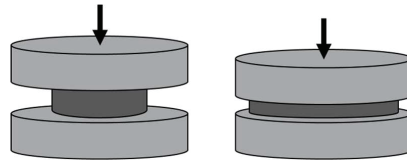

Figure 2-18: Axisymmetric squeeze flow with constant sample volume, adopted from Engmann, et al. [85].

The conditions at the interface between sample and plate will determine how the sample will flow when squeezed as in Figure 2-17 and Figure 2-18. Two ideal cases are treated in Engmann, et al. [85], the perfect slip and the no-slip case. In experiments, it is not always evident if there is no slip, perfect slip or a partial slip. For Newtonian and power-law fluids, the average normal stress versus radius/height will be constant for the perfect slip condition at constant compression rate. The non-slip scenario can be imposed by increasing the roughness of the plate or a more impractical approach is to glue the sample to the plate. Alternatively, the flow can be lubricated by either non-wetting surfaces or a lubricating fluid/solid.

The advantages and disadvantages of squeeze flow rheometry are summarized in Table 2-6.

Table 2-6: Advantages and disadvantages of squeeze flow rheometry, from Engmann, et al. [85].

Advantages	Disadvantages
Wide range of shear rates	Non standardized technique
Initial structure kept while loading	Inertia must be taken into account
Similarity to process flows	Inhomogeneous flow field
Internal deformation of sample	Difficult to assume boundary conditions (no-slip, perfect slip)
Easy set-up	

2.6.5.   PARALLEL PLATE VISCOMETER

Tørklep [86] considered several viscometers for measurements on carbon electrode paste and decided that a parallel plate viscometer is advantageous for these reasons:

- Load characteristics similar to industrial practice can be used
- The measurement range is large, without changing configurations
- Large samples and large measurements gaps can be used, as filler particles can be 15 mm in diameter.

Tørklep realize that for carbon electrode pastes a complete rheological description is not feasible, and measurements comparable to the loads and shear rates attained during the industrial process seems as one of the most descriptive methods to study the rheological properties of electrode paste. The gap size for highly reproducible results should be 50-100 times bigger than the largest particles in the suspension to be measured, which is a problem for electrode paste where coke/anthracite particles can be up to 15 mm. However, Tørklep states that a measurement gap of at least three times the largest particle size is acceptable, with an expected scatter in the results. The theoretical background for calculating apparent viscosity with a parallel plate apparatus will be presented in the following sections.

In Figure 2-19 the parallel plate viscometer is shown, with a moving upper plate at height z=h(t), the lower plate at z=0 and the force F acting on the upper plate. The sample is placed in between the two plates and is squeezed radially during experiments.
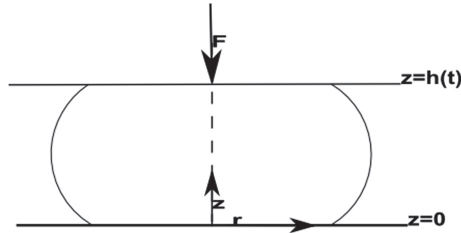

Figure 2-19: Outline of the parallel plate viscometer, the sample is placed between the two plates at z=0 and z=h(t).

Assuming creeping flow (i.e. low flow rates) and using the boundary conditions given by the parallel plate viscometer Stefan [87] first developed the theory and the following is based on the work of Bergstrøm[88], Bird et. al. [89] and Dienes and Klemm[90]. The equation of motion *(2-21)* and the mass balance for the system *(2-22)* are the starting equations.

$$\frac{\delta}{\delta t}\rho \boldsymbol{v} = -(\nabla \cdot \rho \mathbf{vv}) - \nabla p - (\nabla \cdot \boldsymbol{\tau}) + \rho \boldsymbol{g} \qquad (2\text{-}21)$$

$$0 = \frac{1}{r}\frac{\delta}{\delta r}(rv_r) + \frac{\delta v_z}{\delta z} \qquad (2\text{-}22)$$

For constant density and viscosity (incompressible fluid) the equation of motion can be simplified to

$$\rho \frac{\delta \boldsymbol{v}}{\delta t} = -\rho \boldsymbol{v} \cdot \nabla \mathbf{v} - \nabla p + \eta \nabla^2 \boldsymbol{v} + \rho \boldsymbol{g} \qquad (2\text{-}23)$$

Which is the Navier-Stokes equation for incompressible flow. Body forces such as gravity can also be neglected and for creeping flow or slow moving fluids the term v·∇v will be very small, which leaves

$$\rho \frac{\delta \boldsymbol{v}}{\delta t} = -\nabla p + \eta \nabla^2 \boldsymbol{v} \qquad (2\text{-}24)$$

A quasi stationary state is assumed, i.e. at a given time the momentum balance is given by a stationary hydrodynamic problem, while the mass balance will take changes in time into consideration. At the start of each experiment, *dv_r/dt* is not negligible and thus solutions are not applicable.

$$0 = -\nabla p + \eta \nabla^2 \boldsymbol{v} \tag{2-25}$$

in cylindrical coordinates:

$$0 = -\frac{\delta p}{\delta r} + \eta \left(\frac{\delta}{\delta r} \left(\frac{1}{r} \frac{\delta}{\delta r} (r v_r) \right) + \frac{\delta^2 v_r}{\delta z^2} \right) \tag{2-26}$$

$$0 = -\frac{\delta p}{\delta z} + \eta \left(\frac{1}{r} \frac{\delta}{\delta r} \left(r \frac{\delta}{\delta r} v_z \right) + \frac{\delta^2 v_z}{\delta z^2} \right) \tag{2-27}$$

Because of circular symmetry, v_ϕ is effectively zero. Now we consider a plane in a height h(t) from the lower plate which is moving towards the bottom plate as it is stretched in radial direction. If the radii of the sample (R) is bigger than ten times the height (h) of the sample, a good approximation is that v_z is only a function of vertical position, $v_z = f(z)$. Bergstrøm [88] use this approximation in the mass balance and the radial velocity becomes $v_r = -\frac{r}{2} \frac{dv_z}{dz}$. The momentum balance can now be simplified to:

$$0 = -\frac{\delta p}{\delta r} + \eta \left(\frac{\delta^2 v_r}{\delta z^2} \right) \tag{2-28}$$

$$0 = -\frac{\delta p}{\delta z} + \eta \left(\frac{\delta^2 v_z}{\delta z^2} \right) \tag{2-29}$$

Boundary conditions for the parallel plate viscometer are (no slip conditions):

$$v_r = v_z = 0|_{z=0}$$

$$v_r = 0|_{z=h}, v_z = \dot{h}|_{z=h}$$

The momentum equations can now be solved for v_r, v_z, and p.

$$v_r = 3 \frac{\dot{h}}{h} r \left(\frac{z}{h} - \left(\frac{z}{h} \right)^2 \right) \tag{2-30}$$

$$v_z = \dot{h} \left(2 \left(\frac{z}{h} \right)^3 - 3 \left(\frac{z}{h} \right)^2 \right) \tag{2-31}$$

$$p = C - 3\eta \frac{\dot{h}}{h^3} r^2 - 6\eta \frac{\dot{h}}{h} \left(\frac{z}{h} - \left(\frac{z}{h} \right)^2 \right) \tag{2-32}$$

Where C is a constant that may be determined from boundary conditions on the free surface. Dienes and Klemm [90] makes the assumption that v_z is negligible compared to v_r and the pressure will only be a function of radial coordinate.

$$p = p_0 + 3\eta \frac{\dot{h}}{h^3} (R^2 - r^2) \tag{2-33}$$

The force, F, on the upper plate can be found by integrating the pressure difference over the area, where p_0 is the external (atmospheric) pressure and the normal stress component τ_{zz} is 0 (Equation (2-34)) because of no-slip at the plate surface.

$$\tau_{zz} = -2\mu \frac{\partial v_z}{\partial z} \bigg|_{z=h} = 2\mu \left(\frac{\partial v_r}{\partial r} + \frac{\partial v_\theta}{\partial \theta} \right) \bigg|_{z=h} = 0 \tag{2-34}$$

$$F = \int_0^{2\pi} \int_0^R (p - p_0 - \tau_{zz}) \mid_{z=h} r \, dr \, d\theta \qquad (2\text{-}35)$$

The result being the Stefan equation which show how much force, F, must be applied to maintain the plate motion, $\dot{h}$.

$$F = \frac{3\pi\eta R^4 \dot{h}}{2h^3} \qquad (2\text{-}36)$$

For the constant volume case the Stefan equation becomes[90],

$$F_{DK} = \frac{3V^2 \eta \dot{h}}{2\pi h^5} \qquad (2\text{-}37)$$

Bergstrøm[88] proposes two approaches which does not neglect v_z but makes assumptions on the free surface of the sample to able to find C in equation $(2\text{-}32)$. The first approach is for a sample that retains its cylindrical shape and that the radii of the sample is given by constant volume ($V = \pi R(t)^2 h(t)$). The net radial force on the surface of the sample must be zero for r=R, and then the expression for the pressure becomes:

$$\int_0^{h(t)} (p - p_0 - \tau_{rr}) dz = 0 \qquad (2\text{-}38)$$

$$p = p_0 - 2\eta \frac{\dot{h}}{h} \left(1 + \frac{3(R^2 - r^2)}{h^2} - 3\left(\frac{z}{h} - \left(\frac{z}{h}\right)^2\right) \right) \qquad (2\text{-}39)$$

Using equation $(2\text{-}35)$ the force can be expressed as

$$F = \frac{3V^2 \eta \dot{h}}{2\pi h^5} \left(1 + \frac{4\pi h^3}{3V} \right) \qquad (2\text{-}40)$$

A second approach is to take into account the curvature of the surface, which may be expressed using the velocity relations equations $(2\text{-}30)$ and $(2\text{-}31)$, at r=R and that the velocity at the surface can expressed as:

$$v_r|_{r=R} = \frac{dR}{dt}$$

$$\frac{dR}{dt} = \frac{\partial R}{\partial t} + \frac{\partial R}{\partial z}\frac{dz}{dt} = \frac{\partial R}{\partial t} + \frac{\partial R}{\partial z} v_z|_{r=R} \rightarrow$$

$$v_r|_{r=R} = \frac{\partial R}{\partial t} + \frac{\partial R}{\partial z} v_z|_{r=R} \qquad (2\text{-}41)$$

$$v_r|_{r=R} = 3\frac{\dot{h}}{h} R \left(\frac{z}{h} - \left(\frac{z}{h}\right)^2 \right)$$

$$v_z|_{r=R} = \dot{h} \left(2\left(\frac{z}{h}\right)^3 - 3\left(\frac{z}{h}\right)^2 \right)$$

The solution when $h = h_0 + \dot{h}t$ and $R_{z=0}=R_{z=h}=R_0$ is:

$$R = R_0 \left(1 - 4\frac{z}{h}\left(1 - \frac{z}{h}\right)\frac{-\dot{h}}{h_0}t\right)^{-\frac{3}{4}}$$

The normal forces on the surface must balance like in equation *(2-38)* but with the above limits and the expression for the pressure, when $V = \pi R_0^2 h_0$, becomes:

$$p = p_0 + 2\eta\frac{-\dot{h}}{h}\left(1 - 3\frac{z}{h}\left(1 - \frac{z}{h}\right) + \frac{3}{2}\left(\frac{V}{\pi h^3} - \frac{r^2}{h^2}\right)\right) \qquad (2\text{-}42)$$

for the force on the upper plate:

$$F = \left(-\frac{3V^2\eta\dot{h}}{2\pi h^5}\right)\left(2 - \frac{h}{h_0} + \frac{4\pi h^3}{3V}\right)\frac{h}{h_0} \qquad (2\text{-}43)$$

Engmann, et al. [85] use the assumption with perfect slip at the plates, negligible gravity effects, and in absence of flow instability, the sample remains cylindrical during flow. According to Coussot [82] these assumption can also be used for long length samples (radius/height < 0.1). The resulting force on the plate for elongational flow (perfect slip) is:

$$F_e = \left(-\frac{3V\eta\dot{h}}{h^2}\right) \qquad (2\text{-}44)$$

Gent [91] come up with a solution where the deformation of the sample is divided into two parts; elongational flow superposed on squeezing flow. The squeezing flow part is treated as Dienes and Klemm[90] and the elongational flow is treated as above:

$$F_{sum} = \left(-\frac{3V^2\eta\dot{h}}{2\pi h^5}\right)\left(1 + \frac{2\pi h^3}{V}\right) \qquad (2\text{-}45)$$

The shear rate in the sample will be given by equation (2-46) and using equation (2-30) an expression for the shear rate is found.

$$\dot{\gamma}_{rz} = \frac{dv_r}{dz} \qquad (2\text{-}46)$$

$$\dot{\gamma}_{rz} = 3\frac{\dot{h}}{h^2}r\left(1 - 2\frac{z}{h}\right) \qquad (2\text{-}47)$$

The shear rate in the sample will range from zero in the center of the sample to a maximum value at the edge of the sample cylinder. Tørklep [86] uses the max shear rate to describe the shear rate in the sample.

$$\dot{\gamma}_{r=R,z=h} = 3\frac{\dot{h}}{h^2}R\left(1 - 2\frac{h}{h}\right)$$

$$\dot{\gamma}_{max} = \frac{3\dot{h}}{h^2}\sqrt{\frac{V}{\pi h}} \tag{2-48}$$

Bird et.al.[89] propose to use a perturbation approach to check for inertial effects on the Dienes and Klemm equation, the result being:

$$F = \left(-\frac{3V^2\eta\dot{h}}{2\pi h^5}\right)\left(1 + \frac{5\rho h(-\dot{h})}{28\eta} + \frac{\rho h^2 \ddot{h}}{20\eta\dot{h}}\right) \tag{2-49}$$

The importance of inertial effects can be estimated by calculating the size of the two last terms.

2.6.6.   POWER LAW FLUIDS

For power law fluids Scott [92] developed the theory to measure non-Newtonian viscosity of un-vulcanized rubber samples. For a fluid following the power law relationship, equation (2-5), the force on the upper plate for when the sample fills the gap between the plates becomes the *Scott equation* [89, 92]:

$$F = \frac{(-\dot{h})^n}{h^{2n+1}}\left(\frac{2n+1}{2n}\right)^n 2^{n+1}\frac{\pi k_w R^{n+3}}{n+3} \tag{2-50}$$

In addition, when the sample radius is smaller than the plates, i.e. constant volume, the *Scott equation* becomes[84]:

$$F = \frac{(-\dot{h})^n}{h^{\frac{5n+5}{2}}}\left(\frac{2n+1}{n}\right)^n \frac{2k_w V^{\frac{3n+1}{2}}}{\pi^{\frac{n+1}{2}}(n+3)} \tag{2-51}$$

With constant force the equation is an ordinary differential equation for h(t) and can be integrated from t = 0 (h = h_0) to t = $t_{1/2}$ (h = ½ h_0). Which leads to an expression for the time at half compression, $t_{1/2}$,

$$t_{1/2} = K_n\left(\frac{k_w}{F}\right)^{\frac{1}{n}}\left(\frac{V^{3n+1}}{h_0^{3n+5}\pi^{n+1}}\right)^{\frac{1}{2n}} \tag{2-52}$$

Where K_n is a constant that only depends on n.

$$K_n = \left(2^{\frac{3n+5}{2n}} - 1\right)\left(\frac{2(2n+1)}{3n+5}\right)\left(\frac{2}{n+3}\right)^{\frac{1}{n}} \tag{2-53}$$

Measurements of $t_{1/2}$ and F can then determine the power law coefficients n and k_w.

2.7.VISCOSITY OF PITCHES

For glassy solids a viscosity of 10^{12} Pa·s is often assumed to be where the glass transition temperature is, and the viscosity will be dependent on the difference between temperature and the glass transition temperature, $T-T_g$. Rand [44] has given a thorough review of the rheological aspects of pitches, and some of his findings are now presented. Nazem [93] used both a Haake rotational viscometer and a capillary viscometer to find an Arrhenius expression, Equation (2-4), for the temperature dependency of three mesophase pitches in a narrow temperature band (330-370 °C). Rand [44] states that the Arrhenius equation should only be applicable to glass forming liquids, at temperatures well above their T_g. It can be applied at temperatures 120-150 °C above T_g where the free volume is high, and the activation energy, E_a, will be dependent on molecular structure.

At lower temperature, closer to the glass transition temperature a temperature dependency based on the free volume concept is more valid. The Williams-Landel-Ferry (WLF) (Williams, et al. [94]) equation has been widely used for describing the viscoelastic properties of organic polymers, silicate glasses and organic liquids of low molecular weights. The WLF equation, shown below, can be used at temperatures up to 120-150 °C above the glass transition temperature.

$$\ln \eta = \ln \eta_r - \frac{C_{1,r}(T - T_r)}{C_{2,r} + T - T_r} \qquad (2\text{-}54)$$

Where T_r is the reference temperature and $C_{1,r}$ and $C_{2,r}$ are constants dependent on T_r, and η_r is the viscosity at the reference temperature. T_r is often set as the glass transition temperature, and Rand [44] showed that equation (2-16) describes both petroleum and coal extracts well with T_g as the reference temperature up to T_g +120. It is also shown a linear relationship between Ring and Ball softening point and T_g;

$$T_{R\&B} = 1.17T_g + 50 \qquad (2\text{-}55)$$

for petroleum and coal extract pitches. The constants in the WLF equation will therefore be different for each pitch, which is in accord with industrial experience that the viscosity-temperature relationship cannot be described by only an isoviscous temperature.

Collett and Rand [95] measured viscosities for two coal tar pitches with softening points from 83 to 101 °C with a concentric cylinder viscometer during heating. The heating rate during experiments was ca 0.4 °C/min up to 480 °C, and the temperature was measured with a thermocouple placed at the wall above the rotating cylinder. The end effect on the cylinder was corrected with correction factors found from a known Newtonian silicone liquid, and viscosity was found to be Newtonian up to 380 °C. Both the authors and Nazem [93] point out that calibration for end effects using a known Newtonian liquid may not be correct for a coal tar pitch and the temperature gradient will give a constantly changing viscosity compared to isothermal measurements. It was still found that viscosity increase fast above 420 °C, with a sudden decrease above 460 °C and a decisive increase in viscosity after this. It is suggested that at high temperatures, the anisotropic mesophase forms an emulsion with the isotropic pitch, and at the phase inversion point, the viscosity will be at a maximum.

Nazem [96] used a modified Couette instrument to measure mesophase pitches with quite high softening point and high degree of anisotropy. The modified Couette viscometer was also checked against a capillary- (Instron) and a slit- (Seiscor/Han) rheometer to check the reliability of the method. A good agreement among the three measurement principles was found for both a known Newtonian liquid (Polybuten), and the pitches used. An isotropic pitch was found to behave Newtonian 18 °C above its Mettler softening point, while it was found that for anisotropic pitches the rheological properties depend on the degree of polymerization and the nature of the precursor.

Using the Arrhenius' equation (2-4) Fitzer, et al. [97] found that several coal tar pitches had two distinct temperature regions, each with its own activation energy, E_a. The two temperature ranges was associated with first a melting region and then a softening region. The viscosity at the transition between the two regions was found to be nearly constant with a viscosity of 8-16 Pa·s, while the transition temperature was above the softening point of the binder pitch and ranged from 115-407 °C. A concentric cylinder viscometer was used in the experiments at constant temperature and varying shear rates. At each share rate, measurements were done until a steady-state torque was achieved. The isotropic pitches behave according to a Bingham plastic model, with a yield stress, whereas the anisotropic pitches was found to behave non-Newtonian below the transition temperature and Newtonian above.

Li and Li [98] found that during pyrolysis of coal-tar pitch, the viscosity will first decrease and reach a bottom at 360 – 400 °C, before the viscosity increases as the mesophase grow and coalescence. The viscosity was measured at the carbonization temperatures with a revolving viscometer, from 200 °C up to 450 °C. The coal-tar pitch used had a softening point of 81 °C and a QI content of 6.7 wt%, and viscosities in the temperature range mentioned was in the range of $2\text{-}20 \cdot 10^{-3}$ Pa·s. The decrease in viscosity with increasing temperature was attributed to more rapid thermal movement with decrease in intermolecular interaction forces and increased solubility of Benzene Insolubles (BI). It was also found that increased amounts of β-resin give smaller anisotropic domains with mesophase spheres after heat treatment of the coal tar pitch to 450 °C. Thus, β-resin seems to be the nuclei for thermal condensation and the coal-tar pitch will solidify faster and hinder growth of the anisotropic domains.

Eie, et al. [99] has also used the WLF equation to show different temperature dependency of different types of anode paste pitches in the temperature range of Søderberg anode paste mixing. The ratios $C_{2,r}/C_{1,r}$ from the fitted WLF equation could distinguish between different types of pitches, i.e. anode vacuum pitches, Cut-back pitches, and Petroleum pitches. It was also found that all pitches had Newtonian behavior in the temperature range 20-120 °C above the softening point of the pitches.

Sørlie [100] set up a relation between temperature, softening point (Mettler) and viscosity based on measurements on both heat treated and untreated binder pitches. The relationship was found to cover viscosities over 10 orders of magnitude for anode binder pitches for temperatures (in Kelvin) of ± 20 % from the pitch softening point.

$$\log \mu = 292.22 - 729.96 \left(\frac{T}{T_s}\right) + 617.60 \left(\frac{T}{T_s}\right)^2 - 177.22 \left(\frac{T}{T_s}\right)^3 \qquad (2\text{-}56)$$

where $T_s(K)$ is the softening point temperature.

2.8. VISCOSITY OF ELECTRODE PASTE

For a disperse system using petroleum coke particles and the coal tar pitch as binder, Sakai [101] found the relative viscosity to follow the Mooney equation [78] for coke content lower than 40 %. The coke used had a needle like texture and grain sizes from 44-53 μm, thus being a fines fraction. With coke content higher than 50 %, a yield stress was found for the disperse system using creep compliance testing. The relationship between viscosity at T and T_r (η / η_r) of the WLF equation is called the shift factor, α_T in the time temperature superposition principles used for polymers [102]. Sakai found that the shift factor was not dependent on the coke content of the system, thus the temperature dependence of the system is governed by the coal tar pitch used as binder. Sakai [103] also found that the shift factor was independent of the grain size distribution, when using coke sizes up to 147 μm. The coal-tar pitch was found to behave Newtonian between 40 ℃ and 150 ℃ using a cone and plate viscometer.

Tørklep [86] describes how a parallel plate viscometer can be used in production of Søderberg anode paste for aluminum electrolysis. It is shown that large samples are needed as Søderberg anode paste contains 10-15 mm coke particles and it is stated that for dense suspensions the measurement of viscosity will give a flow band opposed to the flow curve of the pitch component alone. Tørklep also found that coke fines content below 40 % follow the Mooney equation as Sakai [101] did. For an anode paste with varied granulometry and a 68.2 % solids content the viscosity is lower than a 60 % fines content, but with a higher temperature dependency.

Larsen [104] has used a parallel plate viscometer on Søderberg electrode paste cylinders. Shear rates, temperatures and dimensions of sample were chosen to resemble conditions in a full-scale electrode. It is found that electrode paste is shear thinning in this temperature (20-100 °C) and shear rate (10^{-5}-10^{-3}) region. Each temperature give a corresponding minimum sample height at the end of experiments. Larsen states that these measurements are suitable for characterizing the relationship of viscosity with parameters like binder softening point and amount of binder.

Hulse [42] used a parallel plate viscometer to examine the pitch content and fines content and fineness influence on Søderberg paste viscosity. It assumed that the material obeys the power law in this shear rate region. The maximum grain size used was 2 mm, and the temperature range 160-200 °C. It is found that viscosity increase with increasing pitch content up to a critical content, where the viscosity start to decrease. Increasing dust fineness and/or dust content increase paste viscosity as expected.

CHAPTER 3   INDUSTRIAL MEASUREMENTS

3.1. OBJECTIVE OF MEASUREMENTS

The liquid paste, as seen in Figure 3-1 , is an indication that the electrode paste may have segregated and is thus an unwanted situation. Two of three electrodes in a circular FeMn furnace have been investigated as the electrode in Figure 3-1 (electrode A) show signs of segregation whereas the other electrodes (electrodes B and C) look healthier. Better understanding of the difference between the liquid paste in electrodes A and C is pursued with measurements of temperatures. By measuring temperatures along the ribs of the casing, the impact of electrode equipment on temperatures can be found. Measurements will be compared with a computer model, and the model help verify the heating/cooling affects from electrode equipment.
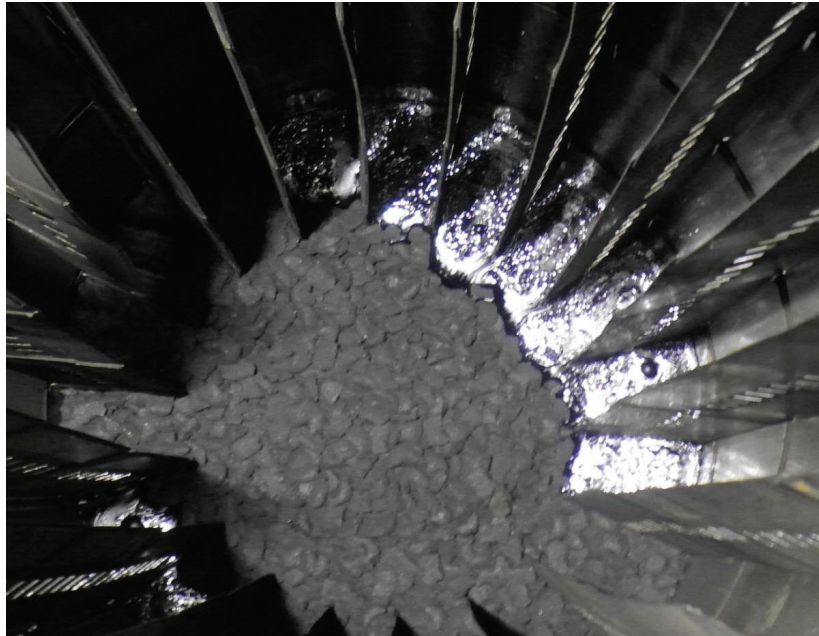
Figure 3-1: Liquid paste level and briquettes on the top of the electrode paste within the electrode casing, also shown as Figure 1-6.

During the measurement campaign, the furnace had a maintenance stop, and this gave an opportunity to measure temperatures during furnace shutdown and start-up.

3.2. EXPERIMENTAL

The set-up of the temperature measurements the furnace conditions during the measurement period is first described. More details about electrode equipment and the preparation for electrode measurement is given subsequently. Description of how measurements were done is also given. A description of the COMSOL computer model used, will finalize this section.

3.2.1.   FURNACE

The measurements were done in a three-phase circular submerged arc furnace of 35 MW producing FeMn. The furnace is closed, which means there is no stoking of the charge and combustion of gases on the furnace top. The active power of the furnace during the period of measurements are given in Figure 3-2. The time of measurements are given along with the average daily power of the furnace. The measurements were done in three periods of 2-3 days, where the furnace had a shutdown 3 April in the second period of measurements. There was also a short shutdown on the 27 March, which led to lower active power during the second measurements. The furnace power decreases in the day before the shutdown, but is around 35 MW for the other periods.
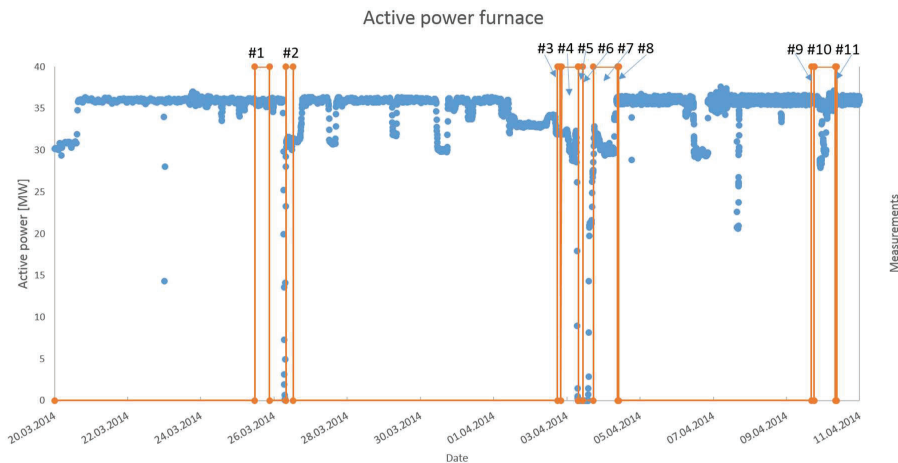

Figure 3-2. The active power of the furnace in the period of measurements.

In Figure 3-3 the current and slipping of the two electrodes, A and C, is shown in the measurement period. As part of the furnace shutdown procedure, electrode current was reduced 24h prior to the furnace shutdown. Forced slipping was used before the furnace shutdown with slipping rates up to 80 mm/h over the last 8h shift before the power cut, compared to the normal slipping rate of 20 – 30 mm/h. There are also some periods with increased slipping and reduced current, associated with forced slipping on both the 31 March and 6 April. The electrode current is slightly higher on the A electrode compared to the C electrode in the measurement period, but the difference is quite small, around 1 % of the current.
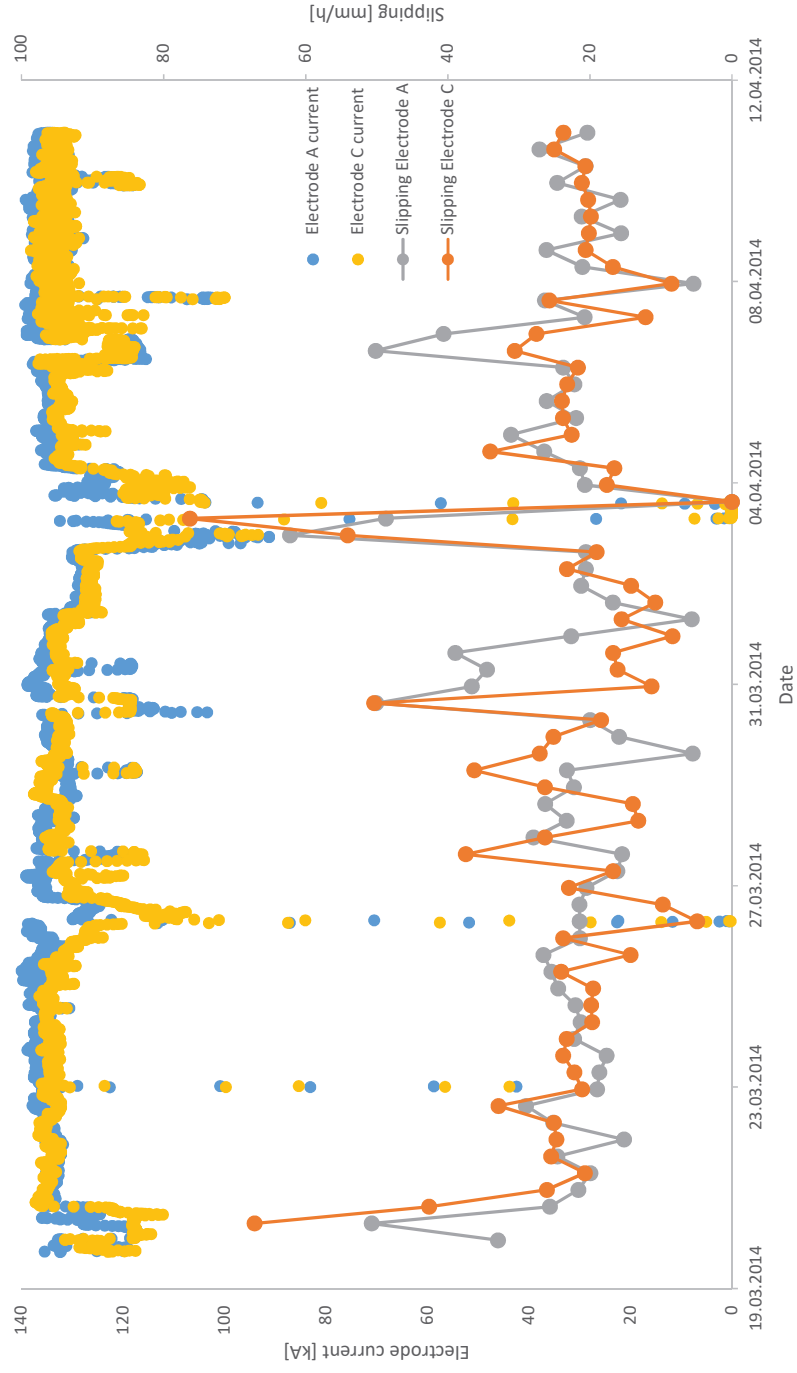
3.2 EXPERIMENTAL

Figure 3-3: The electrode current and the slipping per eight-hour period for electrodes A and C in the measurement period.

3.2.2.   ELECTRODE EQUIPMENT

The Søderberg electrodes at this FeMn furnace are 1.9 m in diameter and uses 0.9 m diameter electrode-paste cylinders. An example of electrode equipment is shown in Figure 2-5 in the Theory chapter, and the electrodes at this furnace are similar. One difference is the exit point of the heating air on the closed FeMn furnace. The heating air flows between the suspension mantle and casing and enters below the slipping equipment as in Figure 2-5, but exits from the suspension mantle above the electrode holder, just below where the current bars enter the electrode. Thus, the heating air does not cool the area most effected by induction from the current bars. For each measurement series, the height from the top of the casing to the top of the electrode slipping equipment is measured. The slipping equipment moves only during slipping and the distance from the top of the slipping equipment and down to top of the contact clamp is constant as long as the electrode is not in the process of being slipped. The distance from the top of the casing down to the top of the contact clamp is thus found for each measurement.

3.2.3.   SET-UP OF TEMPERATURE MEASUREMENTS

The measurement positions relative to the furnace and electrode is shown in Figure 3-4, where measurement positions 1-8 are placed on electrode A, and 9 and 10 on electrode C. Thus, most measurements are done on the electrode with segregation issues, and it is possible to compare measurements on the furnace center side of the electrode to the positions closer to the periphery of the furnace. Electrode A and electrode C can be compared by comparing measurements in positions 7 and 8 with positions 9 and 10. Positions 4-6 are done to compare positions close to fins with positions in-between two fins. The setup also makes it possible to access most of the positions from one side of the furnace, and the need to move measurement equipment around is reduced.
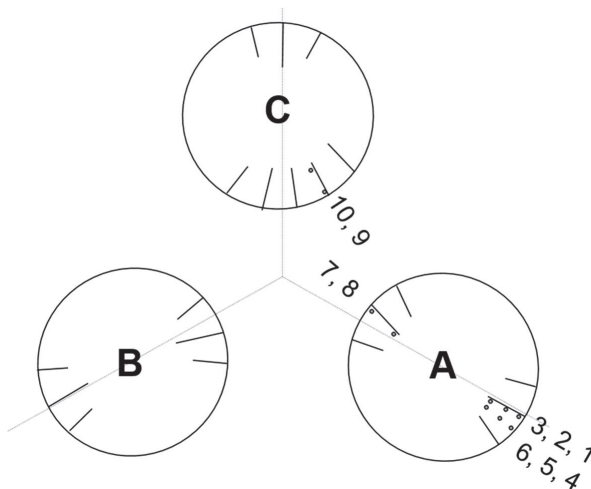

Figure 3-4: Placement of thermocouples during the measurement. Only fins essential for the measurements are shown, but fins are placed around the whole mantle.

Steel tubes were mounted on the electrode casing to be able to move the thermocouples up and down in the electrode. Oxygen lance tubes (used in the tapping) were cut in pieces of 2 m and then screwed back together during welding of new casings. This worked very well without any visible pitch leakages. In Figure 3-5 the placement of thermocouples 1-6 is shown with the steel plate that supports the tubes. The steel plate at the top was used to keep the tubes in the same position on the way down into the electrode.
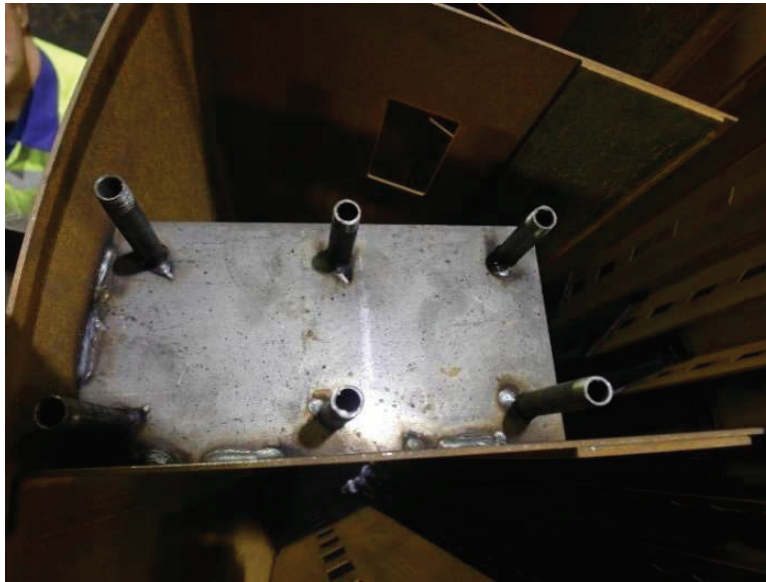
Figure 3-5: A picture of the tubes for thermocouples 1-6. The large steel plate used to hold the tubes in place was not recommended by the author. Less steel should have been used to have a more continuous carbon electrode in this area.

The steel tubes for the thermocouples were placed as shown in Figure 3-4. Tubes 1, 4, 7 and 9 were placed 2 cm from the inside of the casing, and tubes 3, 6, 8, and 10 were placed at inner side of the fin reinforcement, 26 cm from the casing as can be seen in Figure 3-5. Position 2 and 5 are in-between position 1 and 3 and 4 and 6 respectively, 14 cm from the inside of the casing. Thermocouples 1-3 and 7-10 are placed about 2 cm from the fin they are placed next to, whereas thermocouples 4-6 are placed in between two fins.

Figure 3-6 shows how tubes in positions 7-10 are mounted to the fins of the casing. The steel plate is welded to the fins to keep the tubes in place. Without the steel plate, the tubes will move during measurements and lowering the thermocouples will be more difficult.

Figure 3-6: The steel tubes for thermocouples 7 and 8 attached to the fin of the electrode casing

The list of measurements done is found in Table 3-1. The most frequent type of measurement is the temperature profile, where temperatures are measured from 4-5 m above the contact clamp down to below the contact clamp. Fixed position is a measurement where the thermocouple is held in one place as the electrode is slipped. Thus, the position is not 100 % fixed, but will follow the electrode slipping down towards the furnace. Not all positions were available for all measurements, as new casings had to be added to the electrode and some positions were removed during the measurement period.

Table 3-1: List of temperature measurements during the period.

#	Date	Measurement	Positions
1	25/3	Temperature profile	TC1-10
2	26/3	Temperature profile	TC1-10
3	2/4	Temperature profile	TC1-10
4	2/4-3/4	Fixed position	TC1-10, Overnight before furnace shutdown
5	3/4 (1)	Fixed/(semi profile) position	5 TC (1-3, 7+8) Measurements during shutdown. Profile to 3 m above baking zone.
6	3/4 (2)	Fixed position	TC 1-6, start-up of furnace. 3 TC in zone below baking zone, approx. 2h.
7	3/4-4/4	Fixed position	10 TC overnight
8	4/4	(Temperature profile)	Profile of TC1-3 taken while lifting thermocouples out of tubes.
9	9/4	Temperature profile	TC1-3, 7-10.
10	9/4-10/4	Fixed position	TC1-3, 7-10. Approximately at the top of the contact clamp.
11	10/4	Temperature profile	TC1-3, 7-10.

3.2.4. PROCEDURE FOR MEASUREMENTS

Temperature profiles of the electrodes were measured by lowering thermocouples into the tubes mounted on the casing, and stopped at set intervals to measure temperature. The thermocouples were 18 m long K-type delivered by *TC ltd*. Measurements started approximately 4-8 meters above the top of the contact clamp. Thermocouples were also maintained in fixed positions over periods to log the temperature.

The length from the top of the casing to the top of the slipping ring was measured at the start of each measurement. The height from the top of the contact clamp to the uppermost slipping ring is constant and position of the thermocouples relative to the contact clamp can be calculated. Measurements can last for hours, and slipping was taken into account as the distance between top of casing to the uppermost slipping ring decreases when the electrode is slipped.

Figure 3-7 shows the measurement log of 9 April for thermocouples 1-3. For each movement of the thermocouples the time and height of the thermocouples were noted in the logbook. The average temperature for each step was used as the temperature for a given height. Measurements were stopped when the temperature reached approximately 1000° C or it was impossible to move the thermocouple further down.
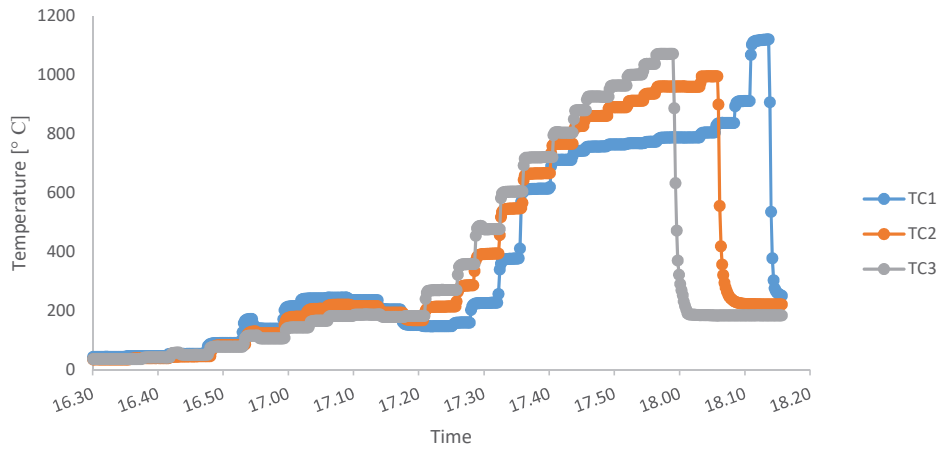
Figure 3-7: Log from data collector for TC1-3 during measurements 9. April..

From observations, the height of the paste level seemed to be different for the electrodes towards the center of the furnace compared to towards the periphery. Paste levels were measured for both center and periphery the last three measurement days. The height of paste and cylinders were recorded with a Bosch laser distance measurer.

3.2.5.　　　COMSOL

COMSOL Multiphysics have been used to model the heat transport in an electrode without fins and slipping of the electrode. The "conjugated heat transfer" mode was chosen to be able to model the effect of the heating air. Only heat transport has been included in the model, but with possibilities to add more features. The model is axisymmetric, with carbon paste in the center and casing outside the paste. To describe the thermal conductivity of the electrode paste a 4th degree polynomial function was adopted to thermal conductivity data given by McDougall, et al. [69]. For the other materials in the model, steel (Steel AISI 4340) and air, the material properties given in COMSOL is used. The model uses a stationary solver with the temperature equation given as:

$$\rho C_p \boldsymbol{u} \cdot \nabla T = \nabla \cdot (k \nabla T) + Q \qquad \text{(3-1)}$$

Where $\boldsymbol{u}$ is the velocity field, T is the temperature, C_p is the heat capacity of the material, k is the thermal conductivity and Q is heat flux. However, for the electrode paste the velocity is assumed zero and the temperature equation for electrode paste becomes:

$$0 = \nabla \cdot (k \nabla T) + Q \qquad \text{(3-2)}$$

Heat fluxes for both the inductive heating and the cooling from cooling clamps were modified to get temperature profiles similar to measurement results. The boundary conditions of heat flux and temperatures are shown in Figure 3-8. In the figure the area numbered 1 is electrode paste and the area numbered 2 is air. The temperature at the top of the casing is set to be 20 °C. The

bottom of the contact clamp is set to be the zero position in the model and the temperature at the bottom of the contact clamp is set to follow the equation

$$T_{electrode} = 1200 - 600 * r/r_1 \qquad \text{(3-3)}$$

where r is the radial position and r_1 is the radii of the casing.

The cooling effect from the contact clamps is given by

$$Q_{cooling} = h_0 \left(T - T_{coolingwater} \right) \qquad \text{(3-4)}$$

Where h_0 is the heat transfer coefficient, which is set to a very high value to model efficient cooling from the water-cooling. T is the temperature in the paste and $T_{coolingwater}$ is set to be 50 °C. The water-cooling is modelled to be effective from z = 0 at the bottom of the contact clamp and up to z_1 30 cm into the contact clamp. This was done to improve the fit of the model.

The heating from the induced current in the casing steel is not known, but a function that rises as the current bars come closer to the casing was used. The function is given in the model as

$$Q_{ind} = -\frac{2}{log_{10}\left(1.5 - \frac{z}{2.7}\right)} \qquad \text{(3-5)}$$

Where z is the vertical position. The induced heat works between z_2 and z_3 in Figure 3-8, where z_2 is the top of the contact clamp and z_3 the position where the current bars come close to the electrode casing.
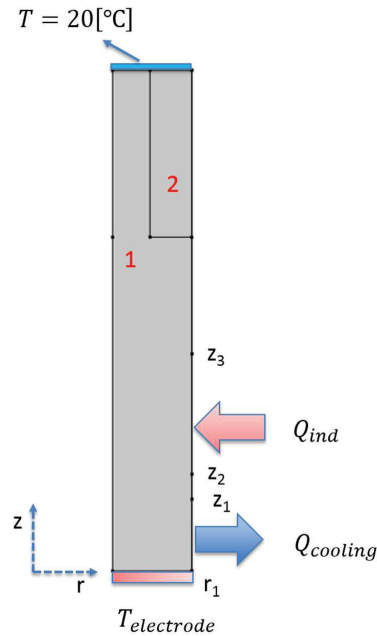

Figure 3-8: Heat flux and temperature input to the COMSOL model.

3.3.RESULTS OF MEASUREMENTS

Liquid paste level and level of cylinders is shown in Figure 3-9, where the liquid paste level was recorded at the periphery side of the electrode. In the A electrode, the liquid paste level dropped during the measurement period, while the cylinder height varied more. For electrode C, the liquid paste level was at a constant level, except from the day of the furnace shutdown when both liquid paste and cylinder level was low.
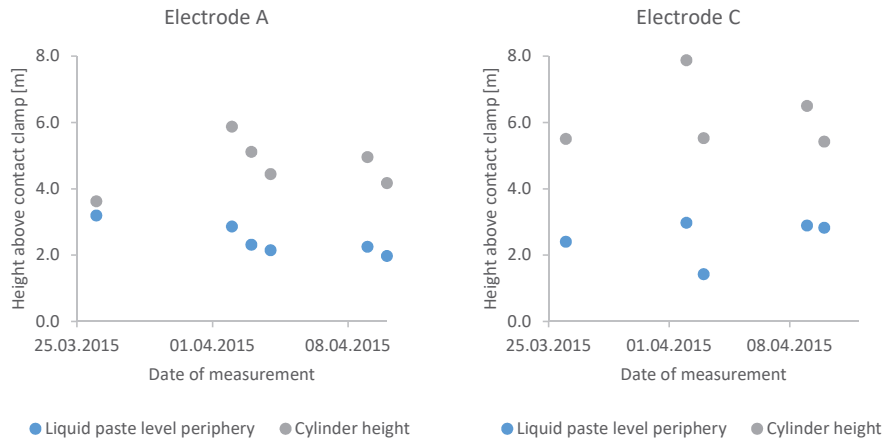

Figure 3-9: Liquid paste and cylinder level of electrode A and C during measurement period.

3.3.1.   TEMPERATURE PROFILES

The temperature profiles from measurements are shown in Figure 3-11 for positions 1, 7 and 9, with measurements # 1, 2, 3, 9 and 11 from Table 3-1. The general form of the temperature profile is best seen in Figure 3-10 for thermocouple position 1. The temperature in the upper part of the casing is around room temperature, 22 °C, and increases slowly up to 40 °C at around 3 m above the contact clamp. Between 2 and 3 m the temperature rises up to about 80 °C before it continues to rise up to a peak in the area 0.0 – 0.25 m above the contact clamp tip. The temperature in this peak can reach temperatures above 250 °C for position 1 on measurement #3 in Figure 3-10, while the temperature is lower for positions 7 and 9.

The temperature drops slowly when coming into the contact clamp, before it quickly rises in the lower half of the contact clamp. The temperature will rise from about 150 °C and up to ~700 °C or more within 20 cm of vertical movement. The general form of the temperature profile is the same for all positions with some variations that will be presented in the following sections.

EVOLUTION OF TEMPERATURES DURING MEASUREMENT PERIOD.

Figure 3-10 shows that temperature increase more 2m above the contact clamp for the three earlier measurements (#1-3) compared to the later (#9 & #11). At the bottom of the contact clamp the two first measurements (#1 and #2) has the steep temperature increase lower than the later measurements (#3, #9 and #11). At TC7 there is no consequent trend in the temperature profiles during the measurement campaign.

On electrode C, TC9 is cooler 1m above the contact clamp and higher in the first measurement period (measurements #1 and #2) compared to later measurements (#3, #9, and #11).
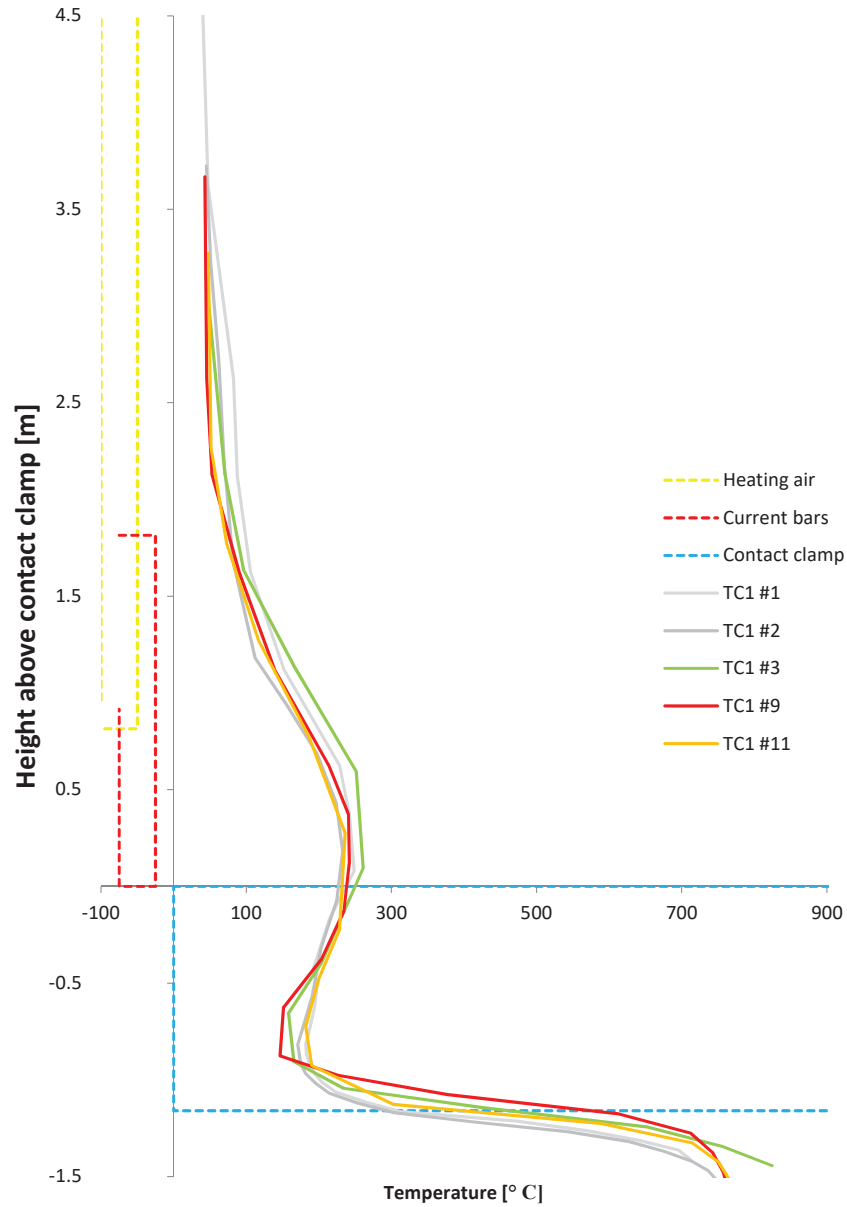

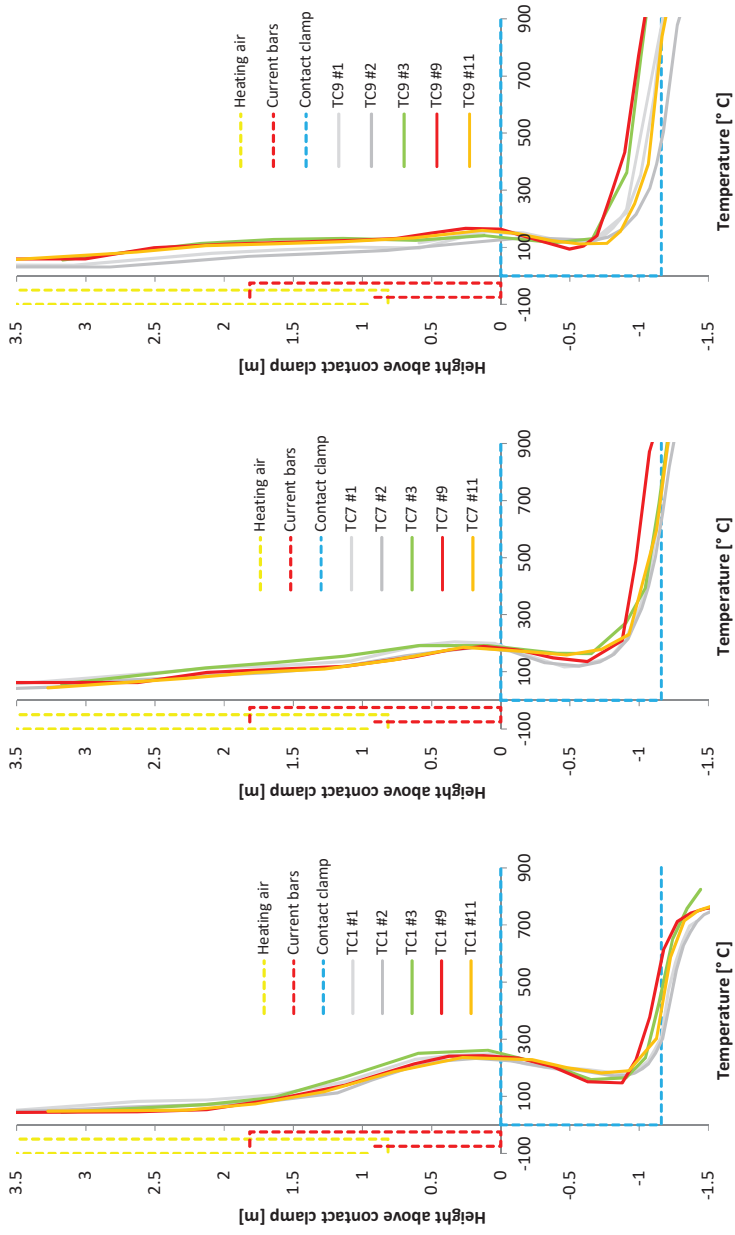*Figure 3-10: Temperature profiles for the whole measurement period for position 1.*

Figure 3-11: The evolution of temperature profiles during the measurement period, with measurement numbers from Table 3-1.

TEMPERATURES WITH INCREASING DISTANCE FROM THE ELECTRODE CASING

In Figure 3-12 temperature profiles for positions with increasing distance from the casing is shown for positions 1-3 and 4-6. The temperatures in the three different radial positions are alike from high in the electrode and down to 1.5 m above the contact clamp tip. Closer to the contact clamp the temperatures are higher closer to the casing than towards the center of the electrode. Moving into the contact clamp the situation is reversed as the positions closest to the casing is cooler at about 0.4 m into the contact clamp. The temperature closest to the center of the electrode start to rise earlier than close to the casing as it is not affected by the cooling in the contact clamp as much as close to the casing. The difference between position 2 and 3 (5 and 6) is small compared to the difference between 1 and 2 (4 and 5) as the temperature rises in the lower part of the contact clamp. Close to the casing, the electrode paste leaves the contact clamp with a temperature below 500 °C, but in this area the temperature rise quickly.
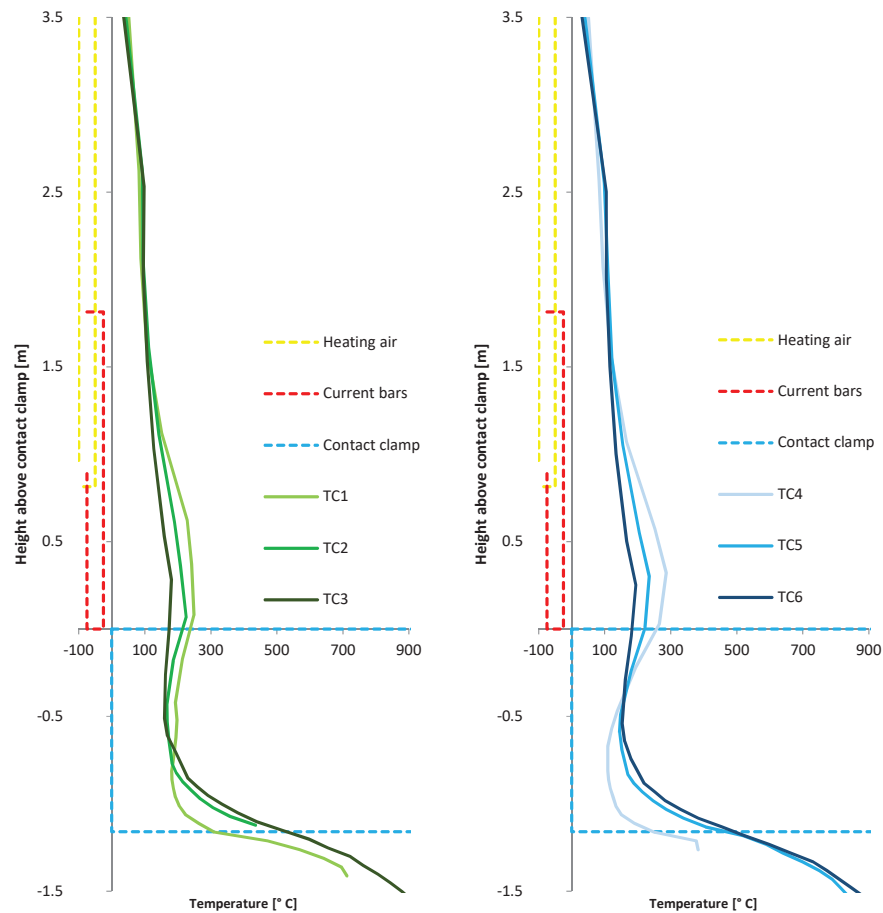

Figure 3-12: Temperature profiles of positions 1-3 and 4-6 for measurements #1.

The temperature profiles for different radial positions for the part of the electrode facing the center of the furnace is shown in Figure 3-13. The temperature profiles are similar to the ones found in Figure 3-12. However, temperatures close to the casing are distinctly higher compared to temperatures towards the center of the electrode above the contact clamp and up 2.5 m. Towards the center of the electrode (TC8 and TC10) there no clear peak above the contact clamp tip, as seen for the positions closer to the casing (TC7 and TC9). For both positions, close to casing and close to the center of the electrode, temperatures rise quickly in the lower part of the contact clamp and reach temperatures well above 500 °C before leaving the contact clamp.
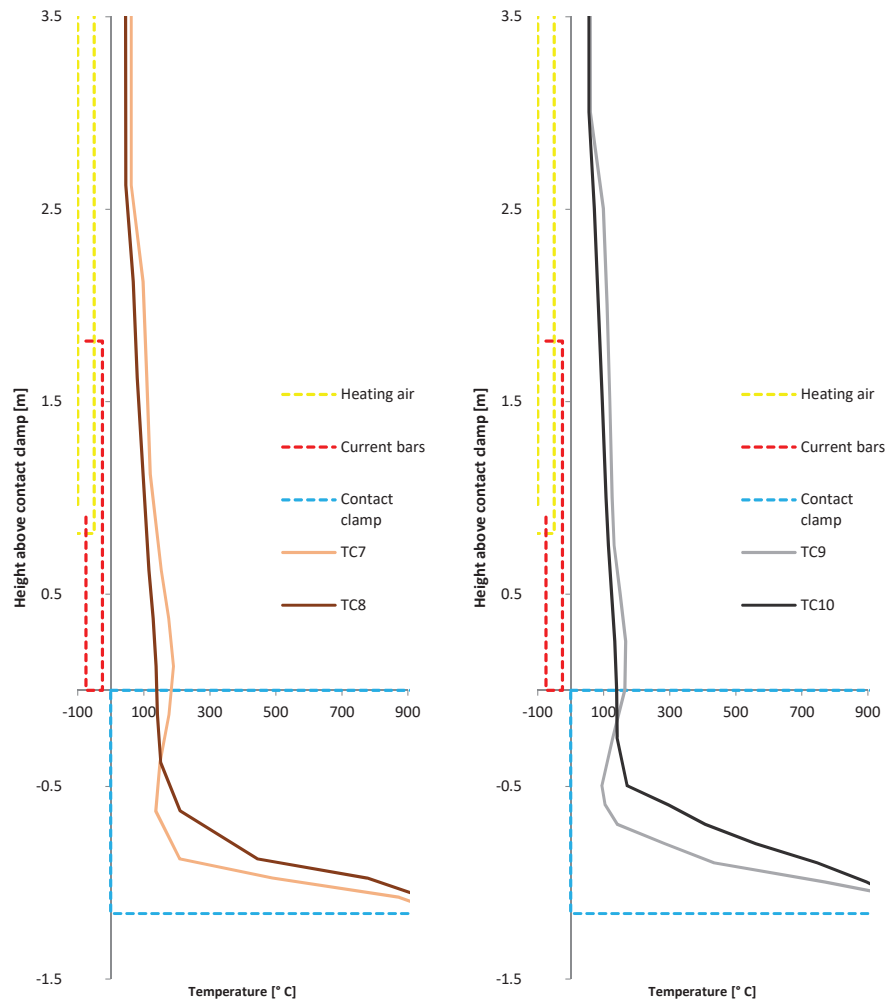

Figure 3-13: Temperature profiles for thermocouples 7 & 8 and 9 & 10 for measurement #9.

TEMPERATURE DIFFERENCE BETWEEN POSITIONS AT FINS AND IN-BETWEEN FINS.

In Figure 3-14 the temperatures of thermocouples in position 1-3, close to the fins, is compared to thermocouples in position 4-6 in-between fins. The temperatures in the two different positions are similar up to the area of the temperature peak above the contact clamp, where the temperature is higher for the position in-between the fins. The temperature in the in-between position peaks at around 280 °C at this position, compared to around 240 °C for the position along the fin. When entering the contact clamp, the temperature in-between the fins falls faster and lower than the thermocouple position beside the fin. The temperature difference between the two positions closest to the casing is around 50 °C at the low point. As temperature rises in the bottom of the contact clamp, temperatures at the same radial positions are similar when comparing the measurements at the fins and in-between fins. Differences between the two positions become smaller for positions closer to the center of the electrode, and the difference between position 3 and 6 is insignificant. Heat transfer is larger in the steel fins compared to paste. Heat transfer along the fins in vertical direction will make temperatures more stable along the fins compared to the in between position. Thus, temperatures close to the casing will be more influenced in the in-between position with heating coming from induced current and contact clamp cooling water close to the casing. However, as heat transfer is slow in the radial direction in paste, the temperatures close to the electrode center will be more stable.

TEMPERATURE DIFFERENCE BETWEEN POSITIONS TOWARDS THE PERIPHERY AND CENTER OF THE FURNACE

Positions towards the periphery and the center of the furnace is compared in Figure 3-15, where temperatures are higher for positions towards the center of the furnace high in the electrode column. The difference is bigger close to the casing (TC1 and TC7) compared to closer to the center of the electrode (TC3 and TC8). 0.5 m above the contact clamp, the temperature peak is higher for the periphery positions (TC1 and TC3) compared to the positions towards the center of the furnace (TC7 and TC8). This is probably due to the distance to or the amount of current in the nearest current bar. That is the position in the periphery is closer to a current bar (or a current bar with higher current) than the position close to the electrode center.

The temperatures are higher in the periphery positions until the temperature rises earlier for positions towards the center of the furnace. The temperatures are higher towards the center of the furnace for the rest of the measurement interval, and temperatures are above 700 °C when the electrode leaves the contact clamp for in the positions oriented to the center of the furnace.
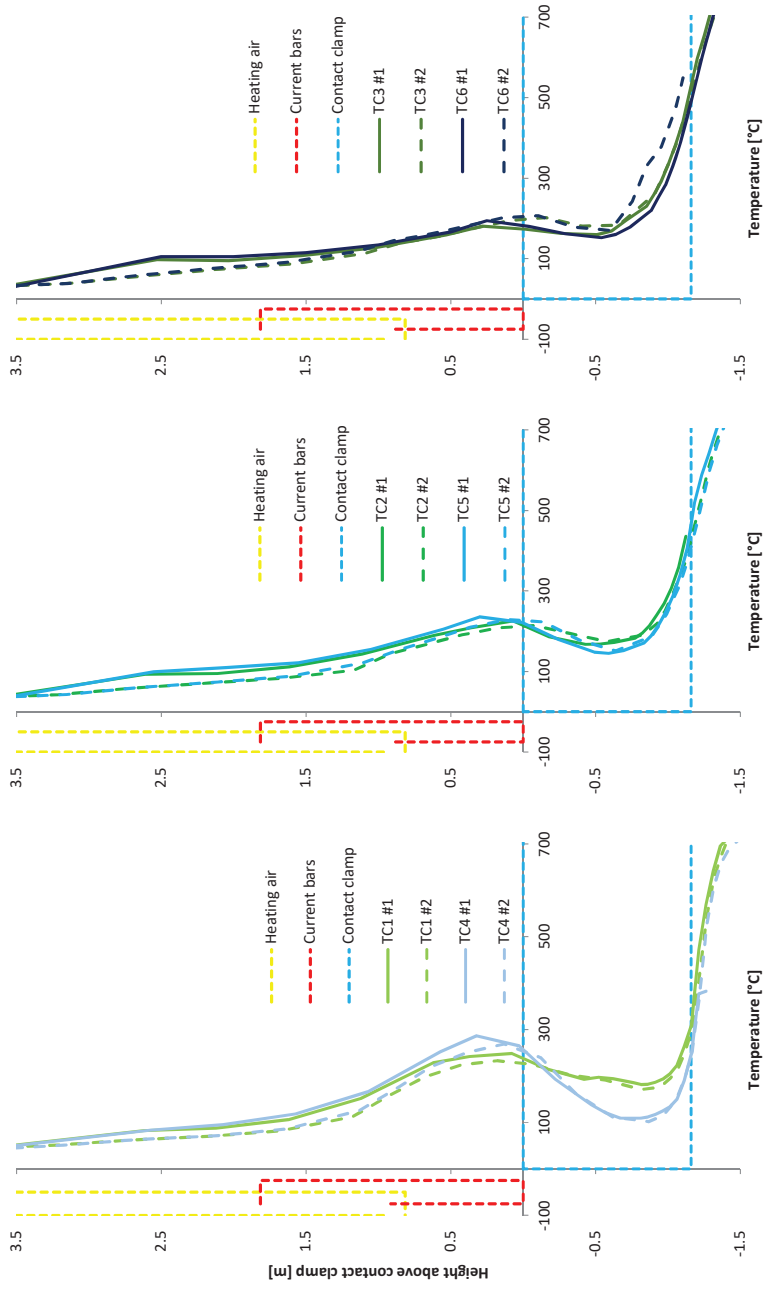
Figure 3-14: Comparison of temperature development in different positions on electrode A. Yellow dotted line depicts the position of the heating air. Red dotted line is the area where the bus tubes are close to the electrode. Blue dotted line show the contact clamps
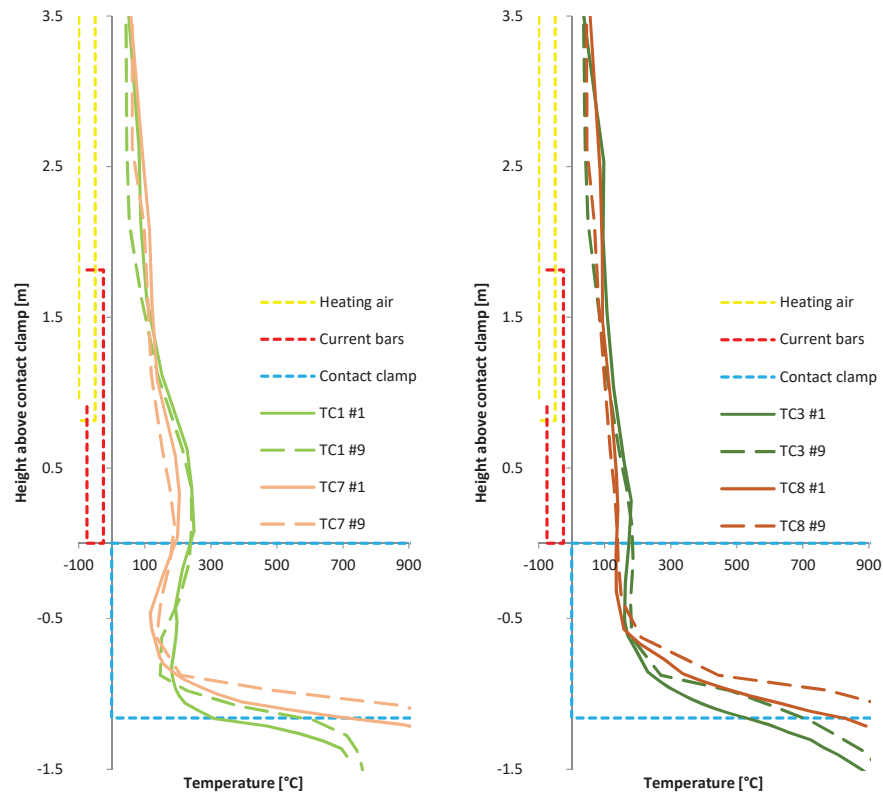
Figure 3-15: Temperature profiles for positions towards the periphery (TC1 and TC3) and the center (TC7 and TC8) of the furnace for measurement #9.

TEMPERATURE DIFFERENCE BETWEEN ELECTRODE A AND C

All temperature profiles for measurements on electrode A and C are shown in Figure 3-16. Measurements close to the casing (TC7 and TC9) are similar up to the temperature peak around 0.5 m above the contact clamp, where electrode A is hotter than electrode C. Further into the contact clamp, no consistent difference between the two electrodes can be seen close to the casing. Measurements closer to the electrode center /TC8 and TC10) are not distinguishable from one another for most of the measurement interval. Small variation in measurements are seen above the contact clamp, but within the lower parts of the contact clamps variation between measurement periods is larger. Temperatures during measurements #3 and #9 on electrode C rise earlier than measurements on electrode A.
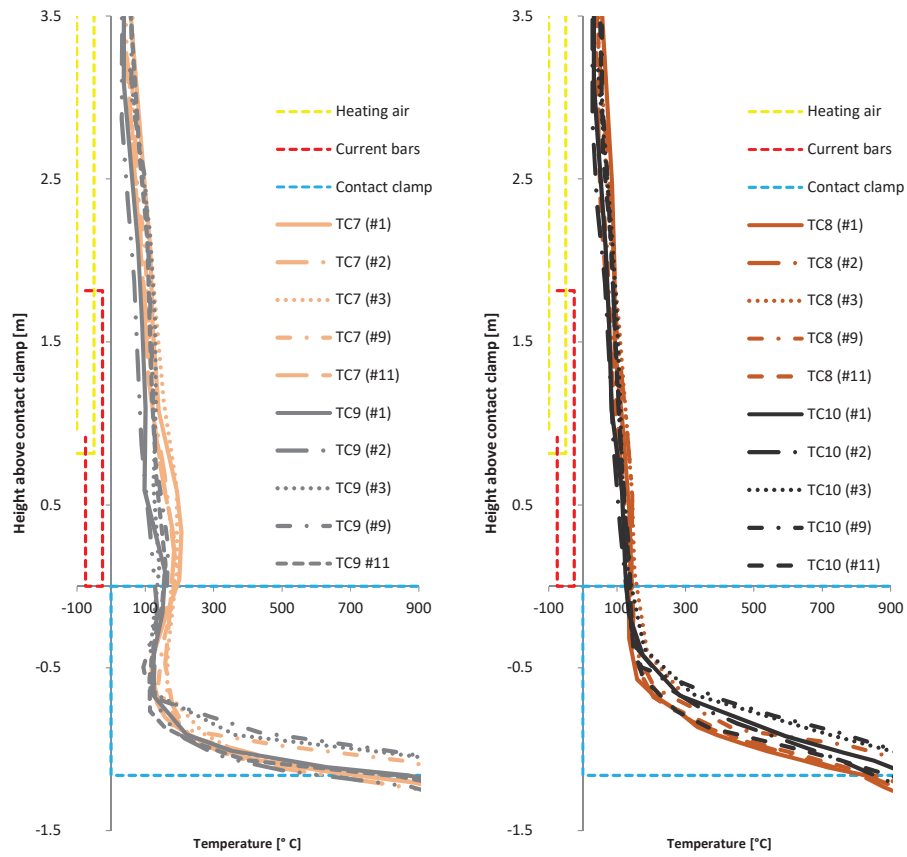
Figure 3-16: All temperature profile measurements for thermocouples in electrode A (TC7 and TC8) and electrode C (TC9 and TC10).

In Figure 3-17 the minimum and maximum values for the temperature profiles are plotted to give a band for within all measurements in the given position would lie. The difference between minimum and maximum temperatures is small above the contact clamp, but increase in the lower parts of the contact clamp. The temperature as the electrode paste leaves the contact clamp is between 200 and 600 °C close to the casing (TC1), and 420 – 700 °C closer to the electrode center (TC3). Measurements taken in a constant position relative to the casing is also shown laying within the temperature band given by profile measurements. The position of the overnight measurement (Measurement #4 in Table 3-1) moves down as the electrode is slipped, and stay within the temperature band for all positions.
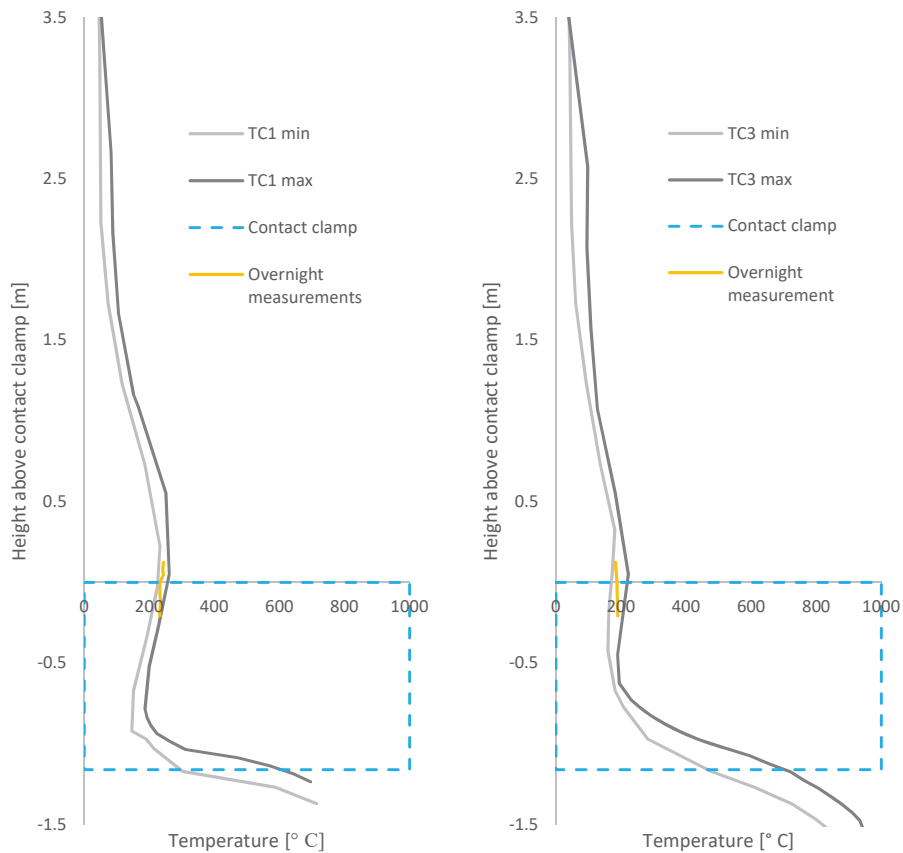

Figure 3-17: Overnight measurements on electrode A in position 1 and 3 with the temperature profile interval.

Figure 3-18 shows the temperature interval from all measurements done with indication to where electrode paste and equipment is situated. The temperature rises to about 70-80 °C as the melted paste level is reached. Further down the electrode, the temperature will rise to a local maximum above the tip of the contact clamp. Inside the contact clamp temperature decreases as the paste is cooled by cooling water in the contact clamps, before it rises rapidly in the baking

zone. The electrode in Figure 3-18 shows measurements done 2 cm from the steel casing, the red vertical line in the figure indicate this position.
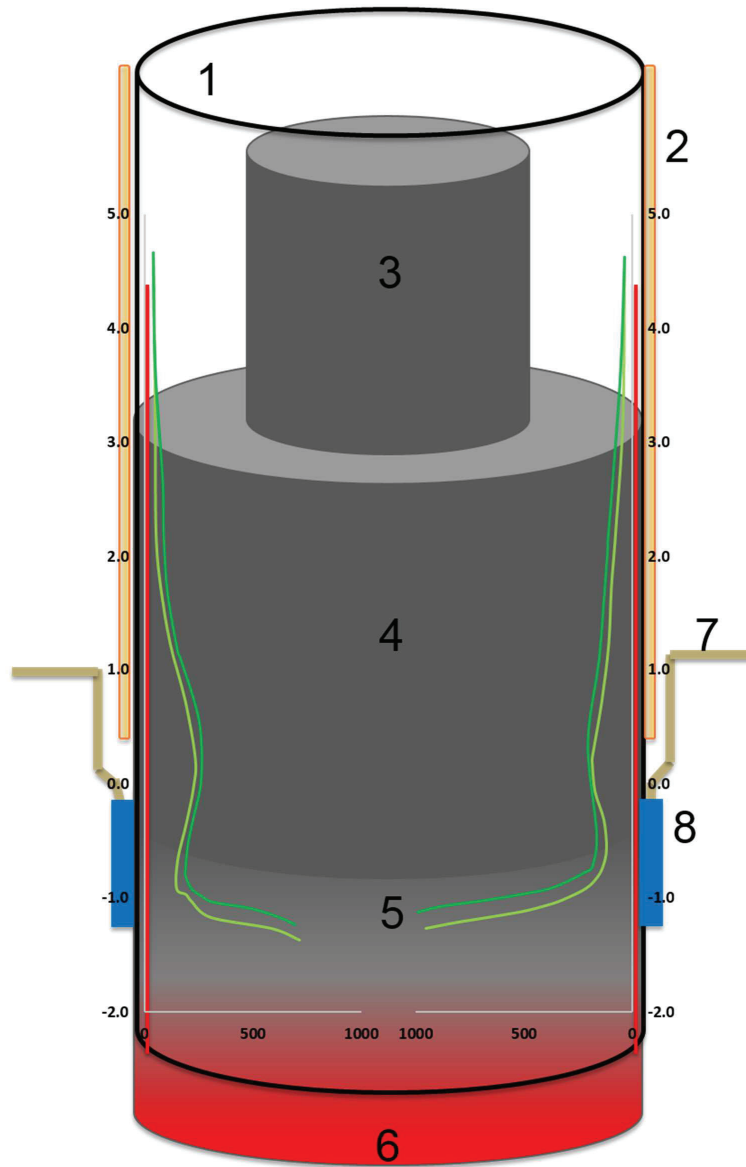

Figure 3-18: The temperature profiles from the measurements are shown in green as temperature bands. The red vertical line indicates where the measurements are done, i.e. two centimeters from the casing. The measurements on the left are towards the furnace periphery and on the right are towards the furnace center. The numbers indicating the following: 1. Casing. 2.Heating air. 3. Electrode paste cylinder 4. Melted electrode paste. 5. Baking zone of electrode paste. 6. Hot solid electrode (Electrode casing is burnt off). 7. Current bars. 8. Contact clamps.

3.3.2. FURNACE SHUTDOWN

Measurements before, during and after the shutdown (Measurements #4-8) are shown with temperature bands in Figure 3-19 for thermocouple positions 1 and 3. The green lines show temperatures in the lower part and below the contact clamp in the hours before the shutdown on April 3. The temperatures start within the normal temperature band, as the electrode is slipped temperatures in both position TC1 and TC3 fall beneath the band.

The blue temperature profiles in Figure 3-19 are recorded around 3h into the shutdown. For TC1 the temperatures stay below the normal borders in the whole measurement range. However, closer to the center of the electrode, i.e. TC3, the temperatures have not decreased as much. In the temperature trough 0.5 m below the contact clamp tip the temperature was within the range of profile measurements. The same can be seen approximately 0.8 m above the contact clamp.
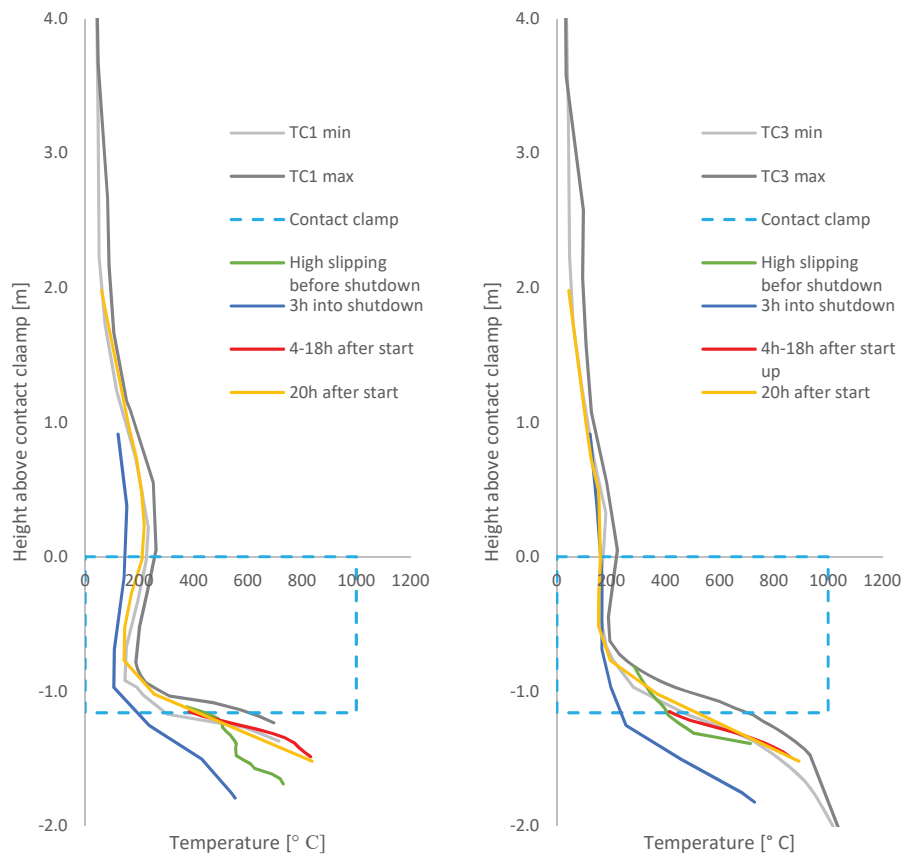

Figure 3-19: Minimum and maximum temperature profiles for thermocouple 1 and 3 with measurements done overnight and during furnace shutdown

During furnace start-up, the red lines in Figure 3-19, temperatures were recorded from 4h after start-up and until 18h after start-up. Close to the casing, the temperatures of TC1 during furnace start-up are tangent to the minimum temperature profile line in Figure 3-19. Closer to the electrode center the temperatures does not rise as fast during start-up, but the distance between the minimum temperature profile and the start-up measurement is diminishing towards the end of the measurement.

The yellow line shows a profile 20h after start-up, with temperatures in the lower end and below the temperature band for normal furnace operations. 1 m below the top of the contact clamp temperatures rise earlier than normal, and in a small region, temperatures are in the upper part of the normal temperature band. Below the contact clamp, temperatures are lower than normal.

Measurements before, during and after the shutdown (Measurements #4-8) are shown with temperature bands in Figure 3-20 for thermocouple positions 4 and 6. The green lines show temperatures in the contact clamp in the hours before the shutdown on April 3. For the position closest to the casing, temperatures are higher than normal in the area where the temperature decrease within the contact clamp. Further into the electrode (TC6), temperatures are higher than normal as long as temperature decreases within the contact clamp. As temperature starts to rise in the lower part of the contact clamp, the temperature during high slipping are lower than normal.

In Figure 3-20 temperatures were recorded from 4h after start-up and until 18h after start-up with a red line in the area around the contact clamp tip. Temperatures above the contact clamp tip are lower than normal, but as the position of the thermocouples is slipped into the contact clamp the temperatures normalize. The position closest to the center of the electrode approaches normal conditions, but is not within the normal temperature band 18h after start-up. The yellow line shows profiles 20h after start-up, with temperatures in the lower end and below the temperature band for normal furnace operations.
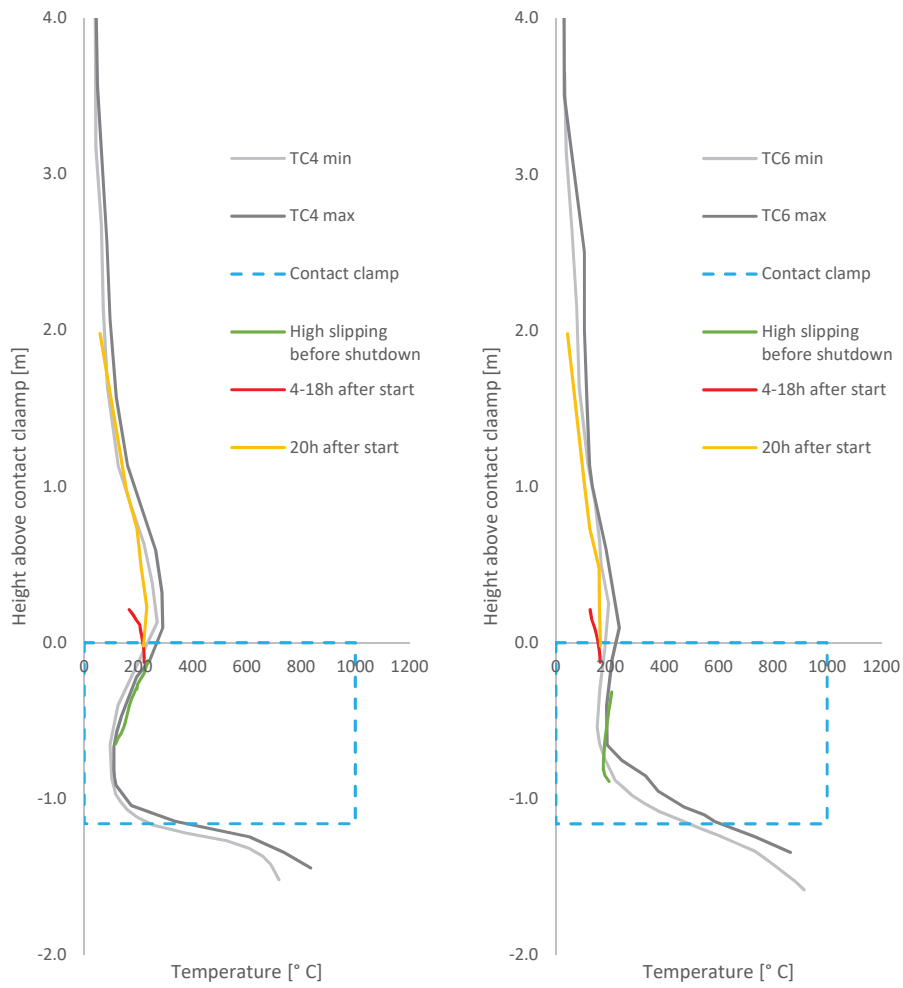
Figure 3-20: Minimum and maximum temperature profiles for thermocouple 4 and 6 with measurements done overnight and during furnace shutdown.

Measurements before, during and after the shutdown (Measurements #4-8) are shown with temperature bands during normal furnace operations in Figure 3-21 for thermocouple positions 7 and 8. The green lines show temperatures 2-2.5 m above the contact clamp in the hours before the shutdown on April 3. The temperature stays within measurements done at normal operations in the hours before the shutdown for positions 7 and 8.

The blue line in Figure 3-21 shows a temperature profile 1h into the furnace shutdown. Above the contact clamp, temperatures are close to normal until the last 0.5 m above the contact clamp tip, where temperatures are lower than normal for the position closest to the casing. In the colder parts of the contact clamp, temperatures are close to normal, but temperatures rise lower in the

contact clamp than normal. Closer to the electrode center temperatures are close to normal until the lower parts of the contact clamp, where temperatures rise lower than normal.

In Figure 3-21 temperatures were recorded from 4h after start-up and until 18h after start-up with a red line in the area around the contact clamp tip. Temperatures are lower than normal for both positions, but closer to the center of the electrode, temperatures are further away from normal.
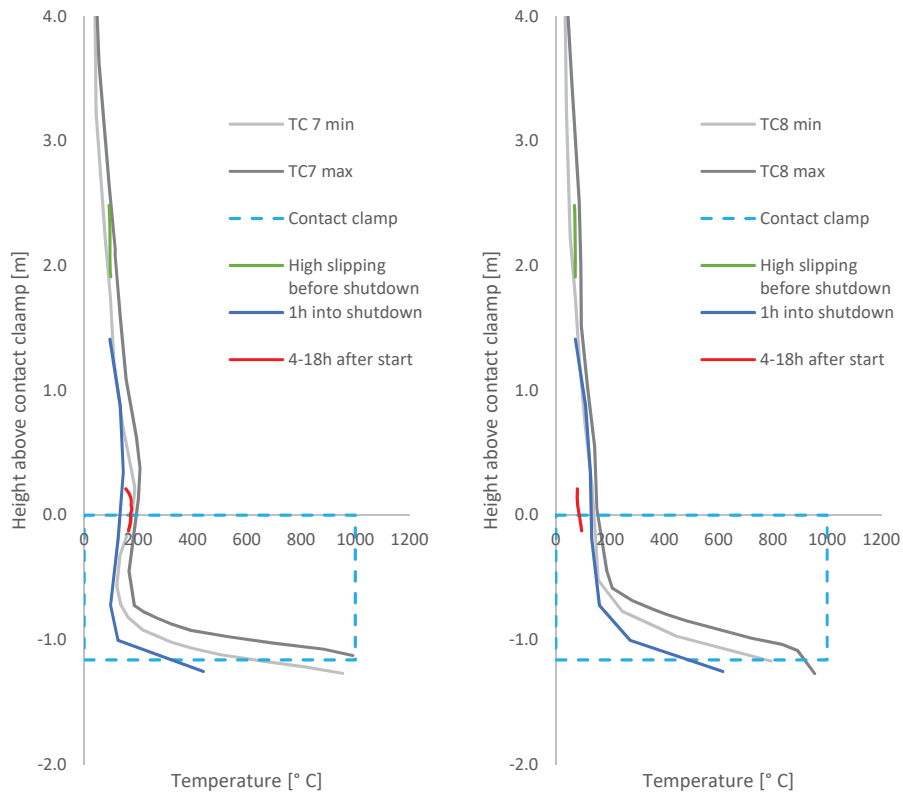

Figure 3-21: Minimum and maximum temperature profiles for thermocouple 7 and 8 with measurements done overnight and during furnace shutdown

Measurements before, during and after the shutdown (Measurements #4-8) are shown with temperature bands during normal furnace operations in Figure 3-22 for thermocouple positions 9 and 10. The green lines show temperatures 1-2 m above the contact clamp in the hours before the shutdown on April 3. The temperature stays in the higher temperature end of measurements done at normal operations in the hours before the shutdown for positions 9 and 10.

In Figure 3-22 temperatures were recorded from 4h after start-up and until 18h after start-up with a red line in the area around the contact clamp tip. Temperatures are lower than normal for both positions, but closer to the center of the electrode, temperatures are further away from normal operation temperature.
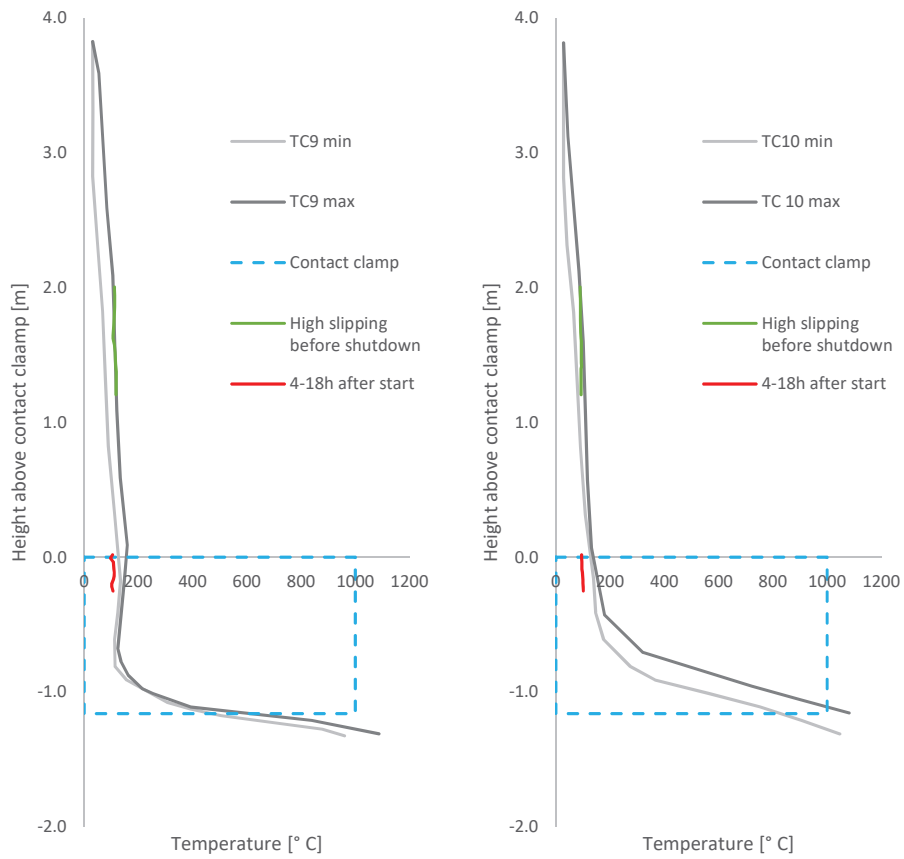
Figure 3-22: Minimum and maximum temperature profiles for thermocouple 9 and 10 with measurements done overnight and during furnace shutdown.

3.4.DISCUSSION

3.4.1.　　　　TEMPERATURE PROFILES

The liquid paste level on electrode A is decreasing during the measurement period, as seen in Figure 3-9, and in Figure 3-10 measurements #1-3 rise to 80 °C before measurements # 9 and 11. The rise in temperature from 40 to 80 °C seems to be correlated with the paste level. In electrode C the same can be observed with the lowest paste level for measurements #1 and 2, while higher paste level for measurements # 3, 9 and 11, and higher temperatures for measurements # 3, 9 and 11 2m above the contact clamp in Figure 3-11. Thus, the temperature of the paste will reach 80 °C or above as it flows out to the casing.

The temperature profiles found in Figure 3-10 and Figure 3-11 show how the temperature evolves as thermocouples are lowered towards the furnace inside the casing. The temperature first increase due to the heat from the heated air that blows alongside the casing on the outside. The next rise in temperature is found when the thermocouples go into the liquid paste, which has a temperature of 60 – 90° C. The temperature then rise faster in the area where the current bars come closer to the casing and go into the contact clamp. The temperature rise is produced from resistive heating by an induced current in the electrode casing caused by the current bars.

As the electrode paste enters the contact clamp, the water-cooling will cause the temperature to fall in the upper part of the contact clamp. The measured temperature drop is in accordance with previous temperature measurements by Olsen, et al. [58] and Innvær, et al. [61]. As the electrode paste is slipped further down into the contact clamp, the resistive heating from the electrode current entering the baked electrode and to some extent the heat from the furnace is the reason for the high temperature increase in the lower parts of the contact clamp.

The induced heating above the contact clamp is not an ideal temperature profile for electrode paste baking, as the electrode paste has a relative low viscosity at 200 – 250 °C which may lead to pitch/fines mixtures segregation from the coarser filler material (Elkem-Carbon [14]). Temperatures in this area has been measured at temperatures 286 °C, in TC4 in Figure 3-12. Evaporation of low molecular weight species might take place around temperatures of 300 °C. These species can rise in the electrode and mix with electrode paste higher in the column, and as the low molecular weight species content increase in the electrode paste, the softening point and viscosity of the binder will decrease. This is believed to be one of the causes to segregated paste, as seen in Figure 3-1. To reduce the unwanted heating in this area increased amount of "heating" air will help cool the casing above the contact clamp. If increase in "heating" air does not solve the problem, installment of induction shields (e.g. copper), has been effective Gunnlaugsson, et al. [105].

TEMPERATURES WITH INCREASING DISTANCE FROM THE ELECTRODE CASING

When comparing temperatures in different radial positions in Figure 3-12, for placements towards the periphery of the furnace, there is a small difference high in the electrode column as there is little heating from outside the casing. For positions towards the center of the furnace, in Figure 3-13, the position close to the casing is hotter than the position closer to the center of the electrode, as the hot furnace gases leaves in the center part of the furnace. Further down the

electrode column, the temperature peak above the contact clamp decreases with increasing distance from the casing, as shown in Figure 3-12 and Figure 3-13. As the heat source above the contact clamp is heat from induced current in the casing it is clear that the temperature should fall as the distance to heat source increases.

Within the contact clamp, the reduction in temperature decreases with distance to the water-cooled contact clamp. The positions towards the center of the electrode, positions 2 & 3 and positions 5 & 6, the temperature starts to rise earlier than for the position closest to the casing (positions 1 and 4). The positions towards the center of the electrode will be less affected by the water-cooled contact clamp, as well as the center of the electrode being hotter than the periphery in the furnace (Innvær, et al. [59]). The efficiency of the cooling in the contact clamp is good as the temperatures in position 1 and 4 is as low as 300 °C when the electrode leaves the contact clamp. For positions towards the center of the furnace, positions 7-10 in Figure 3-13, the temperature rise closer to the contact clamp top for position 8 and 10, compared to position 7 and 9 closer to the casing. The temperature as the electrode leaves the contact clamp is above 500 °C for all measurements in positions 7-10.

TEMPERATURE DIFFERENCE BETWEEN POSITIONS AT FINS AND IN-BETWEEN FINS.

The difference between positions besides the fins and in-between fins can be seen in Figure 3-14, where there is a small difference in the upper part of the electrode for all radial positions. However, above the contact clamp the positon in-between fins is markedly higher than the position besides the fin close to the casing. As can be seen in Table 3-2 the thermal conductivity in steel is much higher than both unbaked and baked electrode paste, hence the fins will conduct heat better both radially and vertically compared to pure electrode paste. The vertical heat transport in the fins makes the peak above the contact clamp lower as heat is transported away from this area, making the temperature low-point in the contact clamp hotter for the position besides the fin compared to the position in-between fins. The measurements show that the temperatures in-between fins are around 50 °C lower than the temperature besides the fin at the low point within the contact clamp.

Table 3-2: Thermal properties of steel and electrode paste, data from Elkem-Carbon [14] and McDougall, et al. [69].

	Thermal conductivity [W/mK]
Steel [20°C]	52
Steel [500 °C]	39.3
Electrode paste[20 °C]	2.5
Baked paste [500 °C]	6.8
Baked paste [1000 °C]	19.2

TEMPERATURE DIFFERENCE BETWEEN POSITIONS TOWARDS THE PERIPHERY AND CENTER OF THE FURNACE

In Figure 3-15, where the positions on the periphery side is compared to positions towards the furnace center, the electrode paste is hotter on the center side high in the electrode column. The heat loss from the center of the furnace will be lower than on the periphery side, as all three electrodes heat up the surroundings in the center. The difference between the positions is thus biggest closest to the casing.

Above the contact clamp, the periphery side is hotter than the center side. The alternating current in the current bars entering the contact clamps will induce Eddy currents in the casing, which will heat the casing through resistive heating. The induced current will be dependent on, among other things, the amount of current in the current bar and the distance between the casing and the current bar. Thus, the heating effect will vary around the circumference of the electrode and some differences in temperatures in this area can be expected.

TEMPERATURE DIFFERENCE BETWEEN ELECTRODE A AND C

In Figure 3-16, temperature profiles measurements comparing electrode A and electrode C are compared, and for positions close to the electrode center (TC8 and TC10), the differences are small. Close to the casing, electrode A is hotter in the area from the contact clamp tip and up to 1 m above the tip, the area heated by induced currents from the current bars. The argument made in the previous paragraph, with induced eddy currents, will also explain differences between the two measuring positions on different electrodes. The temperatures stay higher in electrode A the first 30 cm into the contact clamp as well. As the difference is caused by the distance to the nearest current bar, these differences are not an evidence of the differences in segregation behavior between the two electrodes. For the other places differences between electrodes A and C are not consistent during the measurement period.

ISOTHERMS IN ELECTRODE A

To find the position of isotherms a curve fitting procedure in Sigmaplot™ is used. The measurement data are plotted as shown in Figure 3-23. Note that in Figure 3-23 the y-axis is temperature, and the x-axis is the height above the bottom of the contact clamp, not the contact clamp top as in previous figures. Then curve fit in Sigmaplot™ is used to find a rational expression with 7-10 parameters, e.g. Equation (3-6) with 10 parameters where x is the height above contact clamps and Y is the temperature.

$$Y = \frac{a + bx + cx^2 + dx^3 + ex^4}{1 + fx + gx^2 + hx^3 + ix^4 + jx^5} \qquad (3\text{-}6)$$

With this model for the temperature, the position of isotherms can be found solving Equation (3-6) with respect to x. The Solver add-in in Microsoft Excel is used to find the height, x, for each isotherm temperature Y. This is done for positions 1-3 and 7-8, from the temperature profile measurements, and then the average height of each isotherm is given in Table 3-3. For

positions #3 and #7 there is only one model that give three positions for the 200 °C isotherm and thus the standard deviation for these positions cannot be calculated.
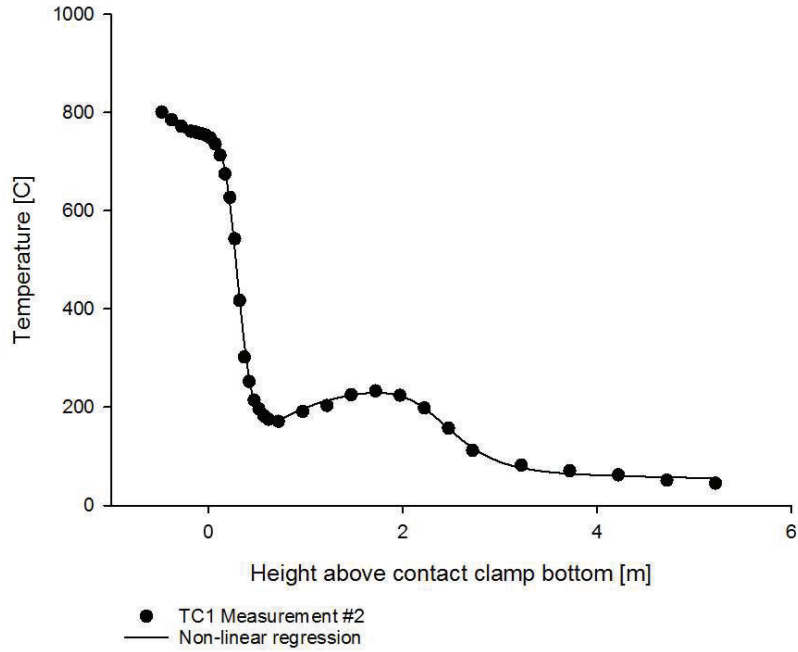

Figure 3-23: The temperature measurement data plotted in Sigmaplot™, with the fitted curve.

Table 3-3: Results from Microsoft Excel Solver for positions of isotherms with the standard deviation as uncertainty.* only one result, thus no standard deviation.

Isotherm [° C]	Positions above contact clamp [m]				
	TC1	TC2	TC3	TC8	TC7
700	-1.30 ± 0.05	-1.26 ± 0.09	-1.22 ± 0.08	-1.00 ± 0.10	-1.12 ± 0.07
500	-1.19 ± 0.05	-1.13 ± 0.07	-1.08 ± 0.06	-0.91 ± 0.07	-1.06 ± 0.07
400	-1.11 ± 0.05	-1.07 ± 0.06	-1.01 ± 0.05	-0.86 ± 0.07	-1.02 ± 0.07
200	-1.00 ± 0.06	-0.84 ± 0.07	-0.74 ± 0.06	-0.62 ± 0.07	-0.86 ± 0.07
200	-0.52 ± 0.10	-0.35 ± 0.18	-0.30*		0.08*
200	0.60 ± 0.21	0.39 ± 0.18	0.43*		0.59*
150	1.15 ± 0.12	0.91 ± 0.13	0.65 ± 0.17	-0.26 ± 0.22	0.91 ± 0.27
100	1.74 ± 0.28	1.56 ± 0.22	1.40 ± 0.28	1.33 ± 0.39	1.85 ± 0.0

Figure 3-24 shows the isotherms of the cross section of electrode A, from the periphery position at the zero point of the x-axis to the mantle positon towards the center of the furnace at x = 190. The isotherms are higher on the center side in the lower parts of the electrode column, which means the electrode is hotter on this side. There are three isotherms for 200 °C as the temperature rise and fall again around the contact clamp tip. On the furnace center side of the electrode, there is only one point for the 200 °C isotherm close to the electrode center, as the temperature has not surpassed 200 °C above the contact clamp.

In the area above the contact clamp the isotherms on the periphery side is at a higher position until the 100 °C isotherm which is in approximately the same height for both sides. In the center of the electrode, where no measurements are available, the isotherms are made with dotted lines. These dotted lined are not an accurate depiction of the real isotherms, but a help to compare positions of isotherms.

On the side towards the furnace center temperatures in the lower parts of the contact clamp are higher than on the periphery side. The 500 °C isotherm, which is higher than the baking temperature found by Shoko, et al. [6], is within the contact clamp on the side of the electrode facing the center of the furnace. Thus, the current can be transferred to the electrode carbon as the electrode leaves the contact clamp. On the periphery side, the 500 °C isotherm is below the bottom of the contact clamp for the position closest to the casing and within the casing for the position closest to the center of the electrode. The position of the baking isotherm is crucial in furnaces where the electrode current is over the current carrying capacity of the casing, as the unbaked carbon electrode cannot conduct current. The current carrying capacity of the casing in this case has been calculated to 139 kA, when the steel in the casing has a capacity to carry 2.5 A/mm^2. The current carrying capacity of the casing is thus around the value that the electrodes are working in this furnace.

The variability of the position of isotherms shown in Figure 3-24 is quite large in upper parts of the electrode column, where temperature gradients are small. In areas where temperature gradients are small, it is expected that isotherms will move more during normal operations. The lower isotherms may be effected by the change of liquid paste level as discussed earlier, and some variability in the position of the, e.g. 100 °C, isotherm is expected. In the lower part of the contact clamp, where temperature gradients are high, smaller variability is found.

As the measurements are done with 21 m long thermocouples, the accuracy of the position is a challenge. Looking at the temperature profiles of Figure 3-11 there is some variability, but as can be seen in Figure 3-15, where measurements two different days show the same variation in four different positions, the variability seen is probably caused by real process variations.
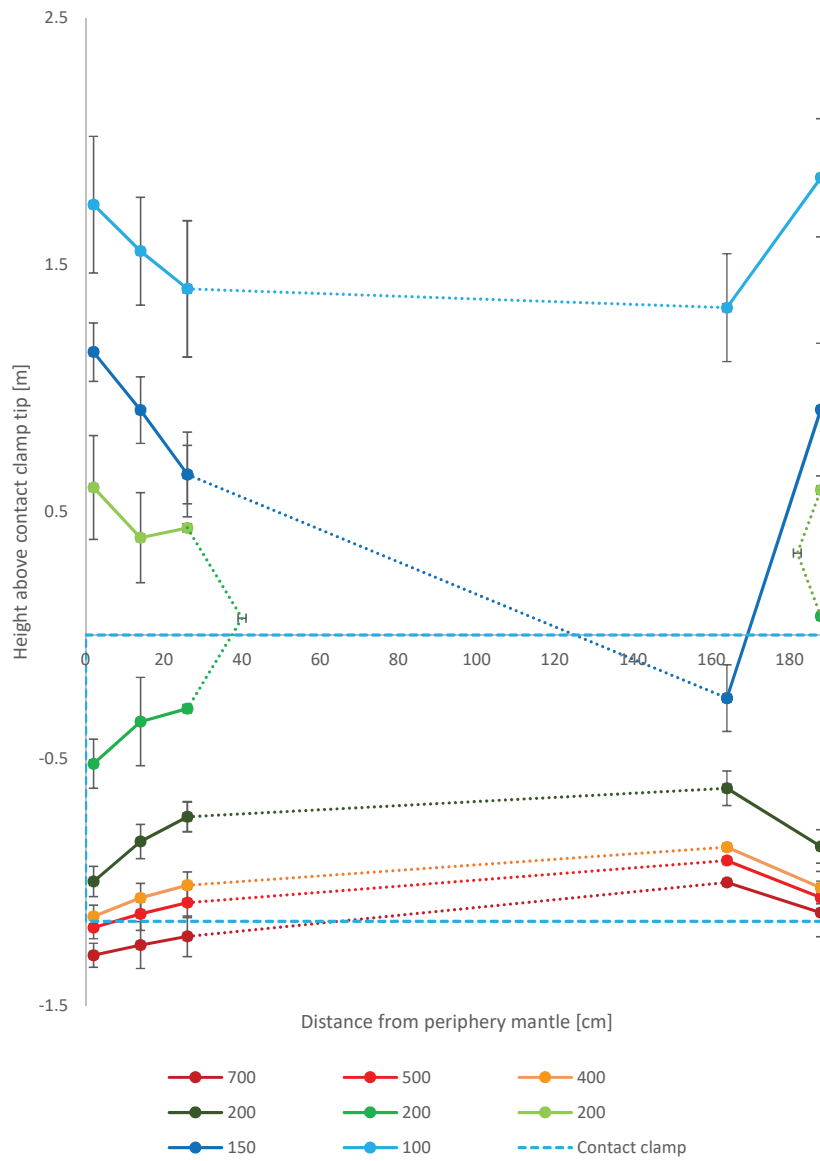
Figure 3-24: Isotherms of electrode A where the x-axis is the diameter of the electrode, where 0 is the mantle in the periphery position. The standard deviation of measurements are used as uncertainty. The blue striped line gives the area of the contact clamp.

The COMSOL model described in section 3.2.4 was developed to model the heat transfer in an axisymmetric case. The results are shown with isotherms and a surface plot in Figure 3-25. Compared to more advanced model, e.g. Larsen, et al. [2] which incorporate slipping and electrical heating by the current, the temperatures in the center of the electrode are too high. The goal of this model was to make a simple model to check how factors, such as the induced heat above the contact clamp and material properties (heat conduction), influence the temperature profiles.
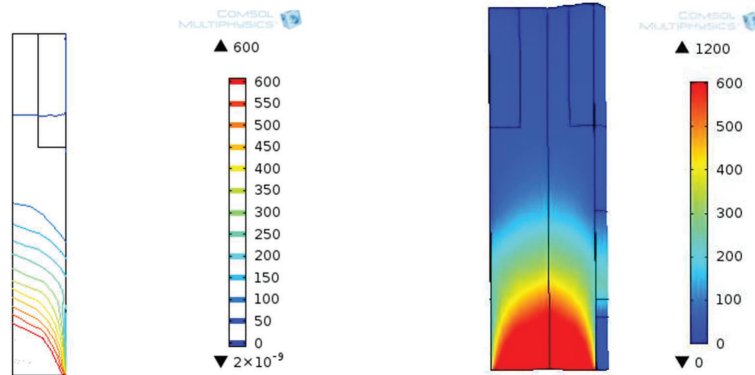
Figure 3-25: Temperatures in the electrode paste calculated by the COMSOL model.

The resulting temperature profiles from COMSOL is shown in Figure 3-26 for the position close to the casing, and in Figure 3-27 for the measurement position closer to the electrode center. Three cases are shown in Figure 3-26, a reference case, a case with lower induced heat and a case with increased heat conductivity in the area of the fins. The modelled temperatures compared to measurements in position #1 and #9. The modelled temperatures are cooler longer than the measured as there is no air heating in the model, and the temperature rise similarly up to a temperature peak caused by the induced heat. The lowest temperatures are reached high in the contact clamp for the model. The model is not able to describe accurately the temperature increase in the lower part of the contact clamp as temperature gradients are lower. The case with increased heat conduction where the steel fins are, were able to increase the temperature gradients but not up to a level of the measured value. When induction above the contact clamp is reduced to 50 %, the peak above the contact clamps is reduced significantly and resembles more measurements in position 9 compared to 1 for the reference case.
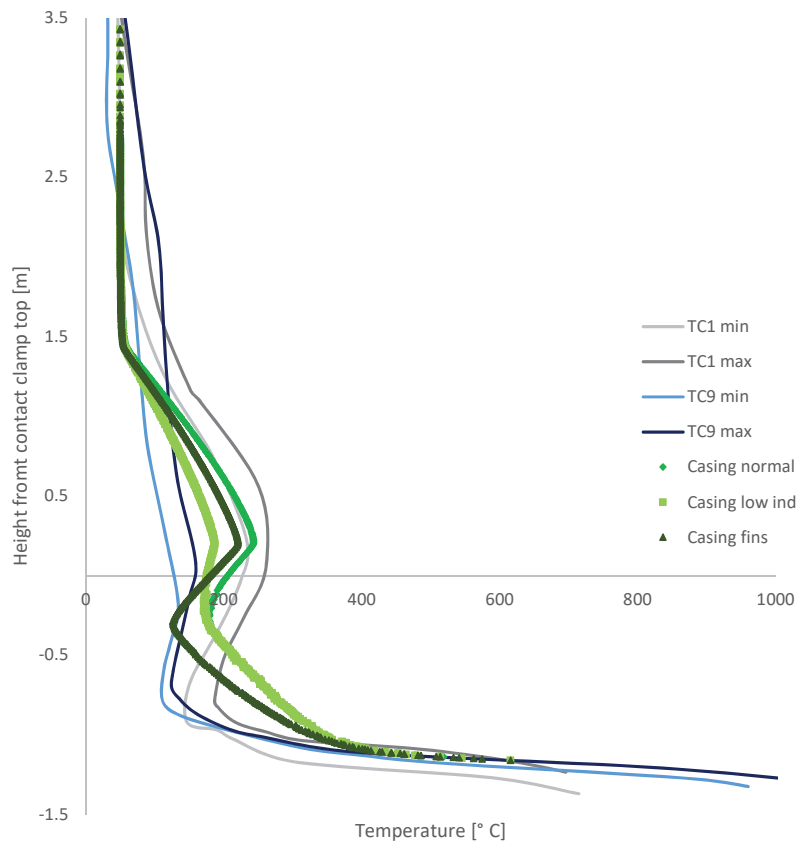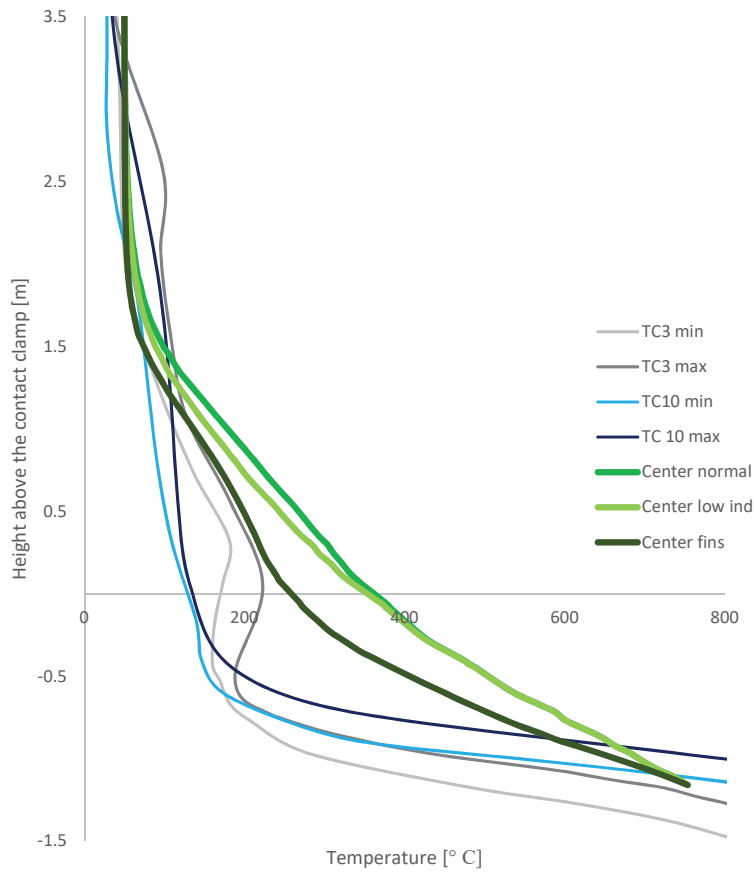
Figure 3-26: The temperature profile given by the COMSOL model is shown to the left and the position of the profile is given in the figure to the right, 2 cm from the casing

In Figure 3-27, the modelled temperatures 26 cm into the electrode are shown with measurements in position 3 and 10. The model is not able to describe the measured temperatures, but the case with higher heat conductivity approached the measured temperatures. Slipping, heat conduction by fins and heating caused by the electric current is not incorporated in the model and is needed to model the interior of a Søderberg electrode well.

Figure 3-27: The temperature profile given by the COMSOL model is shown to the left and the position of the profile is given in the figure to the right, 26 cm from the casing

3.4.2.   TEMPERATURES DURING SHUTDOWN

The slipping increase before a furnace shutdown can be identified in Figure 3-19, when the temperatures drop out of the normal furnace operations band in the lower parts of the contact clamp. Temperatures 600 °C are found 30-40 cm below the contact clamp bottom close to the casing, and the baking zone will thus be moved down as well. In the upper parts of the contact clamp, in Figure 3-20, the temperatures will be high as the temperatures usually decrease in this area under normal operations. As slipping increases, the electrode paste is exposed to the cooling from the contact clamps in a shorter period and will be cooled less. High in the electrode column (1-2.5 m above contact clamp) the temperatures stay within the normal temperature band in high slipping conditions (Figure 3-21 and Figure 3-22). In this area, temperature gradients are usually low and higher slipping will have little effect on the temperature of the paste.

In Figure 3-21 the temperatures have been measured 1 hour into the furnace shutdown, and temperatures are already lower than the normal temperature bands. The effect is higher close to the casing from the middle of the contact clamp and up. As the electrode paste, is either heated or cooled from outside the casing in this area. The temperature peak above the contact clamp is reduced and the paste has been cooled outside of the normal temperature band by the cooling water in the contact clamp. The effect of the cooling in the contact clamp is not severe, as the temperature of the cooling water has been increased to decrease the temperature drop in the electrode paste during furnace shutdown. The temperature rise in the bottom of the contact clamp is much lower than normal as slipping was increased significantly before the furnace shutdown, as discussed in the paragraph above. Only the latent heat within the furnace will now keep temperatures up, and it is not enough to heat the electrode paste below the contact clamps. Closer to the electrode center the temperatures have not dropped as much as close to the casing, as the thermal conductivity of the electrode paste is quite low.

Three hours into the furnace shutdown temperatures have dropped even more, as seen in Figure 3-19. The same effects causes the temperatures to be lower three hours into the furnace shutdown as 1 hour into it.

From 4 to 18 hours into the furnace start-up the temperatures start at a lower than normal in the bottom of the contact clamp, as seen in Figure 3-19. During the start-up temperatures move into the band for normal furnace operations, and end up in the lower parts of the normal furnace operations temperature band. At the top of the contact clamp the temperatures also start up lower than normal in Figure 3-20 and Figure 3-21. Close to the casing the temperatures recovers quicker than closer to the furnace center. In this area the electrode paste is heated by the induced current in the casing, and since the heat comes from outside the temperatures closer to the casing recovers quicker. For the position closer to the electrode center, the position closer to the center of the furnace recovers slower than the periphery position. As the temperature peak above the contact clamp is higher for the periphery position more heat is added in this position and the temperatures will recover faster. This can also be seen when comparing electrode Figure 3-21 (electrode A) and Figure 3-22 (electrode C).

20 hours after furnace start-up, the temperatures close to the casing have almost recovered above the contact clamp. Within the contact clamp temperatures are still lower than normal in the upper parts where the electrode paste is cooled, and temperatures are still lower than normal in the hot parts below the contact clamp. Closer to the center of the electrode temperatures have recovered beneath the contact clamp, but are still lower than normal in the upper parts of the contact clamp and up to 0.5 m above the contact clamp.

3.5. CONCLUSION

The electrode paste will fill the casing at around 80 °C, as there is a temperature increase up to 80 °C in the same height as the liquid paste level. Temperature profiles of Søderberg electrodes in a FeMn furnace have shown that induced currents above the contact clamps may heat electrode paste up to 280 °C. The electrode paste will have low viscosity at these temperatures and segregated paste as seen in Figure 3-1 may happen. Measurements on the electrode with most liquid paste, electrode A, compared to electrode C show higher temperatures in the area above the contact clamps. However, as only two positions are compared, and the effect of induced currents will wary around the circumference of the electrode, it cannot be exclusively concluded that induced currents is the main difference between the two electrodes. The COMSOL computer model show that reducing the heating by the induced current above the contact clamps will reduce temperatures in the electrode paste.

The temperature profiles have shown that the baking isotherm is low in the contact clamp on the periphery of electrode A. Towards the center of the furnace the baking isotherm is within the contact clamp. In situations where the electrode current exceeds the current carrying capacity of the casing, this may lead to soft breakage of the electrode. The current carrying capacity of the casing is close to the actual electrode current and soft breakages have not been a problem at the furnace.

The lowering effect of high slipping before furnace shutdown on the baking isotherm has been shown. During shutdown of the furnace increased temperature of contact clamp cooling water keeps temperatures of the paste stable in the upper parts of the contact clamp. 20 hours after furnace start-up temperatures are almost back to normal furnace operating temperatures.

CHAPTER 4   FLOW AND VISCOSITY MEASUREMENTS

4.1. BACKGROUND AND OBJECTIVE OF MEASUREMENTS

The temperature profiles for heating of electrode paste in an industrial FeMn furnace were found in the previous chapter. As the electrode paste is heated, the viscosity or flow properties of the paste, determines how the electrode paste fills the casing. It is therefore important to establish a method for characterizing the flow properties in the temperature range where the electrode paste flows, 40 – 120° C. This will give knowledge about how the electrode paste flows, and how difference in pastes influence viscosity of the electrode paste.

The basic property determining flow properties is viscosity, and several methods to measure viscosity is given in Section 2.6. Tørklep [86] realizes that a complete rheological description of highly non-ideal electrode paste is unattainable. The parallel plate method for characterizing electrode paste is chosen as the load characteristics are similar with the industrial situation and that large measuring gaps can easily be employed. The reproducibility of measurements depending on gap size divided by particle diameter is shown in Figure 4-1. A large gap between the plates is needed as the electrode paste contains anthracite particles sieved below 12-15 mm. Tørklep [86] states that the gap size needed to maximize reproducibility is 50-100 times particle diameter, but he also states that a rule of thumb allows for gap sizes being more than 3 times the particle diameter.
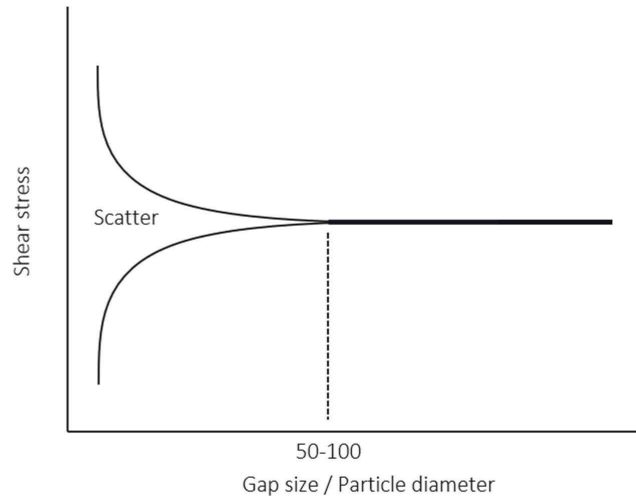

Figure 4-1: As gap size divided by particle diameter increases there is less scatter in measured shear stress, and thus increasing reproducibility, redrawn from Tørklep [86].

Figure 4-2 describes the results expected when testing one electrode paste with repeated measurements of shear stress vs. shear rate. The same electrode paste will give variation in measured data as particle interactions in the electrode paste will vary for each test.
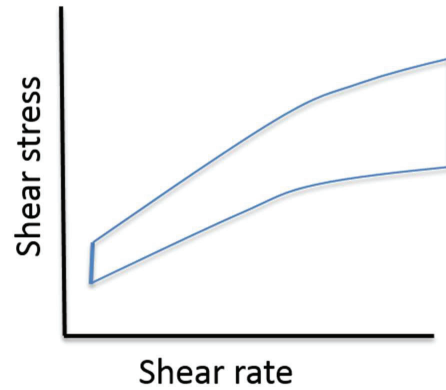
Figure 4-2: Flow bands for suspensions where parallel results will vary because of the solids in the electrode paste. Reproduced from Tørklep [86].

The height/radius ratio used in the experimental setup is similar to the ratio for electrode paste cylinders used in the smelters. To fill the electrode casing the paste cylinders need to double the radii, and hence the height will be reduced by a factor of four. Industrially the electrode paste is compressed by the weight of the electrode paste cylinders added from the top. Cylinders are usually added once a day, 1-3 at a time, and the electrode paste will fill the casing because of the increased pressure. The adding of cylinders can be seen as isothermal compression, in the same way as in the parallel plate viscometer with constant temperature (Larsen, et al. [104]). However, the electrode paste will also flow as it is heated in the electrode column and the viscosity decreases due to the higher temperature.

To gain information about how the electrode paste behaves during heating the parallel plate setup has been used in an oven where temperature can increase similar to an industrial electrode. The electrode paste was preheated for 2h at 30 °C before measurements started, and temperature was set to increase linearly up to the final temperature. In these experiments, the electrode paste is compressed for 24 – 48 hours, similar to the times and shear rates experienced by cylinders in industrial electrodes.

4.2. EXPERIMENTAL

In this section a description of how the electrode paste samples are made and characterized. The focus will be on a description of the equipment and the measurement of flow properties of electrode paste.

4.2.1.   RAW MATERIALS

Electrically calcined anthracite has been used as the filler material for all experiments. The size distribution of the anthracite filler material is characterized by sieve analysis. Each fraction is sieved separately, and the fines fraction is usually only described by retention on one or two (63 or 75 µm) sieves. The size distribution of anthracites used is given in Table 4-1.

Table 4-1: Particle size distribution for the anthracite used in experiments

Particle size fraction	Coarse [%]	Medium [%]	Fines [%]	*Total [%]*
+12.5 *mm*	<5	0	0	< 5
+4 *mm*	>90	< 5	0	>35
+1 *mm*	>98	40-60	< 0.5	40-60
+ 123 *µm*	>98	> 80	< 30	> 70
+63µm	>98	> 80	40-60	> 70

The degree of heat treatment of anthracite is tested with an electrical resistivity measurement of a 0.25-1.0 mm size distribution crushed coarse anthracite, similar to ISO 10143:2014 [106]. For a given anthracite, calcination to a higher temperature will give a lower electrical resistivity in the heat-treated material. Typical values for some properties of the calcined anthracite used in this work is shown in Table 4-2.

Table 4-2: Typical coarse anthracite properties

	Coarse anthracite
Electrical resistivity [µΩm] [106]	559
Absolute density (He) [kg/ m^3]	1849
Density (water) [kg/ m^3]	1665
Vibrated bulk density (VBD) [kg/m^3]	1014

The coal tar pitch is characterized by coking value, distillation, softening point, ash, solubility in quinoline and toluene and density. All pitches used in this work have softening points at about 65 °C, and came from the same producer. The viscosity of the coal tar pitch has been measured at temperatures above the softening point with a HAAKE RheoStress™ Rheometer. Properties of the coal-tar pitch used in this work is shown in Table 4-3.

Table 4-3: Coal tar pitch properties

	Coal tar pitch
Softening point (Mettler) [°C]	66.7
Coking value [%]	41.7
Ash [%]	0.09
TI [%]	18.4
QI [%]	5.52
Density [kg/m^3]	1268
Viscosity [mPa s]	
100 °C	2941
Distillation	
20-270 °C	0
20-300 °C	0
20-360 °C	*3.6*

4.2.2.   PROCEDURE

Electrode pastes have been either sampled from the production line at Elkem Carbon Fiskaa or produced from the same raw materials in the laboratory. A flow chart of electrode paste production is given in the introduction, Figure 1-2, and the electrode paste has been extracted when the electrode paste is casted, in the box "Forming" in the figure. The hot electrode paste (~ 150 °C) is cast into a steel cylinder with the desired radii and other samples such as plasticity can be taken. The samples are air cooled until they are removed from the steel cylinder. The desired height of the sample is achieved by cutting the electrode paste cylinders.

When electrode paste samples are made in the laboratory the anthracite filler and coal tar pitch is preheated to 180° C. The anthracite filler is weighed in the desired amount before mixing, while coal tar pitch is weighed as it is added. A high intensity Eirich mixer, seen in Figure 4-3, was used to mix the laboratory samples. A heat torch, seen on the left in Figure 4-3, can be used to heat the bowl with the electrode paste to maintain the mixing temperature. The dry material is put in the mixer first, and premixed for 1 minute. Then the coal tar pitch is added and mixed with the anthracite for 5 minutes. After the desired mixing times, the electrode paste is casted in the steel cylinders used for the sampling of industrial electrode paste. Samples for plasticity may be gathered, as the electrode paste is casted.

Figure 4-3: The Eirich high intensity mixer used to prepare electrode paste.

4.2.3.   ELECTRODE PASTE CHARACTERIZATION

After the electrode paste has solidified, the density of samples are measured. The density is given by Archimedes' principle, and is calculated by weighing the samples dry ($m_{el.paste}$) and the apparent immersed weight (m_{aiw}) .

$$\rho_{el.paste} = \frac{m_{el.paste}}{\left(m_{el.paste} - m_{aiw}\right)} \qquad \textit{(4-1)}$$

Commercial electrode paste is often characterized by a so-called plasticity number. The plasticity measurement is described in Chapter 2.2, with a heat treatment at 300 °C for 45 minutes, and is defined by the equation:

$$Plasticity \ [\%] = \left(\frac{(radius \ after \ heat \ treatment - \ initial \ radius \ )}{initial \ radius}\right) \cdot 100 \ \% \qquad \textit{(4-2)}$$

4.2.4.   FLOW MEASUREMENTS

Measurements were done with a parallel plate viscometer as shown in Figure 2-19 and with constant force as described by Tørklep [86]. The apparatus is shown in Figure 4-4 with an electrode paste sample inside the furnace. The force on the top parallel plate is given by the weights on top of the plate and the height of the sample is measured by a linear variable differential transformer (LVDT) fixed to the plate on top of the furnace.

Figure 4-4: The furnace for flow measurements with sample inside.

An example of the results is shown in Figure 4-5 where the height of the sample divided by initial sample height is shown as a function of both temperature (black) and time (red). The mayor part of the electrode paste compression is done between 50 and 80 °C, and at 80 °C the sample is at about 40 % of its original height. At this compression in an industrial electrode, the paste will have filled the cross section of the electrode.

As temperature rises linearly with time the two lines in Figure 4-5 are almost identical, with a bit more variation in the temperature results as temperature does not rise perfectly linearly with time. The heating rate used in the experiments resembles the heating rate in an industrial furnace, where Larsen, et al. [104] calculated max shear rates in industrial size electrodes by using equation (2-48) to be $5 \cdot 10^{-5} - 2 \cdot 10^{-4} s^{-1}$. Shear rates in the flow measurements in Figure 4-5 range from $3 \cdot 10^{-6} - 1.1 \cdot 10^{-4} s^{-1}$, as seen in Figure 4-6. The slower shear rates are at low temperatures and it is expected that electrode paste cylinders in industrial furnaces will experience similar shear rates as the flow measurements gives. Higher shear rates are expected during addition of electrode paste to the top of the electrode column, as the pressure on the heated paste is increased in a relative short time (e.g. addition of two cylinders in a 1.8 m electrode is ~2 tons in 10 minutes).
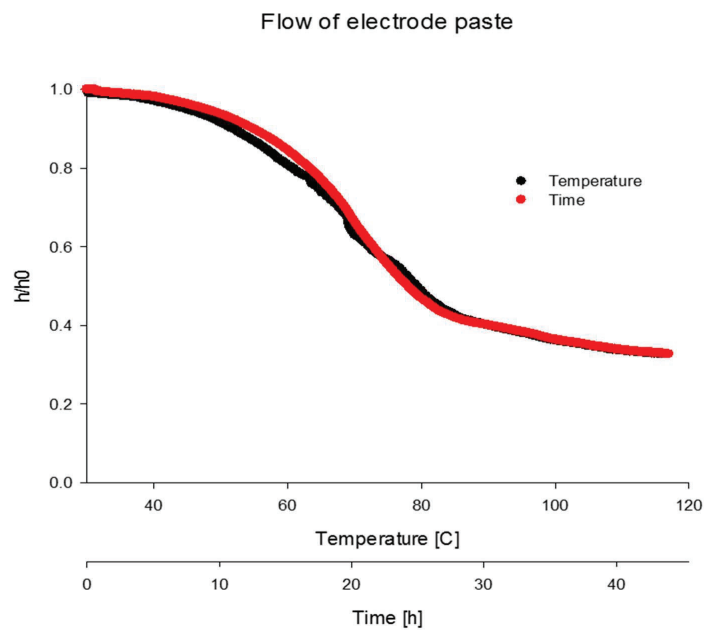
Figure 4-5: The height of the sample divided by initial height with both temperature and time on the x-axis is shown for a sample in the parallel plate setup used in this paper (Data from experiment with LP High).
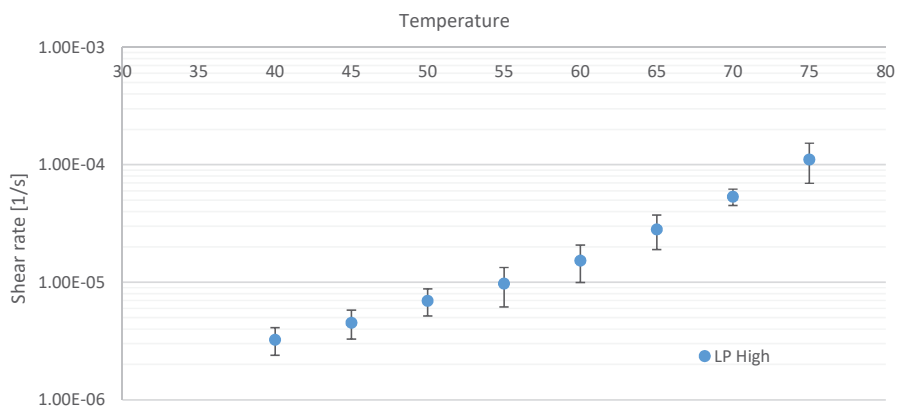

Figure 4-6: Shear rates from 40 – 75° C for electrode pate with large particles (LP High).

4.2.5.   EXPERIMENTAL SERIES

To study the effect of experimental parameters on the flow properties of electrode paste, series of experiments were conducted. In the following section, experimental variables for each series is given.

4.2.6.   SAMPLE HEIGHT AND HEATING RATE

In Table 4-4 mixing and sample characteristics are given for the samples used to ascertain the effect of sample height on flow measurements of electrode paste. Two electrode pastes were tested, one with larger coarse particles (LP) and one with smaller coarse particles (SP). The heights of the samples varied between around 16 cm and 8 cm.

Table 4-4 Electrode paste characteristics for paste used in flow measurements to test the effect of height of samples on flow characteristics. Where size fractions is the number of fractions used, that is a 3-fraction paste consist of a coarse- medium and fines-fraction.

Sample height	Heights [m]	Size fractions	Pitch content [%]	Plasticity
LP High	0.16	2	23.9	31.3
LP Low	0.08	2		
SP High	0.16	3	24.8	26.6
SP Low	0.08	3		

The paste with larger coarse particles was also used to check then influence of heating rate on flow properties of electrode paste. The samples and the different heating rates are given in Table 4-5.

Table 4-5: Samples used in heating rate experiments with a high and low heating rate and high and low samples.

Heating rate series	Heating rate [°C/h]	Height [cm]
LP High 2 °C/h	2	16
LP High 4 °C/h	4	16
LP Low 2 °C/h	2	8
LP Low 4 °C/h	4	8

The pressure and temperature for isothermal measurements on electrode paste with varying force on sample are shown in Table 4-6.

Table 4-6: The electrode paste samples used in isothermal measurements.

Sample	Height [m]	Radius [m]	Force on sample [N]	Pressure on sample [bar]	Temperature [° C]
Iso-SP High P 1	0.14	0.15	657	0.37	70
Iso-SP High P 2	0.14	0.15	657	0.37	70
Iso-SP Low P 1	0.14	0.15	477	0.27	70

4.2.7.   AMOUNT OF COARSE PARTICLES

In one experimental series the fines/pitch ratio was kept at two constant levels while the content of coarse particles was increased from 40 to 70 %, see Table 4-7. The cylindrical flow measurement samples made had a height of 16 cm and a radius of 8.5 cm. Only flow measurement samples were cast, and samples had the same height and radius, 16 cm high and with a radius of 8.5 cm.

Table 4-7. Mixtures in the coarse fraction experiments, where the fines/pitch ratio had a high level and a low level for each content of coarse fraction.

Coarse series	Coarse content [%]	Pitch content [%]	Pitch/fines ratio
CF-40-H	40	28.7	0.670
CF-40-L	40	27.0	0.617
CF-50-H	50	25.1	0.669
CF-50-L	50	22.9	0.593
CF-60-H	60	21.2	0.673
CF-60-L	60	19.2	0.594
CF-70-H	70	18.2	0.743
CF-70-L	70	16.2	0.650

4.2.8.   FINES SERIES

Electrode pastes containing only fines and coal tar pitch binder was made to see how flow properties of the binder/fines phase change with increasing fines content. Fines content ranging from 30 % to 73 % were tested in two different sample sizes, as shown in Table 4-8. The samples of mix FF-30-2 were brittle, and broke when the cast was removed. Samples were made for both measurements of flow during increasing temperature and flow at constant temperature, see Table 4-9.

Table 4-8: Dimensions of samples for each batch mixed and used in flow measurements of electrode paste containing fines and pitch in different ratios.

Fines series	Fines content [%]	Radius [cm]	Height [cm]
FF-30-1	30.0	7.5	7
FF-30-2	30.0	-	-
FF-60-1	60.0	8.5	16
FF-60-2	60.0	7.5	7
FF-67-1	67.0	8.5	16
FF-67-2	66.9	7.5	7
FF-73-1	72.9	8.5	16

Table 4-9: Measurements done within the fines series

Fines series	Measurement	Temperature [°C]
FF-30-1	Isothermal	40
FF-60-11	Flow measurement	30-120
FF-60-21	Isothermal	40
FF-60-22	Isothermal	50
FF-60-23	Isothermal	40
FF-67-11	Flow measurement	30-120
FF-67-12	Isothermal	50
FF-67-21	Isothermal	40
FF-67-22	Isothermal	50
FF-73-1	Flow measurement	30-120

4.3. RESULTS

4.3.1.   VISCOSITY MEASUREMENTS ON BINDER

The viscosity of the binder, and a mixture of binder and 30 % fines is given in Figure 4-7, where viscosities from 70-120 °C are shown as a function of $\frac{1}{T}$. Measurements done with concentric cylinders in a HAAKE RheoStress™ Rheometer. Addition of fines clearly increases the viscosity of the mixture in the temperature region examined. At the lower end of the temperature region, the rheometer is not able to make measurements at low rotating speeds (Figure A - 3 and Figure A - 4). The viscosity of the two curves follow the exponential equations below when plotted against 1/T:

$$Pitch: \quad y = 4 \times 10^{-19} e^{16246x}$$

$$Pitch \ and \ 30\% \ fines: \quad y = 2 \times 10^{-19} e^{17016x}$$
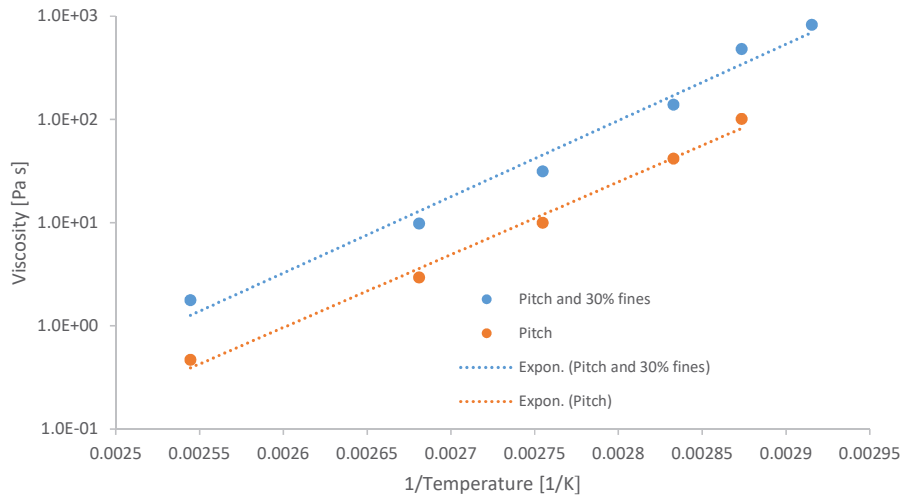
Figure 4-7: Viscosity of binder and a binder/fines mixture at temperatures from 70-120 °C plotted as viscosity vs the inverse temperature. The softening point of the binder is 65° C.

The viscosity at two temperatures is shown in Figure 4-8 as a function of shear rate. As the measurements are done by cycling up and down in shear rate, the pure pitch measurements are stable. The pure pitch behave Newtonian in the shear rates measured at both 100° and 120° C within the shear rate region measured (1-100 s^{-1}) as viscosity is constant for increasing shear rates. For the fines and pitch mixture there is a small increase in viscosity as shear rate decreases, but the difference is negligible at 120° C and small at 100° C. The measurements are more stable as shear rate is decreased at the end of the measurement cycle, compared to the increasing shear rate to begin with.
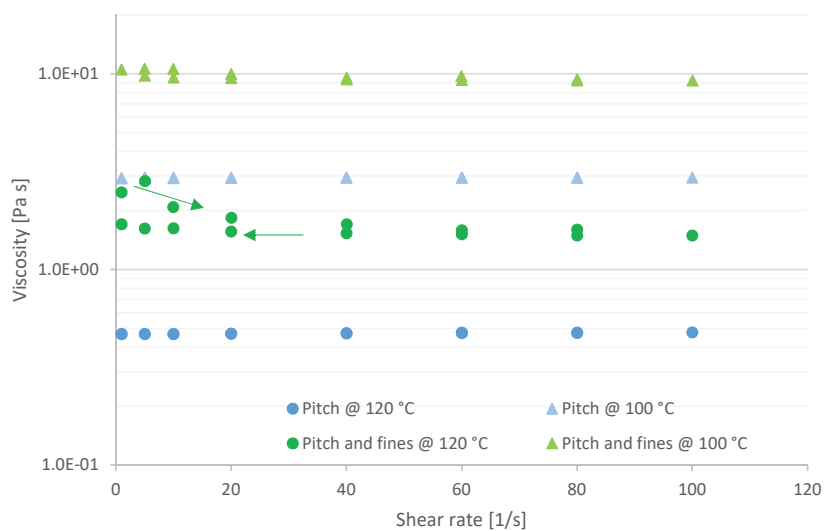
Figure 4-8: The viscosity of pitch and pitch and fines with increasing shear rates in a concentric cylinder rheometer. Green arrows show the way the measurements were cycling, with increased viscosity when shear rates are increasing.

4.3.2.   FLOW MEASUREMENTS

The apparent viscosity of the electrode paste was calculated by rearranging equation (2-43), solving for the apparent viscosity giving equation (4-3). The plate speed $\dot{h}$ is substituted with change in time (Δt) and height (Δh) between two measuring points when calculating the apparent viscosity.

$$\eta = \frac{2\pi F h^5}{3V^2 \frac{\Delta h}{\Delta t}} \frac{h_0}{\left(2 - \frac{h}{h_0} + \frac{4\pi h^3}{3V}\right) h} \qquad (4\text{-}3)$$

Apparent viscosities calculated for temperatures between 40 and 75 °C are presented in Figure 4-9 as a function of 1/T. Apparent viscosity of the electrode paste decreases exponentially, and an Arrhenius' expression can be fitted to the data in this temperature region. The temperature region used is 40 up to 75 °C, as the flow of the electrode paste is restricted by the measurement equipment above this temperature (see Figure 4-5). Uncertainty in the measurements is given as one standard deviation in Figure 4-9, which is up to 40 % of the given apparent viscosity. As shown in Figure 4-2 there will be a certain degree of variability when measuring apparent viscosity of granular materials.
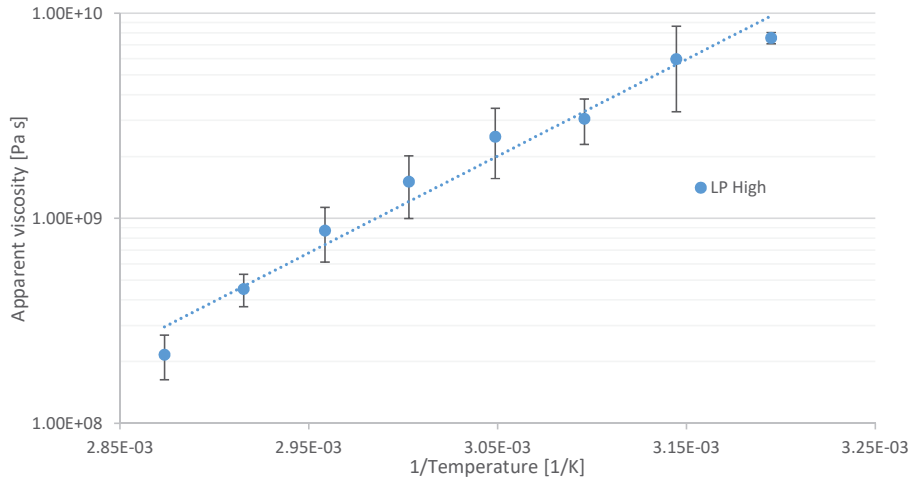
Figure 4-9: Apparent viscosity of electrode paste LP High from 40-75 °C, one standard deviation is used as uncertainty.

4.3.3.   HEATING RATE

The relative height of the electrode paste cylinders are plotted against temperature for experiments at normal (2 °C/h) and high (4 °C/h) heating rate in Figure 4-10. There is no difference between samples at low and high heating rate, even with a doubling of the heating rate when the relative height is plotted against temperature. One sample (LP High 2) is higher than the four other samples from 50 – 70 °C, which probably is due to variation in flow properties of suspension of granular material, e.g. Figure 4-2 or discussion in previous paragraph.

The heating rate has thus a small impact on how the electrode paste flows with respect to temperature, and the temperature gradients in the samples will be quite similar. As a difference in temperature gradient, between the two cases, would give lower temperature (and higher viscosity) in the middle of the samples for higher heating rates. Lower temperature in the middle of the sample would thus lead to slower electrode paste flow.
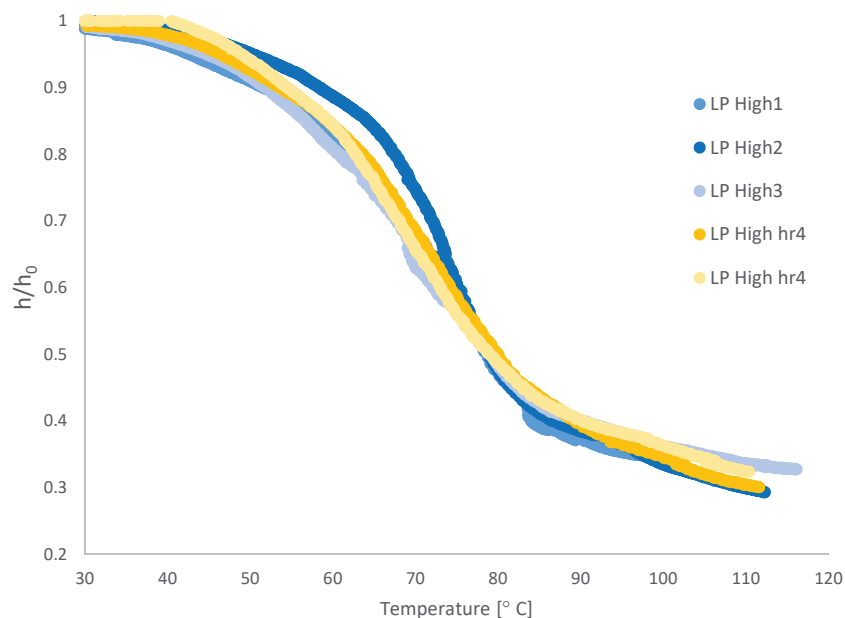
Figure 4-10: The influence of heating rate on the relative height of sample. Samples in blue have heating rate of 2 °C/h and samples in yellow a heating rate of 4 °C/h.

Plotted against time, as shown in Figure 4-11, the high heating rate (yellow) starts with a compression rate similar to the normal heating rate (blue). Although after 5h, at 40 °C, the high heating rate samples increase the compression rate. The higher heating rate will give a faster compression, thus increased shear rate and decreased viscosity.
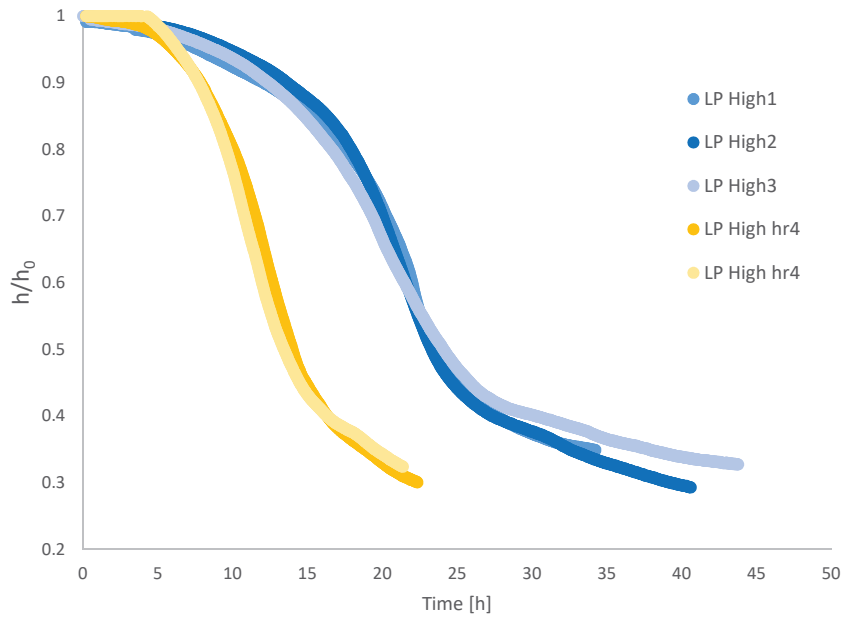
Figure 4-11: The influence of heating rate on the relative height of sample. Samples in blue have heating rate of 2 °C/h and samples in yellow a heating rate of 4 °C/h

The shear rates of the two heating rates are shown in Figure 4-12. At the start of the experiment shear rates of the two heating rates are similar as there is very little movement. Similarly, at the end of measurements shear rates are equal, as movement is restricted by the experimental set-up and the movement is slowed.
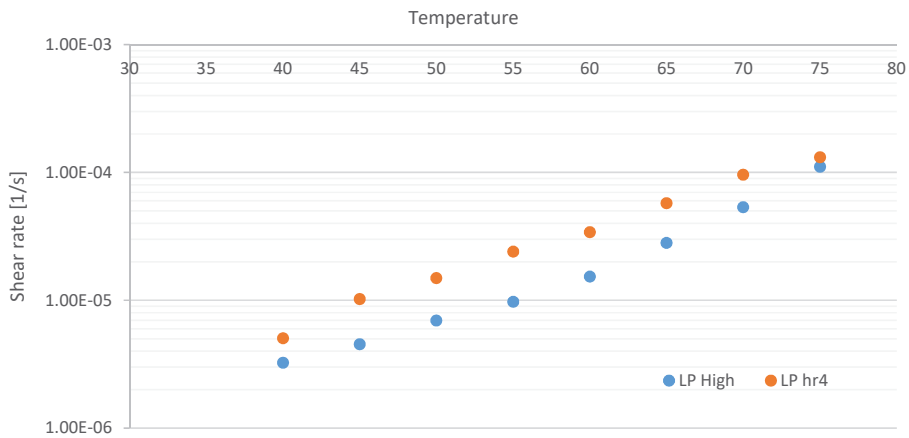

Figure 4-12: Shear rates of normal (2° C/h) and high (4° C/h) heating rates.

The calculated apparent viscosities for the two cases are differing with a factor of around two as shown in Figure 4-13. The viscosity of a Newtonian liquid is a material property and has a given value at a given temperature. Pastes, which are often non-Newtonian, need measurement conditions to be the same to measure equal apparent viscosities, i.e. shear rate and temperature. The apparent viscosity of the two curves follow the exponential equations below:

$$LP\ High: \quad y = 8 \times 10^{-6} e^{10869x}$$
$$LP\ hr4 \quad y = 8 \times 10^{-4} e^{9085x}$$
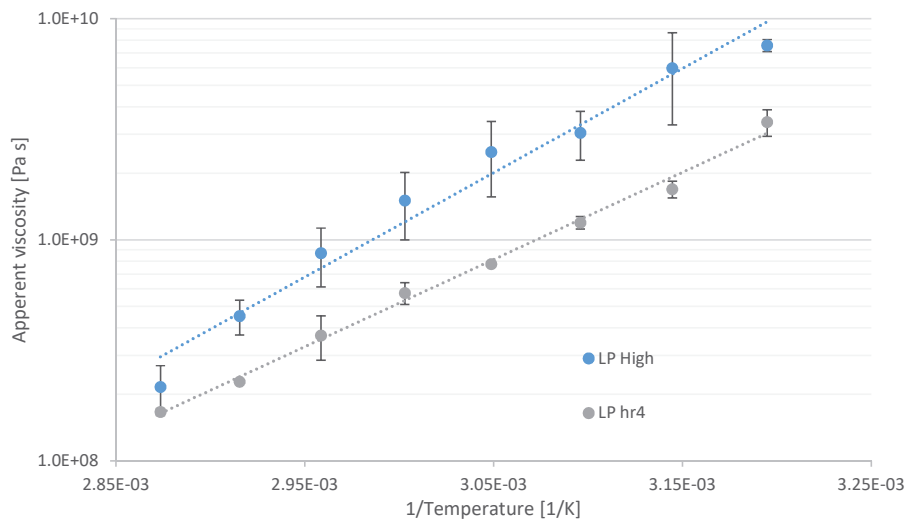
Figure 4-13: Apparent viscosity for normal and high heating rate samples, with uncertainty one standard deviation.

4.3.4.   HEIGHT OF SAMPLE

In Figure 4-14, the height of the sample divided by initial height of sample for samples of height 160 and 80 mm. The high and low samples follow the same curve up to about 70 °C when the lower samples are compressed to 70 % of their initial height. As temperature rises the decrease in height of the samples is slowed, and almost reach a constant height at temperatures above 110 °C.
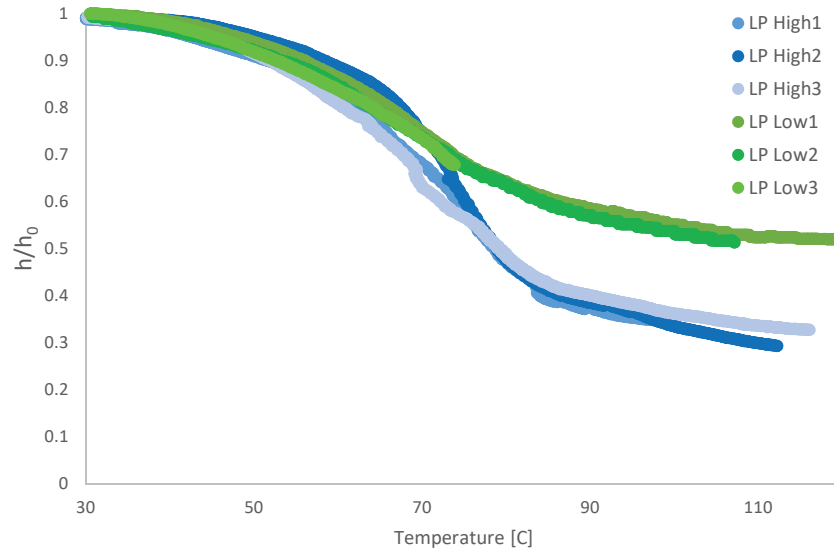
Figure 4-14: Height divided by initial height for high (blue) and low (green) 2-fraction samples of electrode paste.

In Figure 4-15, the same data is shown as a function of sample height, where the high samples are about 16 cm and the low samples have a starting height of about 8 cm. The sample height at the end of the experiment is quite similar for the high and low samples, as the low samples approach 4 cm and the high samples approach 5 cm height. At a height of 7 cm the plate speed of the high samples slows significantly down, whereas for the low sample the plate speed slow down at a height of 6 cm.
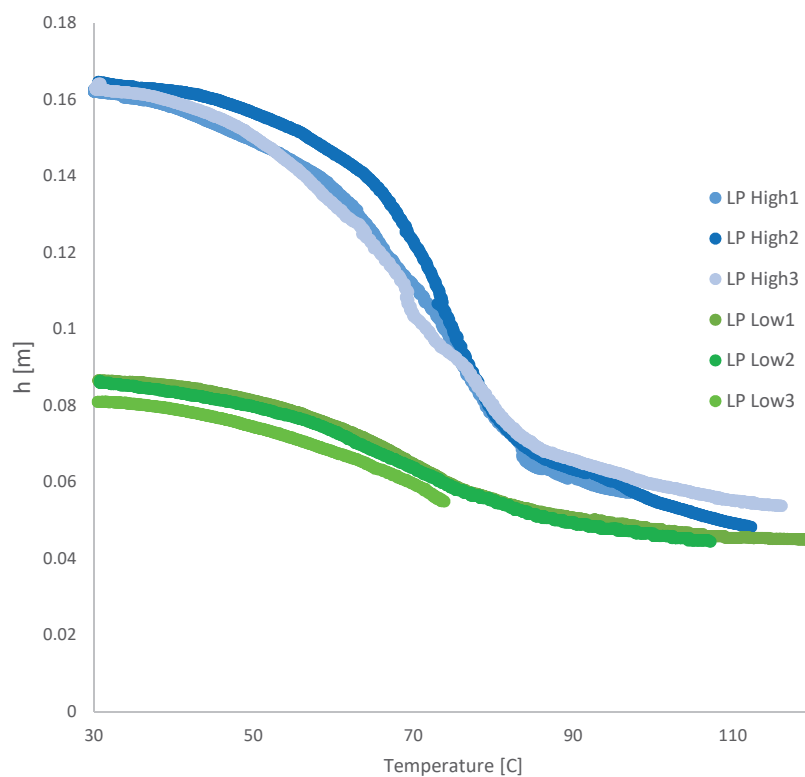
Figure 4-15: The height of high and low samples as a function of temperature for a 2-fraction sample.

In Figure 4-16 and Figure 4-17 the relative height and height of high and low electrode paste samples is given as temperature increases for a 3-fraction electrode paste. The relative heights of the low samples are quite similar to the high samples up to about 70 % of the initial height, at a temperature of 70 °C, where the low samples are compressed less than the high samples. The low samples are compressed to around 40 % of initial height at 120 °C, while the high samples are at 30 % of initial height at the same temperature. In Figure 4-17 the height of the same samples is given, where the final heights of high samples are at 4.5 cm at 120 °C, whereas for the low samples the height is 3 cm.
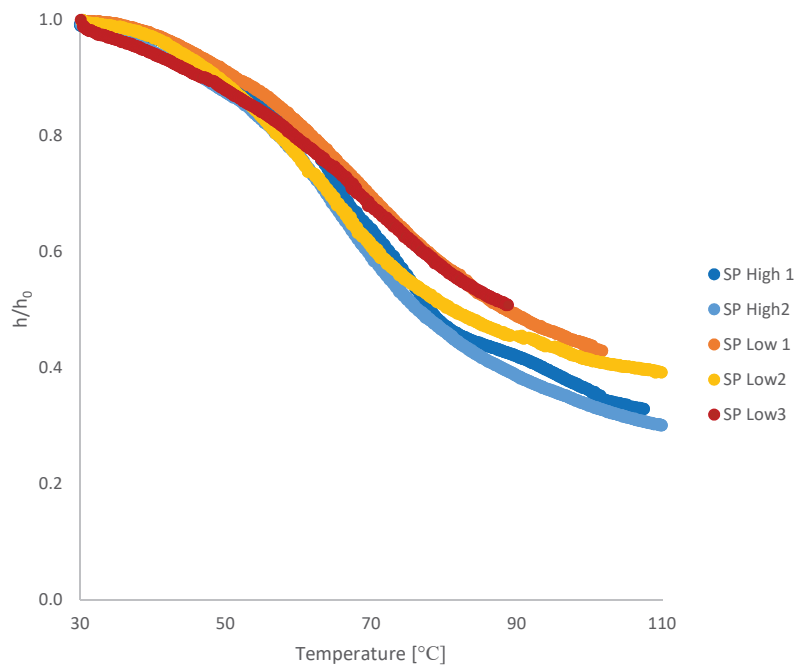
Figure 4-16: Height of samples divided by initial height for high and low 3-fraction electrode paste samples.
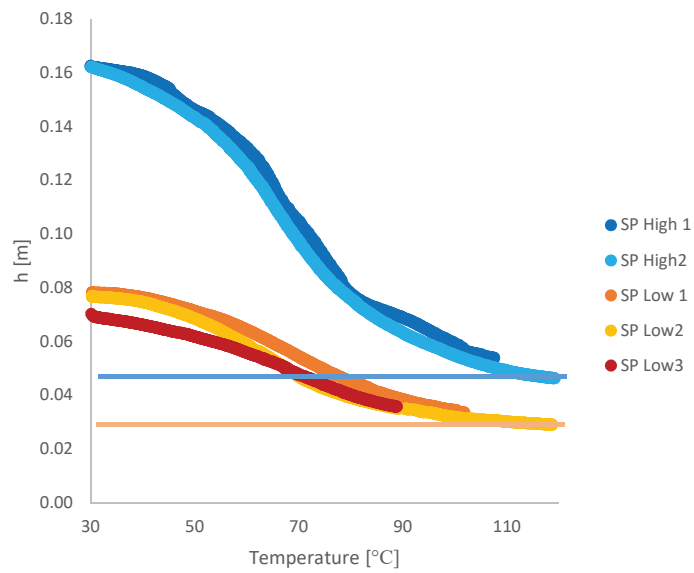
Figure 4-17: The height of high and low samples as a function of temperature for 3-fraction samples.

Apparent viscosities calculated at temperatures of 35-60° C are presented in Figure 4-18. The low samples have lower apparent viscosity than the high samples up to 70° C. At 70° C, the measured apparent viscosity of the low samples will be influenced by the size of the largest particles, and therefore decrease less than the high electrode paste samples. The apparent viscosity of the two curves follow the exponential equations below:

$$LP\ High: \quad y = 8 \times 10^{-6} e^{10869x}$$
$$LP\ Low \quad y = 0.1521 e^{7501x}$$
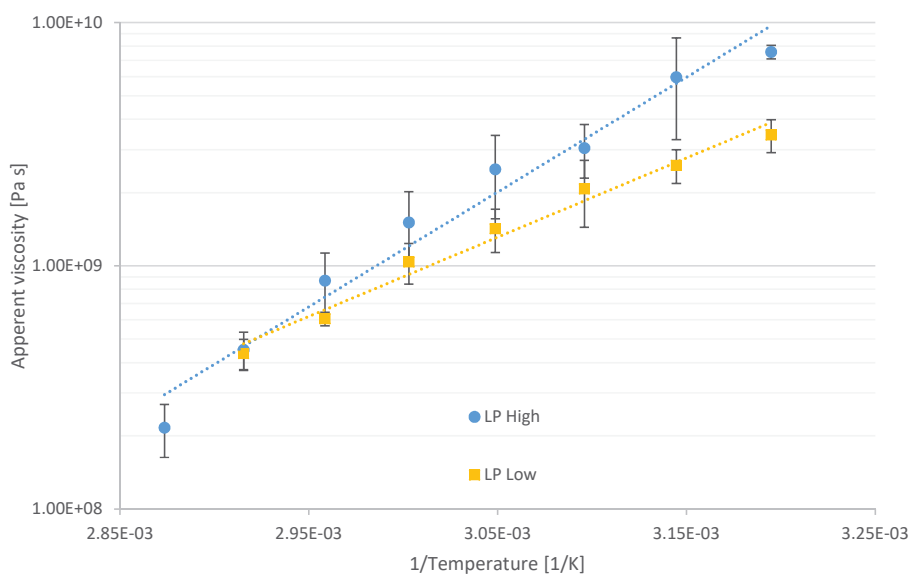
Figure 4-18: Calculated apparent viscosities at temperatures ranging from 35-75° C fir high and low electrode paste samples.

4.3.5.   COARSE PARTICLE SIZE

The influence of the largest particles on flow measurements are assessed by using a more coarse anthracite. The difference in particle size is given by the D90 of the coarse particle size distribution, and is given in Table 4-10. Where D90 signifies that 90% of the particles are smaller than the given size.

Table 4-10: D90 of the two mixes with different coarse anthracite.

	D90 [mm]
Large particles (LP)	12.3
Small particles (SP)	10.6

Flow measurements is shown in Figure 4-19 for high paste samples with large- (LP) and small (SP) particles. SP High 1 has a flow profile similar to LP High 1 and 3, whereas SP High 2 flows earlier and LP High 2 later than the other does. Thus, there is a tendency that the SP paste flows faster than the LP pastes up to about 70° C. Above 70° C there is a small difference between the pastes. The higher pitch content of the SP paste (Table 4-4) may be the reason that the SP pastes flows faster than the LP paste. The higher plasticity of the LP paste does not seem to make the paste flow faster at low temperatures (30-70° C), i.e. below and around the softening point of the pitch.
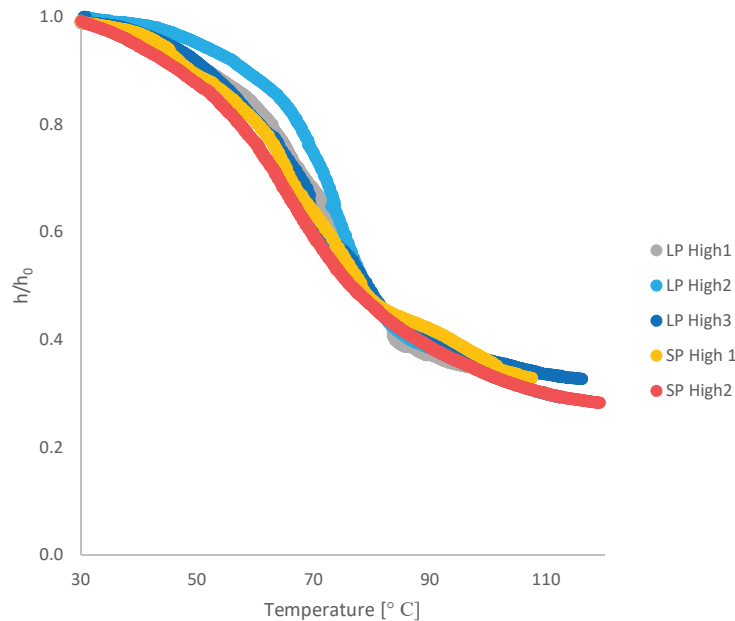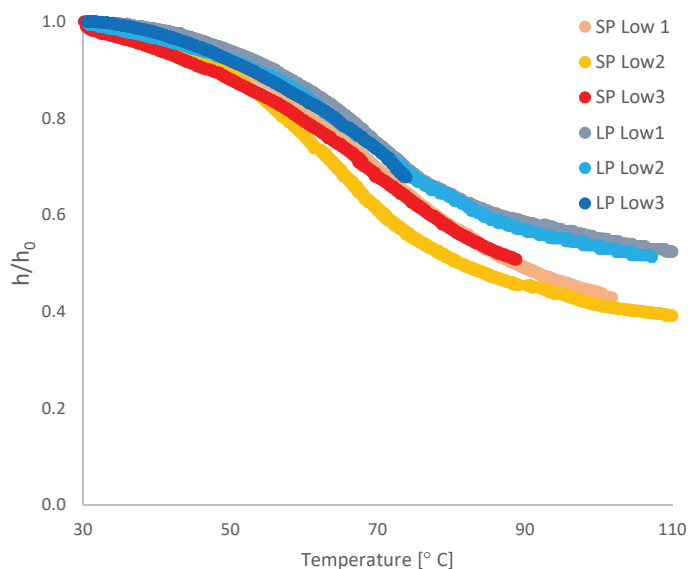

Figure 4-19: Relative height of high samples of paste with large particles (LP) and smaller particles (SP) with similar plasticity. The softening point of the binder is 65 °C for all experiments.

The relative height of low electrode paste samples with large and small particles during flow measurements is shown in Figure 4-20. For the lower electrode paste samples, there is a distinct difference between the two, as the paste with larger particles is not compressed as low as the paste with smaller particles. The flow curves are similar up to h/h_0 0.7, where the large particle paste starts to slow down and the compression flatten at about 50 % compression. As the low height samples with larger particles does not compress as low as the smaller particle paste, the size of the coarse particles seems to influence compression height.

Figure 4-20: Relative height of low samples of paste with large particles (LP) and smaller particles (SP) with similar plasticity.

To asses at what point the low samples start to deviate from a normal flow, the apparent viscosity of the low samples is shown in Figure 4-21 up to 85° C. The small particle paste apparent viscosity flattens at 65° C, compared to 70° C for the larger particles. The height at these temperatures (Breaking point height) is shown in Table 4-11. The breaking point (BP) height divided by D90 should than give a minimum height of sample compared to the largest particle size. The gap size needs to be 5 times the largest particle size (D90 of the coarse material) to have reliable measurements.
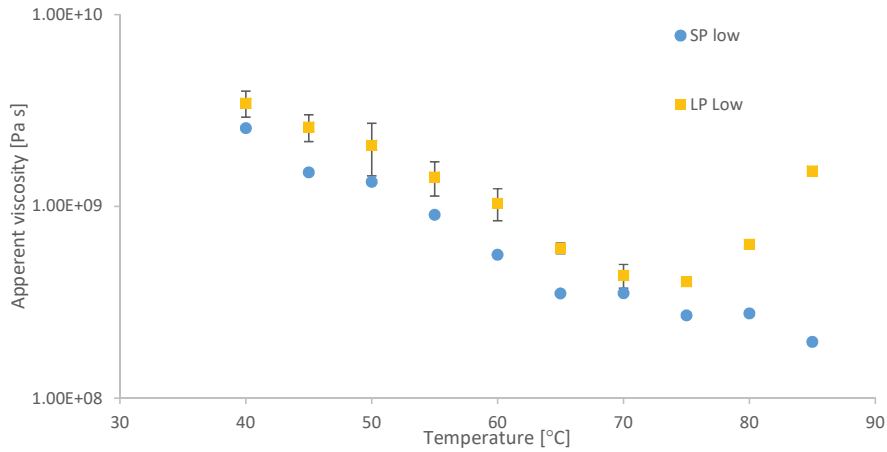
Figure 4-21: The apparent viscosity of SP samples stops decreasing at 65 °C while the LP samples stops decreasing at 70 °C.

Table 4-11: Comparing Height of samples at the point where viscosity measurements starts increase and the particle size D90 give

	LP low	SP low
Temperature [°C]	70	65
Breaking point (BP) height [mm]	62.7	54.8
D90 [mm]	12.3	10.6
BP/D90	5.1	5.2

4.3.6.   ISOTHERMAL MEASUREMENTS ON PASTE

Shear rates of isothermal measurements are higher than average shear rates in industrial electrodes and flow measurements with increasing temperature. In industrial electrodes, new paste is added regularly, and as new paste is added, the pressure on the electrode paste will increase. Thus, isothermal measurements can show what happens to electrode paste as new paste is added.

Isothermal flow of two samples with normal pressure and one sample with reduced pressure is shown in Figure 4-22 at 70° C. The flow curve of the two samples with normal pressure are compressed to the same level, but iso-SP High-P1 is compressed faster than iso-SP High-P 2 in first 4 hours of the measurements. At lower pressure, the electrode paste is compressed slower and to a higher level compared to the higher-pressure samples.
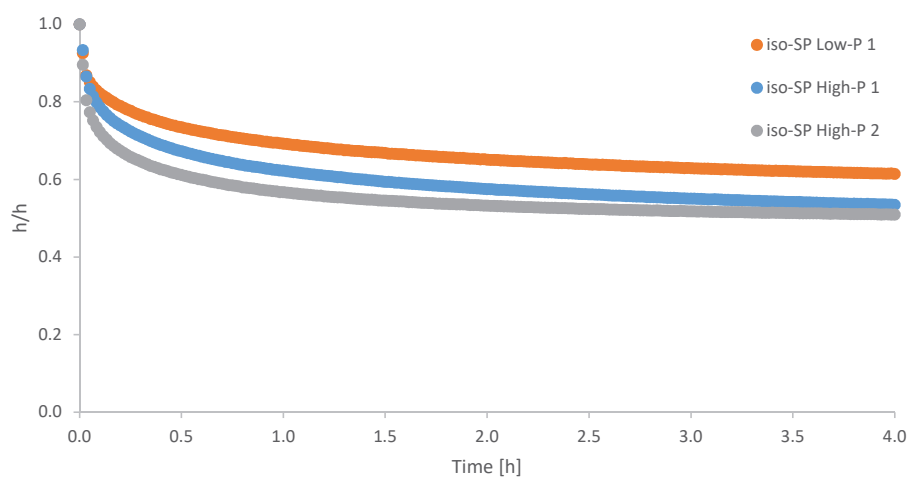
Figure 4-22: Isothermal compression of electrode paste samples at 70° C with high and low force on the samples. Higher pressure on the electrode paste sample increases compression rate and decreases the relative height to which the sample is compressed.

There is little difference in apparent viscosity between the two high pressures samples shown in Figure 4-23 at 70° C. As compression rate decreases the variability of the measurements increase, as discussed previously. Lower pressure on the electrode paste give the same apparent viscosity at the start of the experiments, but after 0.2 h apparent viscosity for sample with lower pressure is slightly lower than the higher-pressure samples. Thus, the apparent viscosity is not dependent on pressure up to the point where the flow starts to slow down.
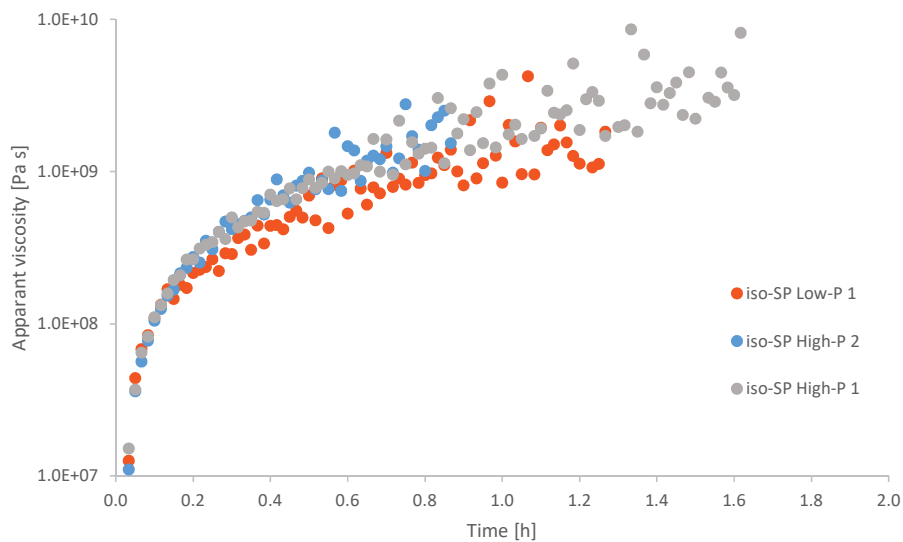
Figure 4-23: Apparent viscosity at 70° C for high and low pressure electrode paste samples.

4.3.7.   FINES/PITCH MIXTURES

The density of pitch and fines mixtures increases with increasing fines content as shown in Figure 4-24. The density increases as the fines have higher density than the coal tar pitch, and there is enough binder to fill the voids between the fines particles. As density increases throughout the fines content range investigated, there is a surplus of pitch.
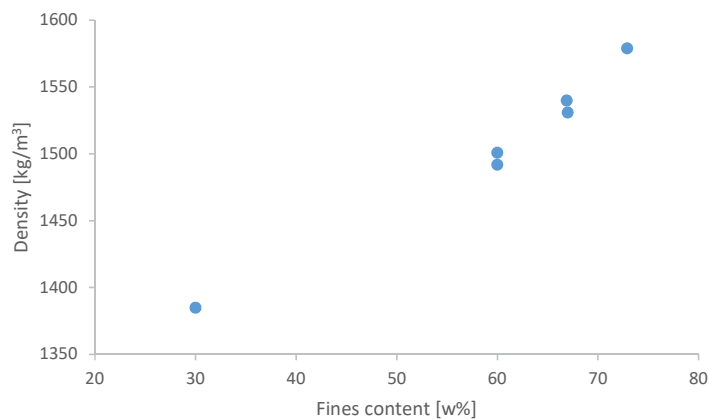

Figure 4-24. Density as a function of fines content for pitch and fines mixtures.

Three of the fines series electrode paste was used in flow measurements with increasing temperature, whereas the rest was used in isothermal flow measurements. The height divided by initial height for the increasing temperature measurements are given in Figure 4-25. An increase in fines content from 60 % (FF-60-1) to 73 % (FF-73-1) decreases the flowability significantly. The sample with 60 % fines is compressed to below 30 % of initial height at 50 °C, while at 73 % fines the compression at 50 °C is above 97 %. The final height of compression for FF-60-1 is restricted by the apparatus, thus the horizontal line above 50° C. In the experiment with 67 % fines the compression of the electrode paste seems to halt at around 50 °C, before it resumes a steady flow. This is probably caused by friction in the equipment used caused by condensed pitch components. The pitch could condense on the bars from the upper plate leaving the furnace up to the LVDT.
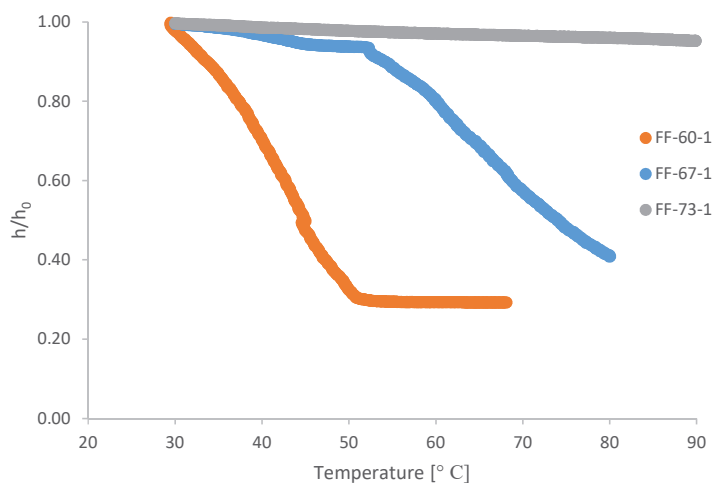
Figure 4-25: Flow measurements of pitch and fines mixtures with 60 % fines (FF-60-1), 67 % fines (FF-67-1) and 73 % fines (FF-73-1).

The apparent viscosity is calculated by equation (4-3), and are presented at 40 and 50 °C in Figure 4-26 with increasing fines content. As fines content increase from 60 to 73 % the apparent viscosity increases with around two orders of magnitude at 40 °C. While at 50 °C the apparent viscosity increases with around three orders of magnitude. The difference in apparent viscosity between the two temperatures decrease as fines content increases. At 73 % fines apparent viscosity at 60 and 70 °C is added, which shows that apparent viscosity increases with increasing temperature. This shows that at 73 % fines the flow of the electrode paste is totally dominated by the fines particles, and thus the friction between particles (Coussot [82]).
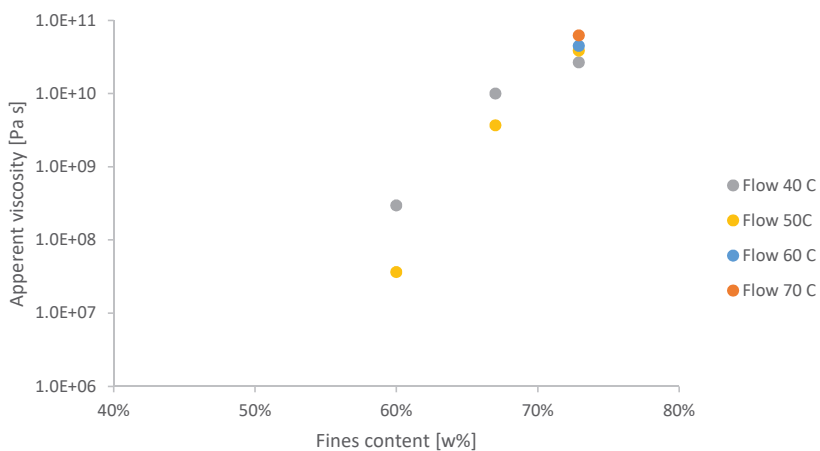

Figure 4-26. Logarithmic plot of apparent viscosity with varying fines contents from 40-50° C for flow measurements (Figure 4-25), calculated with equation (4-3).

4.3.8. ISOTHERMAL MEASUREMENTS OF FINES/PITCH MIXTURES

In Figure 4-27 the isothermal measurement of fines/pitch mixtures are given at 40° C for fines and pitch mixes with fines content 30 %, 60 % and 67 %. As fines content increase, the electrode paste samples flows slower and final compression height increases. At 40° C, the sample with 30 % fines (FF-30-1) is compressed to 50 % of original height at 5 min and 35 % within half an hour. The two samples with 60 % fines are compressed to 59 % and 65 % after 3 hours, while the sample with 67 % fines (FF-67-21) is above 88 % of original height at 3 hours.
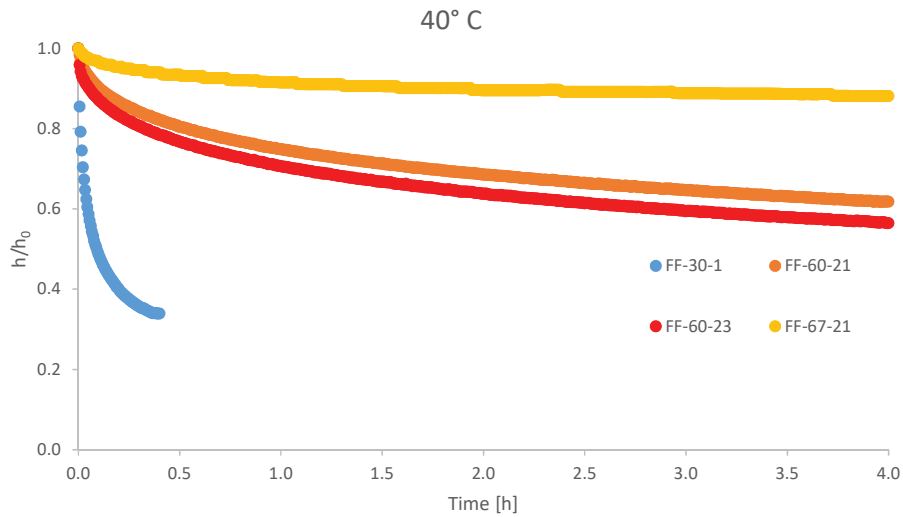

Figure 4-27: The isothermal flow measurements of fines/pitch mixes at 40 °C with green plots of theoretical constant viscosity in green. In blue the sample with 30 % fines, red/orange curve are sample with 60 % fines and yellow curve has 67 % fines.

Shear rates decrease with increasing fines as shown in Figure 4-28 for fines/pitch samples at 40° C. The variability in the measured shear rates increase as fines content increase, as the paste moves from a lubricated to a frictional regime (Coussot [82]). As compression speeds are in the area of 6-60 μm/min for the sample with 67% fines, some of the variability is probably due to movement in the measurement equipment caused by the fan which blows heated air into the measurement furnace. Shear rates are distinctly higher for lower content of fines, which is also shown in Figure 4-27 where height decreases faster for lower fines content.

The shear rates in Figure 4-28 are for the most part larger than in the flow measurements with increasing temperature (Shear rates with increacing temperature have shear rates lowar than $1.1 \cdot 10^{-4}$, especially the part where most of the compression is done. Comparing viscosity measurements for the isothermal and increasing temperature measurements is thus problematic as shear rates differ so much.
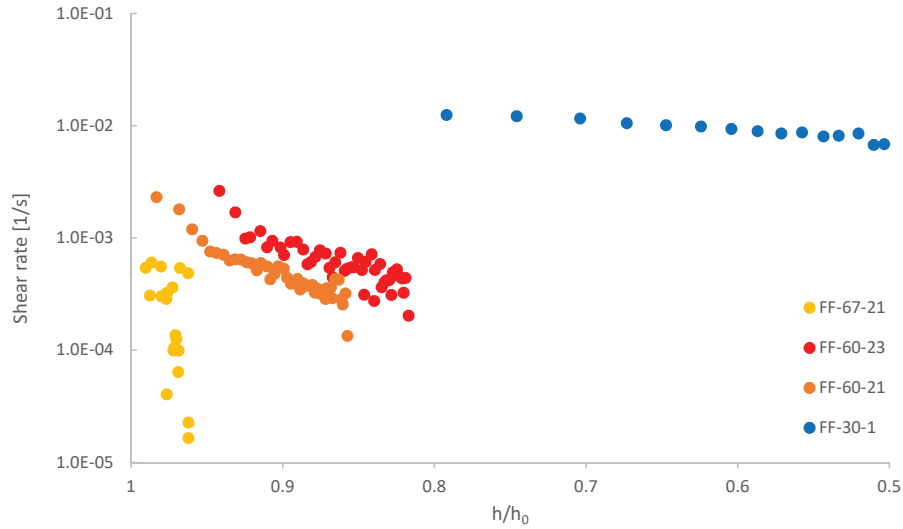
Figure 4-28: Decreasin shear rates as a funtion of height divided by initial height for samples at 40° C. Increasing variabilty as shear rate decreases for all samples.

Since both shear rate and apparent viscosity is calculated from the same data (time and height of sample), they will show the same relative trend between electrode paste samples. Increasing fines content increases apparent viscosity in Figure 4-29. For isothermal measurements, a constant viscosity is expected for Newtonian liquids, but all isothermal measurements of apparent viscosity increase with decreasing height of sample (increasing time). Thus, in these measurement conditions the fines/pitch mixtures does not behave Newtonian.
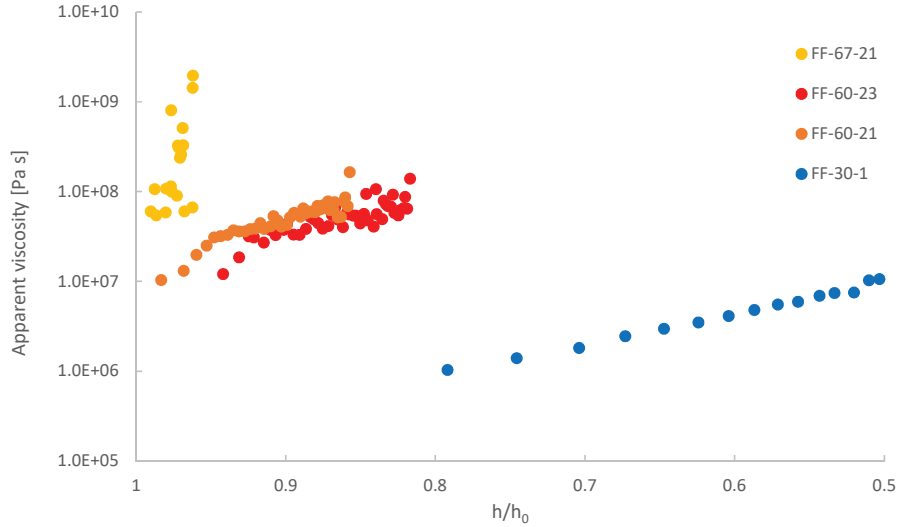

Figure 4-29: Apparent viscosity increases with increasing fines content for samples with 30 % fines (FF-30-1), 60 % fines (FF-60-21 and 23) and 67 % fines (FF-67-21) as a funtion of height divided by initial height.

At 50 °C the difference between samples at 60 % (FF-60-22) and 67 % (FF-67-12 and FF-67-22) fines is shown in Figure 4-30, where the high fines content samples still flow little while the sample with 60 % fines is compressed below 50 % in less than an hour. The 67% fines sample is compressed to about 82% of original height after 3 hours. Increasing temperature by 10° C, compared to Figure 4-28, only decreases relative comression height from 88 % to 82 % for the 67 % fines samples, comared to 59 % to 43 % for the 60 % fines samples. Thus the flow of fines/pitch samples with 67 % fines is mostly restricted by the fines, and not the viscosity of the binder.
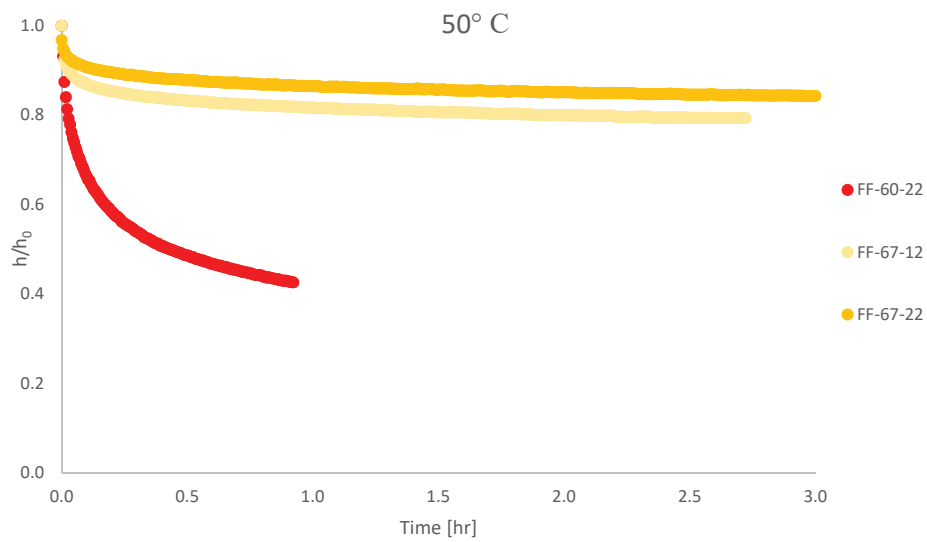

Figure 4-30: The isothermal flow measurements of fines/pitch mixes at 50 °C.

4.3.9.   COARSE CONTENT

The coarse content of a 2-fraction electrode paste has been varied while keeping the pitch/fines ratio constant at two levels, high and low pitch. The resulting electrode paste densities are shown in Figure 4-31 where they increase with increasing coarse content up to 60 % coarse for the low pitch samples. For high pitch samples the pitch/fines ratio are about 67 %, and for low pitch samples the pitch/fines ratio is around 60 %, see Table 4-7 for details.
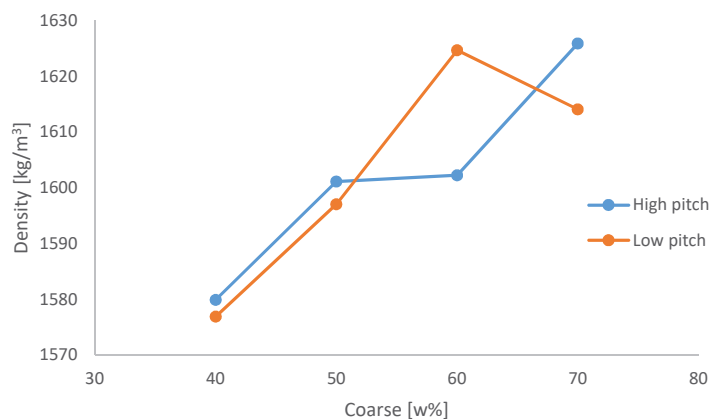

Figure 4-31: Density as a function of coarse anthracite content for electrode pastes with a high and low pitch/fines ratio.

The plasticity of the same samples is shown in Figure 4-32, with very high plasticity at low coarse contents and low plasticity at high coarse content. The high pitch/fines has higher plasticity for 40 % and 70 % coarse content but lower plasticity for 50 % and 60 % coarse content.
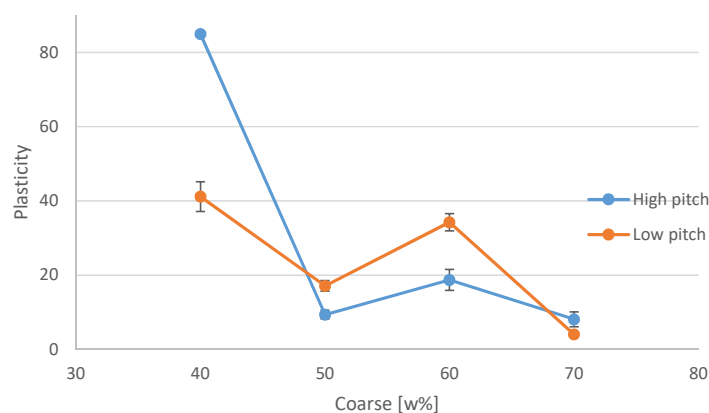

Figure 4-32: Plasticity for high and low pitch electrode pastes samples with increasing coarse filler content.

The resulting flow curves are given in Figure 4-33, where sample height divided by initial height is plotted against temperature. The contents of each sample is given in Table 4-7, and the different coarse contents are given in different colors in Figure 4-33, where the darker shade of the color has the higher pitch content. As coarse content decrease, the electrode paste cylinders are more easily compressed. Comparing mixes with same amount of coarse fraction, the mix with more binder is more easily compressed.
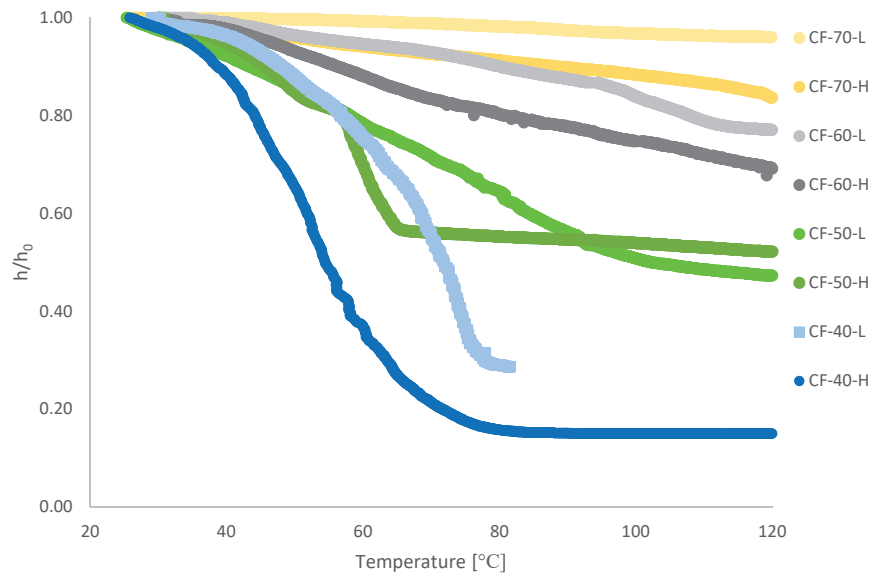

Figure 4-33: Height divided by initial height for samples with varying fines content and pitch/fines ratio, high and low.

From the flow curves with low pitch/fines ratio the height divided by initial height for 40, 50 and 60 °C has been plotted with increasing coarse content in Figure 4-34. At 40 and 50 °C h/h_0 decreases when coarse content increases from 40 to 50%, whereas at 60 °C the height ration increases with increasing coarse content. At higher coarse contents, h/h_0 increases with increasing coarse content at the temperatures 40, 50 and 60 °C.
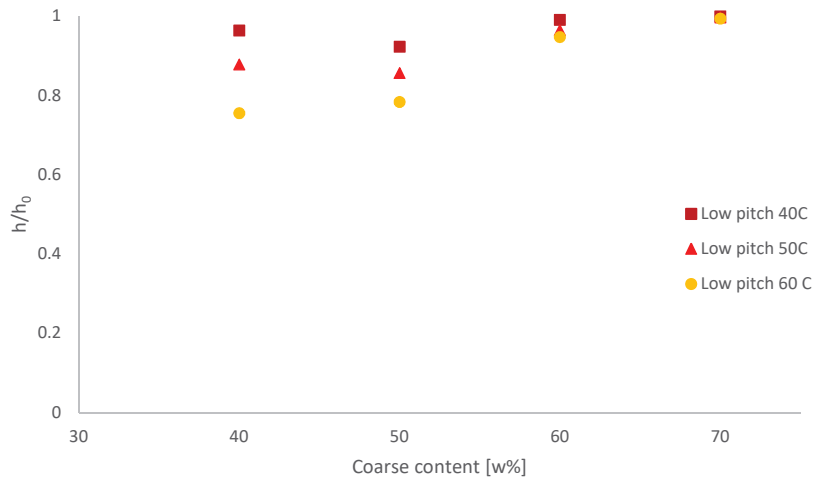
Figure 4-34: Height divided by initial height with increasing coarse content for the low pitch/fines ratio samples at 40, 50, 60 °C.

The h/h$_0$ ratio for high pitch/fines samples are shown in Figure 4-35, where the spread of the measurements is bigger compared to the low pitch/fines samples. As coarse content increase h/h$_0$ increases for all temperatures, with the biggest difference at 60 °C which increased from less than 40 % of h$_0$ at a coarse content of 40 % up to 94% of h$_0$ at 70 % coarse content. The difference in h/h$_0$ between 40 °C and 60 °C, decreases as coarse content increases and is almost negligible at 70 % coarse content.
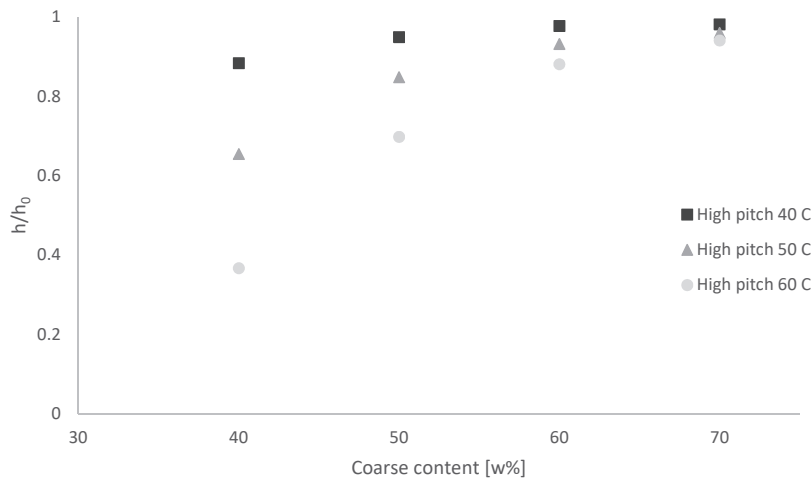

Figure 4-35: Height divided by initial height with increasing coarse content for the high pitch/fines ratio samples at 40, 50, 60 °C.

The apparent viscosity of the electrode paste is calculated by equation (4-3), and is presented in the following two figures. The viscosities are calculated at 40, 50, and 60° C. In Figure 4-36, the apparent viscosity of the low pitch/fines ratio is generally increasing as coarse content increase for all temperatures.
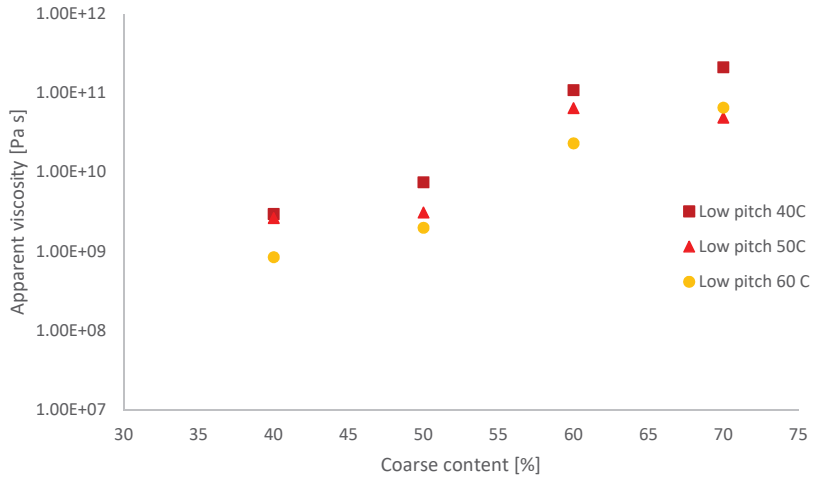

Figure 4-36: Apparent viscosity with increasing coarse content for the low pitch/fines ratio samples at 40, 50, 60 °C.

At high pitch/fines ratios, the difference in apparent viscosity with increasing temperature is higher. The apparent viscosity at 60° C is distinctly lower than that of the lower temperatures in Figure 4-37. At both 50 and 60° C there is very little increase in viscosity from 60 to 70 % coarse material.
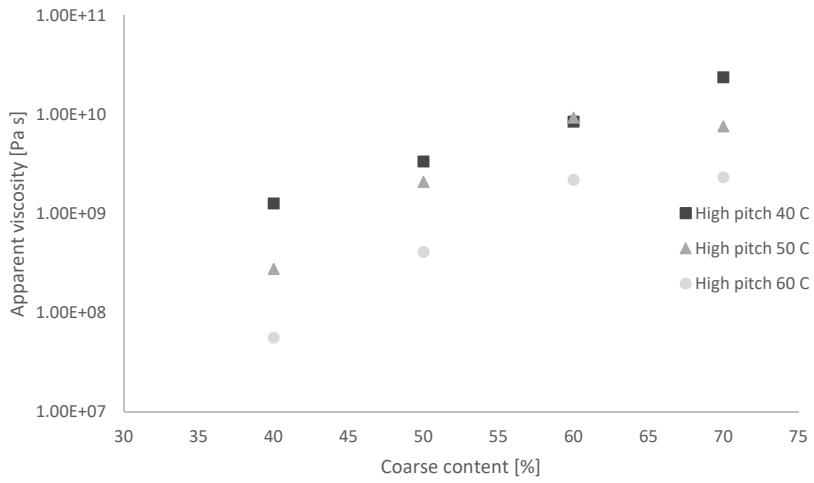

Figure 4-37: Apparent viscosity with increasing coarse content for the high pitch/fines ratio samples at 40, 50, 60 °C.

4.4.DISCUSSION

4.4.1.   METHOD

FLOW MEASUREMENTS

Measuring flow of electrode paste samples with different starting heights give similar flow profiles (h/h_0) down to a point where coarse particle interaction with the plates slows the flow of the electrode paste samples with low height, as seen in Figure 4-14 and Figure 4-16. As long as samples are of similar initial height and with measuring range above five times the D90 of the coarse particles, the method will give similar flow diagrams when height divided by initial height is plotted against temperature. A doubling in heating rate, from 2°C/h to 4°C/h gives the same flow profile, see Figure 4-10. Thus, flow profiles are robust against uneven heating rates and small changes in initial height.

As a test on how heating rates would influence the flow curve of electrode paste the height of a sample with a given viscosity function during heating, can be calculated using a modified version of the Dienes and Klemm equation (2-37). With known initial height, force on the sample, volume of the sample and the times (t_1 and t_2) the new height, h_2, can be found with equation (4-4)

$$\frac{1}{h_2^4} = \frac{8\pi F(t_2 - t_1)}{3V^2 \, \eta(T)} + \frac{1}{h_1^4} \qquad (4\text{-}4)$$

In this model, a viscosity function was chosen to fit the experimental flow curves. The Arrhenius expression

$$\eta(T) = 4 \cdot 10^{-8} e^{\frac{1.3 \cdot 10^4}{T}} \qquad (4\text{-}5)$$

gave the flow curves shown in Figure 4-38. The modelled flow curves are compared to one of the measured samples. Due to the lower time the high heating rate sample has on each temperature; the flow will be slower compared to the normal heating rate in the modelled cases. In the experiments, the higher heating rate give higher shear rates, which lowers the apparent viscosity, which leads to similar flow as a function of temperature for the two heating rates.

In the literature, Rand [44] discourage from using the Arrhenius expression on coal tar pitches on temperatures below 120-150° C above the glass transition temperature (T_g). Using the relationship between T_g and the Ring and Ball softening point (Equation (2-55)), the glass transition temperature of the coal-tar pitch used is 12.8° C, and the flow measurement range below the temperature limit set by Rand. Assuming an Arrhenius temperature dependence of viscosity in electrode paste in temperatures around the softening point of the pitch, as done in Figure 4-38, is a simplification that managed to give a quite good fit to the experimental data. As the experimental set-up was designed to be similar to industrial use of electrode paste, this simplification could be used to model the melting of electrode paste in an industrial furnace.
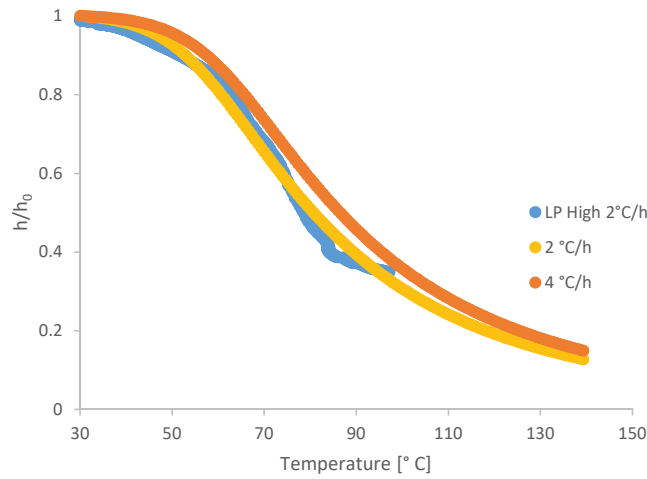
Figure 4-38: Flow curves of models with heating rate 2 °C/h and 4 °C/h, compared with the flow curve of LP high 2 °C/h

VISCOSITY

As described in Chapter 2 the equation of motion *(2-21)* is central in developing working equations for the parallel plate viscometer. In this section, the assumptions made will be discussed.

$$\frac{\delta}{\delta t}\rho\boldsymbol{v} = -(\nabla \cdot \rho\mathbf{vv}) - \nabla\mathrm{p} - (\nabla \cdot \boldsymbol{\tau}) + \rho\boldsymbol{g} \qquad\qquad (2\text{-}21)$$

The assumptions that body forces can be neglected and that creeping flow conditions exists should be valid as the weight on the sample is high and the flow is very slow.

A quasi stationary state is assumed, i.e. at a given time the momentum balance is given by a stationary hydrodynamic problem, while the mass balance will take changes in time into consideration. At the start of each experiment, *dv/dt* is not negligible and thus solutions are not applicable as the experiments starts. As plate speed is not constant the influence of inertial effects has been checked by equation (2-49), as proposed by Bird, et al. [89], and found to be negligible for all experiments. The inertial effects are sufficiently low because of low plate speed caused by the high viscosity of the pastes at the temperatures used during measurements. For isothermal measurements, with the highest changes in plate speed during the start of the experiments, the highest influence of inertial effects is nine orders magnitude lower than the pure Dienes and Klemm expression.

For constant density and viscosity (incompressible fluid), the equation of motion can be simplified to the Navier-Stokes equation (2-23) for incompressible flow. Assuming constant (Newtonian) viscosity for electrode paste is in the best case optimistic. The binder phase has been found to behave Newtonian at temperatures above the softening point (>20 °C) (Nazem

[96], Fitzer, et al. [97] and Eie, et al. [99]), while Nair [107] and Briggs [108] found non-Newtonian behavior of high TI pitches at lower temperatures. Furthermore, pastes with high amounts of solids are known for their non-Newtonian behavior, as can be seen in Figure 2-15. As fines concentration increase from 0 -30 % in experiments with concentric cylinders, the viscosity measurements show a tendency towards more non-Newtonian flow in Figure 4-8. Isothermal flow measurements in Figure 4-44 also show that increasing fines content gives larger deviation from equations assuming Newtonian viscosity. Thus, it is likely that the electrode paste, typically with 40-60 % fines, will not behave Newtonian in the temperature range around the softening point of the binder.

The no-slip assumption at the interface between plate and electrode paste is believed to hold. In Figure 4-39, Mavridis, et al. [109] showed how a polymer sample barrels outwards and up against the plate during compression. As the electrode paste sticks to the aluminum foil on the plates, a similar flow pattern is plausible for the electrode paste.

The assumption that vertical velocity, v_z, is only a function of vertical position, i.e. uniform vertical velocity in the radial direction, works well for radius/height ratios above 10. Mavridis, et al. [109] has shown in Figure 4-39 that vertical velocity is not uniform in radial direction for a polymer following the power law of Scott [92], Equation (2-51). The analytical solution in Figure 4-39 showed good accordance with experiments, and for an analytical Newtonian fluid, the radial tracers remained parallel. Radius/height ratios used were around ½ at start of experiments, and it is shown that the analytical solution differ significantly from Scotts equation when radius/height ratios are below one.
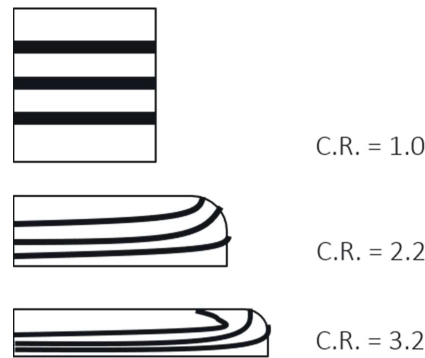

Figure 4-39: Analytical solutions to barreling of radial tracers in isothermal flow (power law index = 0.3) of a polymer sample, redrawn from Mavridis, et al. [109]. C.R.is the compression ratio (h_0/h).

Tørklep [86] proposes to use the approach of Gent [91], equation (2-44), which combines both elongational and squeeze flow additively in the solution for the force on the plate. Coussot [82] also proposes to use a combination of elongational- and squeeze flow for intermediate radius/height ratios, but with solutions that are more general. It is stated that elongational flow works well for radius/height ratios below 0.1 and squeeze flow at ratios above 10.

In Figure 4-40, the solution of Bergstrøm (equation (2-43)) is compared to the pure squeeze-(Dienes and Klemm equation (2-37)) and elongational-flow (equation (2-44)) on the LP-High

electrode paste. The Bergstrøm solution used in this work gives apparent viscosities similar to the elongational flow equations. As the height is reduced at higher temperatures, the elongational and squeeze flow solutions are closer.
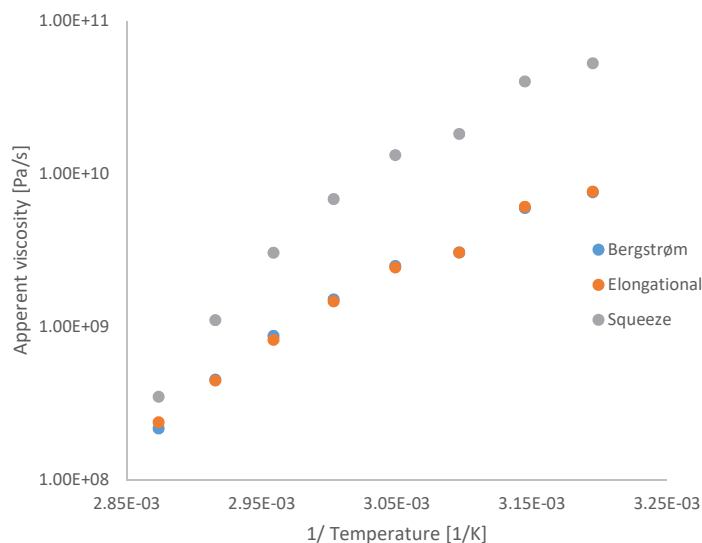

Figure 4-40: Calculated apparent viscosities for the three methods Bergstrøm, Elongation and Squeeze as a function of inverse temperature. Higher temperatures to the left.

Tørklep [86] accepted the complex rheological behavior of carbon anode pastes, but still uses the solution for Newtonian flow even though solutions for non-Newtonian fluids, e.g. Scott [92] for power-law fluids, were available. Engmann, et al. [85] reviews solutions for a long list of fluids e.g. Bingham, power-law, and linear elastic fluids, but finding parameters for the solutions in such rheological models requires a substantial amount of work, and the applicability of the resulting model is usually limited to the exact material. The setup used for the parallel plate measurements resembles the industrial application of Søderberg electrode paste, where height/radius ratio, force on sample, and shear rates are similar in experiments and the industrial furnaces. Thus, using the solutions of Tørklep/Bergstrøm should give measurements usable to describe the flow of electrode paste in industrial electrodes.

SHEAR RATE

Shear rate is calculated as the maximum shear rate in the sample, as Tørklep [86] describes, using Equation (2-48). Using a fixed force on the plate results in varying plate speeds, and thus the shear rate in the sample is not constant during measurements, as shown in Figure 4-12. The shear rate increases as the sample apparent viscosity decreases and the height decrease. This causes a problem as the viscosity in shear thinning materials is also dependent on the shear rate. Comparing different samples viscosities when the shear rate is not the same will thus not give a meaningful comparison of the samples.

INCREASING TEMPERATURE

Using an increasing temperature during viscosity measurements is not recommended as there will be temperature gradients in the sample. But with very low heating rates the temperature gradients will be low, and in industrial use, the electrode paste is heated up as it moves down in the electrode column. The experimental set-up with increasing temperature will resemble the industrial use of electrode paste, thus this approach can be useful to describing the apparent viscosity of electrode paste in industrial models.

ISOTHERMAL MEASUREMENTS

For isothermal measurements the problems with increasing temperature and temperature gradients in the sample is evaded. But as you add force to a sample it will compress faster than a sample under constant load. Thus, the shear rate during compression are quite high, as shown in Figure 4-41, compared to what is normal in industrial electrodes ($5 \cdot 10^{-5} - 2 \cdot 10^{-4} s^{-1}$). As the shear rate varies during the measurement, it is not possible to get a defined viscosity at a defined temperature and shear rate.
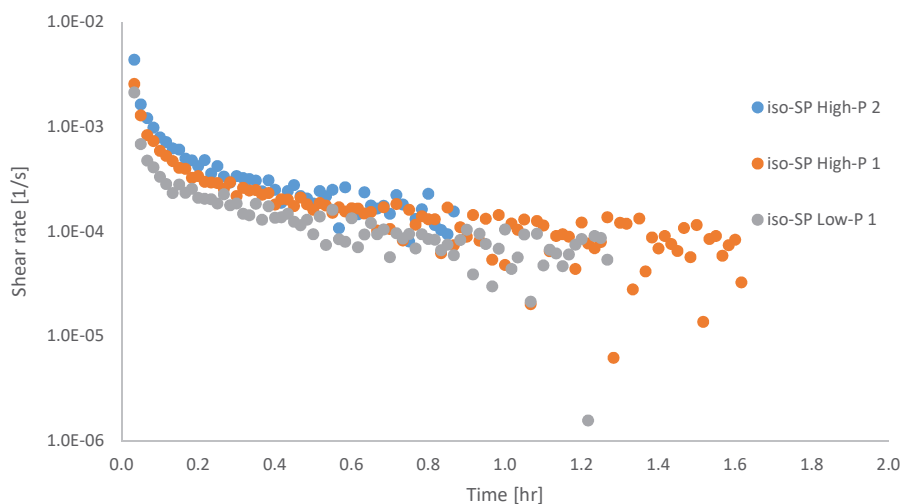

Figure 4-41: Shear rates in samples during isothermal measurements

It was shown in Table 4-11 that the gap size needs to be at least 5 times the D90 of the coarse material, which implicate that the sample height must be higher than what is assumed in the working equation for apparent viscosity. As the experimental set-up deviates from the assumptions made (Newtonian viscosity and height of sample) in the equation for apparent viscosity, the applicability of the results is limited. Given similar shear rates in industrial electrodes, the calculated apparent viscosity should give indications to how electrode paste will flow in industrial furnaces. It can also be used to differentiate between pastes, as it easier to see differences between apparent viscosities than the height of the sample at a given temperature, as will be discussed next.

4.4.2. VISCOSITY OF ELECTRODE PASTE

The flow profiles are quite robust against changes in the electrode paste as well, seen in Figure 4-19, and it is challenging to tell different pastes apart. As some of the measurements in Figure 4-19 of the two different pastes are on top of each other. To see differences in flow properties of two pastes can be done by calculating the apparent viscosity, as seen in Figure 4-42, where the large particle paste has a higher apparent viscosity at lower temperatures. Thus, for differentiating between pastes it can be valuable to calculate apparent viscosity, in combination with showing flow profiles.
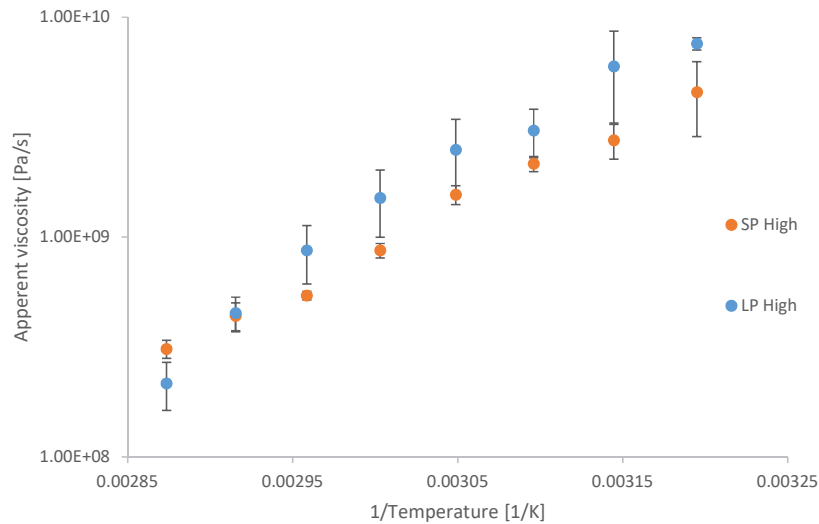

Figure 4-42: Apparent viscosities of two electrode pastes, one with larger coarse particles (LP High) and the other with smaller coarse particles (SP High). The electrode paste with smaller particles has lower viscosity at lower temperatures compared to the paste with larger particles.

4.4.3.   FINES AND PITCH MIX

In Figure 4-43 Tørklep [86] shows how ball mill fines influence the viscosity of a pitch/fines mixture, and how the pitch/fines mixture reach a saturation limit for where flow stops. In Figure 4-25, 73 % fines is close to (or at) this saturation limit, as there is very little flow and viscosity does not decrease with increasing temperature. Addition of small amounts of fines will significantly increase apparent viscosity in the concentration range of 60 % fines, as shown in Figure 4-26.
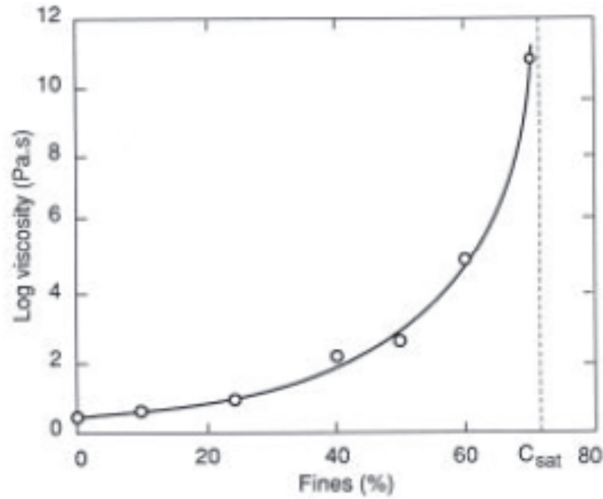

Figure 4-43: Viscosity of pitch/fines mixtures at 150° C for 105° C Mettler softening point pitch, from Tørklep [86], Copyright © by The Minerals, Metals, Materials Society, used with permission.

ISOTHERMAL MEASUREMENTS

To compare the experimental data to a constant viscosity sample, equation (2-43) was rearranged and integrated with respect to time to give equation (4-6).

$$t(h) = \frac{3\eta V^2}{2\pi F} \left(\frac{-2}{3h_0 h^3} + \frac{1}{2h_0^2 h^2} + \frac{4\pi}{2h_0 V} \ln \frac{h}{h_0} + \frac{1}{6h_0^4} \right) \tag{4-6}$$

The time (t) it takes to compress a sample with apparent viscosity (η) to a given height (h) can be calculated for different viscosities. These plots are compared to experimental data, previously shown in Figure 4-27 and Figure 4-30, in Figure 4-44 and Figure 4-45. The only sample that follows a constant viscosity, according to equation (4-6), is the 30 % fines sample. As fines content increase it is not possible to fit the compression to a constant viscosity, which indicates that friction between fines particles has an impact on flow properties at higher concentrations.
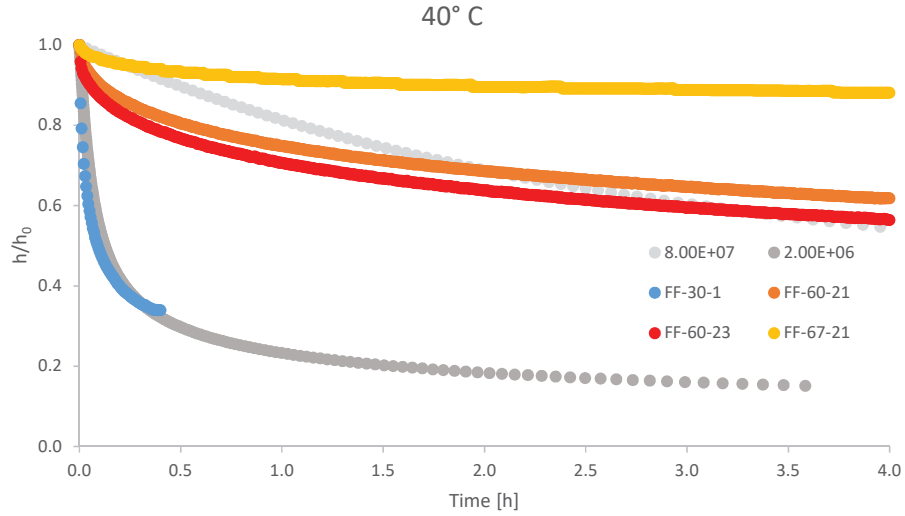
40° C

Figure 4-44: The isothermal flow measurements of fines/pitch mixes at 40 °C with green plots of theoretical constant viscosity in green. In blue the sample with 30 % fines, red/orange curve are sample with 60 % fines and yellow curve has 67 % fines.

At 50° C, in Figure 4-45, neither samples at 60 %, nor 67% fines fit the constant viscosity lines according to equation (4-6). This indicates that the flow of these pastes is non-Newtonian and influenced primarily by the high fines content. Shear rates for the 50° C isotherms follows the same trend as the 40° C isotherms in Figure 4-28, and can be found in Appendix, Figure A - 5.
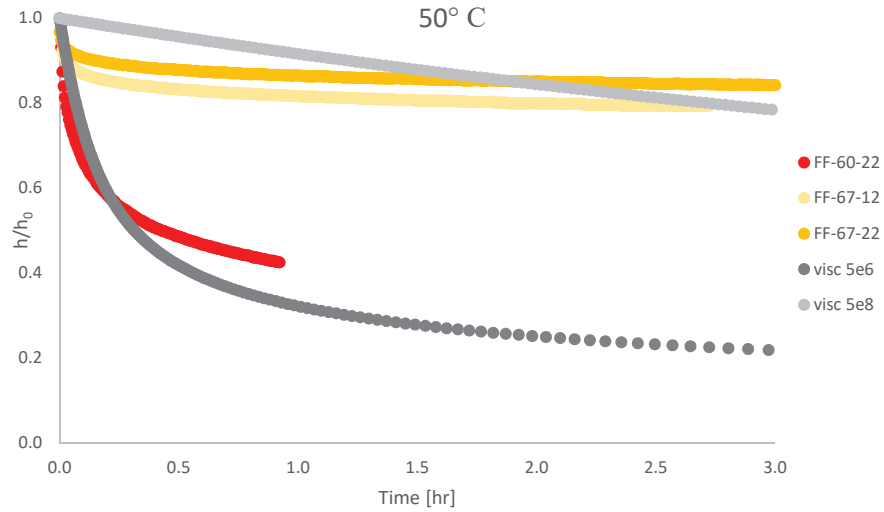
50° C

Figure 4-45: The isothermal flow measurements of fines/pitch mixes at 50 °C.

The viscosity of coal tar pitch is in the literature found to be Newtonian for temperatures above 20° C above the softening point of the binder (Nazem [96], Fitzer, et al. [97] and Eie, et al. [99]), while at lower temperatures the coal tar pitch behaves non-Newtonian (Fitzer, et al. [97]). For coal tar pitch and fines mixtures Tørklep [86] states that the coal tar pitch retains the Newtonian properties up to a fines content of 40 %, which agrees with Figure 4-44 where the sample with 30 % fines has a flow profile similar to a constant viscosity model. For samples with 60 % and 67 % fines it is not possible to fit a constant viscosity function to the experimental data in Figure 4-44 and Figure 4-45.

4.4.4.   COARSE PARTICLES

The pitch/fines density at 60% fines was found from the fines fraction experiments to be 1496.5 kg/m^3, and the coarse fraction density in water was used to find the volume percentage of coarse fraction in each mix, see Table 4-12. The ratio of vibrated bulk density (VBD) and density in water (d_{H_2O}) for the coarse fraction is 60.9 %, and an approximation of the maximum volume percentage coarse. As can be seen in Table 4-12 the samples with 70 % coarse exceeds this limit, and due to this flow should be limited by particular flow of coarse material. As the paste flows to some degree, the particles are not locked but restrained by friction between coarse particles as described by Coussot [82].

Table 4-12: The percentage of fines in the fines/pitch part and the volume percentage of coarse material in the coarse fraction sample series.

Coarse series	Coarse content [%]	Volume percentage of coarse [%]	% fines of (fines + pitch) [%]
CF-40-H	40	**33.4**	**59.9**
CF-40-L	40	33.8	61.9
CF-50-H	50	**42.6**	**59.9**
CF-50-L	50	43.3	62.8
CF-60-H	60	**52.2**	**59.8**
CF-60-L	60	53.0	62.7
CF-70-H	70	61.8	57.4
CF-70-L	70	**62.8**	**60.6**

In the coarse fraction measurements, the percentage of fines in the pitch/fines mix are shown in Table 4-12 and the ones closest to 60 % are in bold. In Figure 4-46, the coarse fraction experiments with 60 % fines in the pitch/fines matrix are compared to the pitch/fines sample with 60 % fines. This show how increased amount of coarse fraction delays flow in the electrode past. At 60 % coarse added the flow is restricted by the coarse particles and at 70 % coarse content there is no flow of the electrode paste.
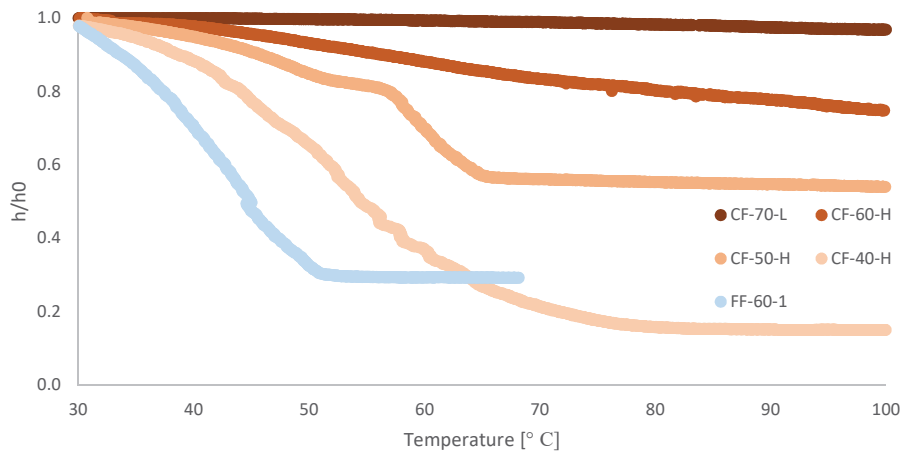
Figure 4-46: Coarse fraction flow measurements with 60 % fines in the fines/pitch matrix, compared with only 60 % fines and pitch.

VISCOSITY WITH INCREASED COARSE CONTENT

The apparent viscosity from experiments with increasing coarse content is shown in Figure 4-47, Figure 4-48, Figure 4-49 at 40° C, 50° C and 60° C respectively. With increasing apparent viscosity from 40 % up to 60 % coarse material. At 50° C the apparent viscosity of both the high pitch and the low pitch sample decrease from 60 to 70% coarse. Thus, the electrode paste flow is limited to particle-particle interaction also at 60 % addition of coarse material.
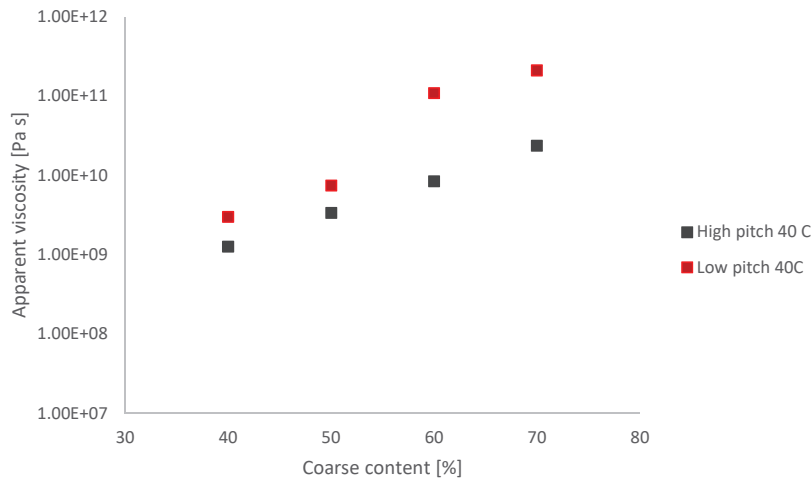

Figure 4-47: Apparent viscosity of electrode paste with increasing coarse content at 40° C with high and low levels of pitch.
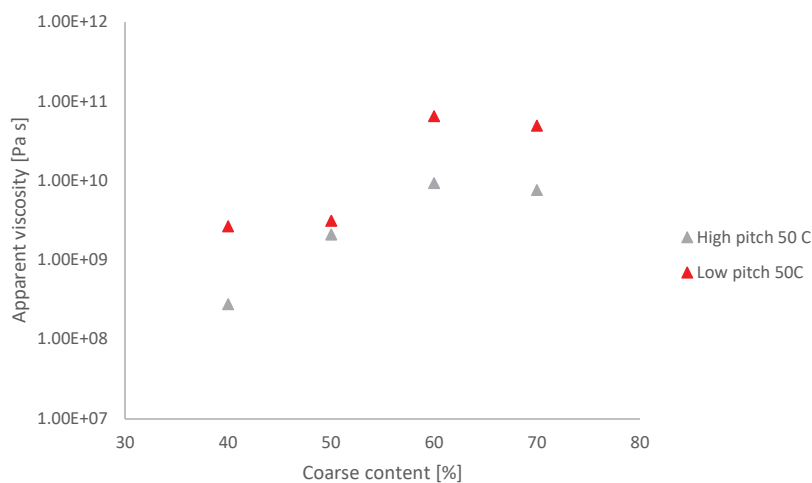
Figure 4-48: Apparent viscosity of electrode paste with increasing coarse content at 50° C with high and low levels of pitch.
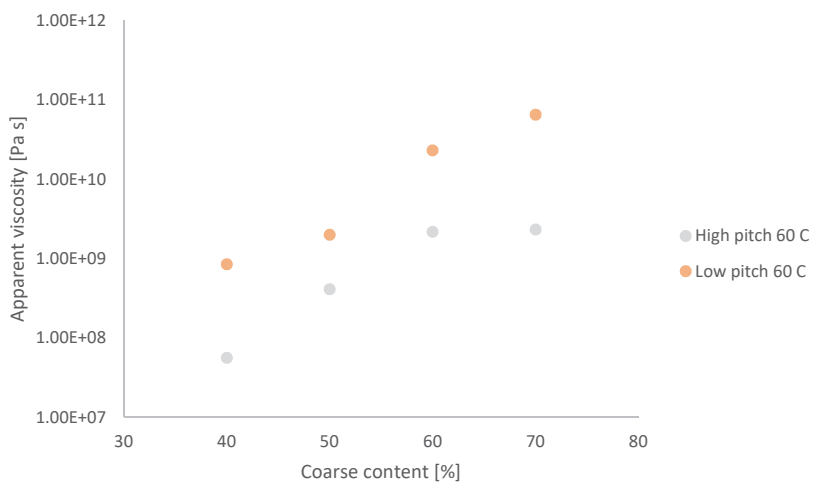
Figure 4-49: Apparent viscosity of electrode paste with increasing coarse content at 60° C with high and low levels of pitch.

The measured apparent viscosity for increasing coarse content is showed in Figure 4-50 and Figure 4-51 compared to suspension viscosity models by Krieger and Dougherty [79] (Equation (2-11), with intrinsic viscosity = 5/2) and equation (2-12) from Coussot [82]. The measured viscosity for a fines and pitch mix at 60 % fines is used as the viscosity of the suspending medium. At 40° C the models fit quite well with increasing coarse contents up to 60 %. Coarse contents of 70 % are not included as it is above the maximum volume percentage of particles found by the VBD/d_{H_2O}) ratio. At 50° C the models show a discrepancy compared

to the measured value, probably due to a change in the viscosity of the suspending medium. As the coarse material will be wetted by some of the coal tar pitch, less coal tar pitch is available for the fines.

The models used have shown good correlation with monodisperse, spherical particles, different from the coarse anthracite used. Thus, models like the ones used are not expected to fit very well. Coussot [82] also states that these models are problematic as the volume fraction of solids increase. In electrode pastes the volume fraction of solids is high.

Figure 4-50: Measured apparent viscosity at 40° C versus calculated viscosities with the Krieger-Dougherty and Coussot equations for coarse content 40-60 w%. Measured apparent viscosity starts at 0 w%, which is used to calculate the viscosities at higher particles content.
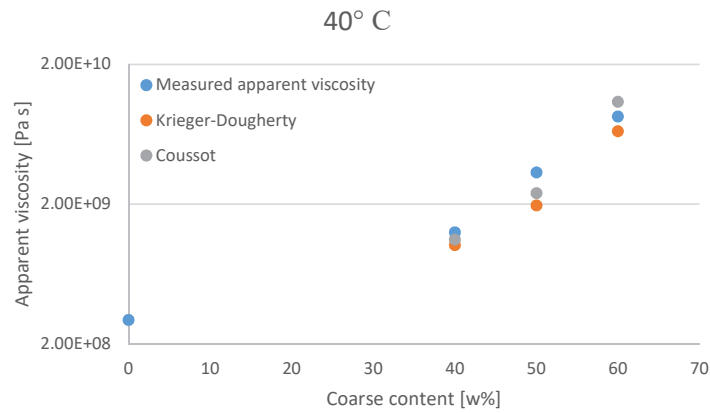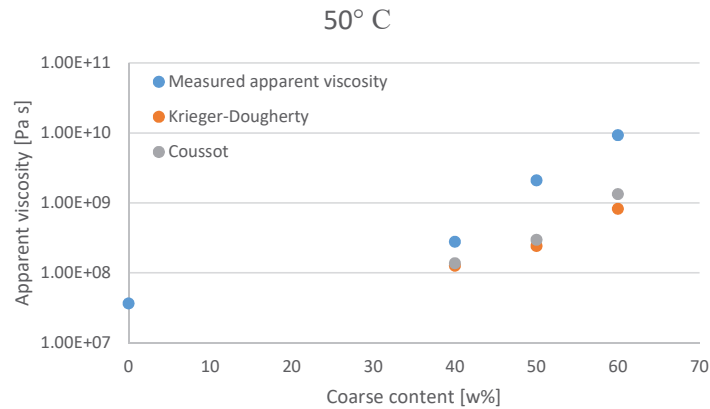

Figure 4-51: Measured apparent viscosity at 50° C versus calculated viscosities with the Krieger-Dougherty and Coussot equations for coarse content 40-60 w%. Measured apparent viscosity starts at 0 w%, which is used to calculate the viscosities at higher particles content.

4.5.CONCLUSION

Flow measurements can predict how electrode paste flows in an industrial electrode. The method gets similar results for a doubling of heating rate and decreasing the sample height to the half, if the plate distance is more than 5 times the D90 of the largest particles in the paste. The electrode pastes used, start to flow at 25 °C below the softening point of the binder, and reach 50 % of the original height at 70 – 80 °C.

Apparent viscosity of electrode paste has been found at temperatures and shear rates similar to industrial application of the pastes. Electrode paste has a shear thinning behavior under these measurement conditions.

The measured viscosity is an apparent viscosity because many of the assumptions in the underlying equations to the parallel plate viscometer are not followed. Among other things the shear rate varies during measurements and is not even throughout the sample. Thus, apparent viscosity found in this work is only applicable under the same conditions as the experiments done, and can be used, with awareness, in industrial electrodes as measurement conditions are close to what is seen in industrial electrodes.

Coal-tar pitch and fines mixes are found to behave non-Newtonian above 30 % addition of fines in this work. Increased fines content increases the viscosity of the mix. 73% fines are found to "lock" the system, and the viscosity of this system is governed by the particle-particle interactions in the mix.

Isothermal measurements were found to be less effective, as the shear rates varies over many orders of magnitude and are higher than used in industrial electrodes. Many measurement series are needed to get apparent viscosities at the temperature range seen in industrial electrodes. These measurements can however be used to give insights into how electrode paste flows after charging of new paste, as the charged paste will increase pressure on the electrode paste.

Increased coarse content increases apparent viscosity. Apparent viscosity of electrode pastes with more than 60 % coarse particles are heavily influenced by particle-particle interactions, as apparent viscosity does not increase much with more addition of coarse material. Paste with 70 % coarse particles have very little flow at temperatures up to 120 °C.

CHAPTER 5   CONCLUSIONS AND FURTHER WORK

Temperature profiles show that the electrode paste has filled the electrode casing at approximately 80° C. In flow measurements of electrode paste, the height is reduced to about 45 % of the original height at 80° C. In industrial electrodes a 45 % reduction of electrode paste height will not fill the whole electrode casing as ratios between the radius of electrode paste cylinders and the electrode casing is between 0.45-0.50. Thus, the height needs to be reduced to 25-30 % of the original height to fill the casing. At 80° C, as observed in the industrial temperature measurements, the electrode paste has probably not filled the whole casing. The cylinders will probably go through the molten paste level and continue to increase in temperature until it fills the casing. Then it can be pushed upwards by the pressure from the cylinders above and be cooled as it flows upwards and reach the molten paste level. Big difference in molten paste level temperature and flow measurements can indicate poor melting conditions in the industrial electrode.

When facing electrode problems like hard and soft breakages, temperature measurements can be performed to find what temperatures the electrode paste experiences before it is baked to a solid electrode. The electrode paste flow can be a part of the root cause of the problems. In these cases, knowledge about the flow properties and viscosities of electrode paste, can make it possible to design an electrode paste with correct flow properties according to the temperatures measured in the electrode.

Temperature measurements can be valuable when searching for new binders, e.g. binders with less PAH. The new binder must melt and bake at temperatures measured in industrial electrodes. Thus, the viscous properties of the binder and the new electrode paste must be designed so that it enables the electrode paste to fill the whole casing. Measurements of flow on electrode paste with new binders will then show if the electrode paste can be used in a Søderberg electrode.

It has been shown that doubling the heating rate of flow measurements gives the same flow profiles, when plotted against temperature. Thus, increased slipping on an electrode should give similar melting of the electrode paste as long as temperatures in the electrode column are similar. To have similar temperatures during high slipping it can be recommended to increase heating of the electrode air to ensure good melting conditions for the electrode paste.

5.1. FURTHER WORK

Temperature measurement campaigns should be used to check how new electrode equipment, e.g. copper shields against induction and increased heating of electrode air, changes the temperatures inside the column. Quantifying the change in temperature will help finding the best corrective measures on electrodes that have problems with electrode melting, e.g. segregation.

More research should be done on finding a good method for evaluating the viscosity in electrode paste. More work on non-Newtonian viscosity models for the parallel plate viscometer is one way to go. A constant velocity parallel plate viscometer can also be utilized, because it is easier to control shear rate when the plate speed can be controlled. When shear rate is controlled it easier to differentiate the viscosities of different electrode pastes.

Increased knowledge about the viscosity of electrode paste will help with modelling of the electrode paste flow in industrial electrodes. Models can be useful to better understand the segregation problems at the top of some electrodes.

In this work it has been found that high amounts of fine particles and high amounts of coarse particles obstruct flow of electrode paste. To study how different particle size distributions affect flow properties, would be valuable, as electrode paste can be designed to flow as wanted when the temperatures in the electrode column is known.

More work should also be done on the viscosity of electrode paste on higher temperatures, as temperatures above 200° C are found in large areas above the contact clamps on some electrodes. This will give information on how the electrode paste behaves beneath the molten paste level and this will give increased insights into the cause of segregation in electrode paste.

BIBLIOGRAPHY

[1]   C. W. Søderberg, "Electrode for electric furnaces and process for manufacturing the same,"
        United States, 1923. Available: http://www.freepatentsonline.com/1440724.html.

[2]   B. Larsen, H. Feldborg, and S. A. Halvorsen, "Minimizing thermal stress during shutdown of
        Søderberg electrodes," in *INFACON XIII*, Almaty, Kazakhstan, 2013, pp. 453-466: P. Dipner.

[3]   L. R. Nelson and F. X. Prins, "Insights into the influence of paste additions and levels on
        søderberg electrode management," in *INFACON X: Transformation through technology*, Cape
        Town, South Africa, 2004, pp. 418-431.

[4]   R. J. Ord, J. G. Schofield, and C. G. Tan, "Improved performance of Soderberg electrodes,"
        (in eng), *CIM bulletin,* vol. 88, no. 991, pp. 97-101, 1995.

[5]   A. Schei, J. K. Tuset, and H. Tveit, *Production of high silicon alloys*. Trondheim: Tapir, 1998,
        pp. 363 s., ill.

[6]   L. Shoko, J. P. Beukes, and C. A. Strydom, "Determining the baking isotherm temperature of
        Söderberg electrodes and associated structural changes," *Minerals Engineering,* vol. 49, no. 0,
        pp. 33-39, 8// 2013.

[7]   I. McDougall, "Ferroalloys Processing Equipment," in *Handbook of Ferroalloys*, M. Gasik,
        Ed. Oxford: Butterworth-Heinemann, 2013, pp. 83-138.

[8]   T. Foosnæs and T. Naterstad, "Carbon: Basics and Principles," in *Introduction to aluminium
        electrolysis : understanding the Hall-Héroult process*, K. Grjotheim and H. Kvande, Eds. 2nd
        ed. Düsseldorf: Aluminium-Verlag, 1993, pp. XII, 260 s., ill.

[9]   H. Jalkanen and M. Gasik, "Theory of Ferroalloys Processing," in *Handbook of Ferroalloys*,
        M. Gasik, Ed. Oxford: Butterworth-Heinemann, 2013, pp. 29-82.

[10]   M. Tangstad, "Manganese ferroalloys," in *Metal production in Norway*, M. Tangstad, Ed.
        Trondheim: Akademika Publishing, 2013.

[11]   T. Rosenqvist, *Principles of extractive matallurgy*, 2nd ed. Trondheim, Norway: Tapir
        Academic Press, 2004.

[12]   L. Holappa, "Basics of Ferroalloys," in *Handbook of Ferroalloys*, M. Gasik, Ed. Oxford:
        Butterworth-Heinemann, 2013, pp. 9-28.

[13]   M. Tangstad, "Ferrosilicon and Silicon Technology," in *Handbook of Ferroalloys*, M. Gasik,
        Ed. Oxford: Butterworth-Heinemann, 2013, pp. 179-220.

[14]   Elkem-Carbon, "Søderberg Electrode Manual," Internal, 1991.

[15]   J. A. Persson, "Iron free self baking electrode," US, 1986. Available:
        http://www.google.no/patents/US4575856.

[16]   D. F. Shriver and P. W. Atkins, *Inorganic chemistry*, 3 ed. Oxford: Oxford University press,
        1999.

[17]   G. G. Wallace, S. E. Moulton, R. M. I. Kapsa, and M. J. Higgins, "Carbon," in *Organic
        Bionics*: Wiley-VCH Verlag GmbH & Co. KGaA, 2012, pp. 41-79.

[18]   B. McEnaney, "Structure and Bonding in Carbon Materials," in *Carbon Materials for
        Advanced Technologies*, T. D. Burchell, Ed. Oxford: Elsevier Science Ltd, 1999, pp. 1-33.

[19]   I. A. S. Edwards, "Structure in carbon and carbon forms " in *Introduction to carbon science*,
        H. Marsh, Ed. 1 ed. London: Butterworth & Co., 1989, pp. 1-31.

[20]   X. Bourrat, "Structure in carbons and carbon artifacts," in *The science of carbon materials*, H.
        Marsh and F. Rodríguez-Reinoso, Eds.: Universidad de Alicante, 2000, pp. 1-97.

[21]   A. Krueger, "Carbon – Element of Many Faces," in *Carbon Materials and Nanotechnology*:
        Wiley-VCH Verlag GmbH & Co. KGaA, 2010, pp. 1-32.

[22]   M. Inagaki, "Applications of polysrystalline graphite," in *Graphite and Precursors*, P.
        Delhaès, Ed. (World of carbon, Amsterdam: Gordon and Breach science publishers, 2001, pp.
        179-198.

[23]   W. H. Bragg and W. L. Bragg, *The Reflection of X-rays by Crystals* (no. 605). 1913, pp. 428-
        438.

[24]   P. Scherrer, *Nachrichten von der Gesellschaft der Wissenschaften zu Göttingen,* pp. 98-100,
        1918.

[25]   A. L. Patterson, "The Scherrer Formula for X-Ray Particle Size Determination," *Physical
        Review,* vol. 56, no. 10, pp. 978-982, 1939.

[26]   N. Iwashita, C. R. Park, H. Fujimoto, M. Shiraishi, and M. Inagaki, "Specification for a standard procedure of X-ray diffraction measurements on carbon materials," *Carbon,* vol. 42, no. 4, pp. 701-714, // 2004.

[27]   B. E. Warren, "X-Ray Diffraction Study of Carbon Black," *The Journal of Chemical Physics,* vol. 2, no. 9, pp. 551-555, 1934.

[28]   J. Biscoe and B. E. Warren, "An X-Ray Study of Carbon Black," *Journal of Applied Physics,* vol. 13, no. 6, pp. 364-371, 1942.

[29]   B. E. Warren, "X-Ray Diffraction in Random Layer Lattices," *Physical Review,* vol. 59, no. 9, pp. 693-698, 05/01/ 1941.

[30]   R. E. Franklin, "Crystallite Growth in Graphitizing and Non-Graphitizing Carbons," *Proceedings of the Royal Society A: Mathematical, Physical and Engineering Science,* Journal Article vol. 209, no. 1097, pp. 196-218, 1951-10-23 1951.

[31]   A. Oberlin, "Carbonization and graphtization," *Carbon,* vol. 22, no. 6, pp. 521-541, 1984.

[32]   M. Inagaki and F. Kang, *Materials science and engineering of carbon: Fundamentals*, 2nd ed. Waltham, MA: Elsevier Inc, 2014.

[33]   *Standard classification of coals by rank*, D388-12, 2012.

[34]   R. Menéndez, J. Bermejo, and A. Figueiras, "Tar and Pitch: Composition and application," in *Sciences of carbon materials*, F. Rodríguez-Reinoso and H. Marsh, Eds. [Alicante]: Universidad de Alicante, 2000, pp. XXXVI, 674 s., ill.

[35]   S. Madshus, "Thermal Reactivity and Structure of Carbonized Binder Pitches," Ph.D., Materials Science and Engineering, NTNU, Trondheim, 2005.

[36]   B. Rand, A. J. Hosty, and S. West, "Physical properties of pitch relevant to the fabrication of carbon materials," in *Introduction to carbon science*, H. Marsh, Ed.: Butterworth & Co., 1989.

[37]   M. Zander and G. Collin, "A review of the significance of polycyclic aromatic chemistry for pitch science," *Fuel,* vol. 72, no. 9, pp. 1281-1285, 9// 1993.

[38]   K. T. Osman, "Soil Resources and Soil Degradation," in *Soils: Principles, Properties and Management*Dordrecht: Springer Netherlands, 2013, pp. 175-213.

[39]   *Standard test method for softening point of bitumen (Ring-and-Ball apparatur)*, ASTM-D36/D36M-14, 2014.

[40]   *Standard test method for softening point of pitches (Mettler softening point method)*, D3104-14, 2014.

[41]   L. Shoko, J. P. Beukes, C. A. Strydom, B. Larsen, and L. Lindstad, "Predicting the toluene- and quinoline insoluble contents of coal tar pitches used as binders in Søderberg electrodes," *International Journal of Mineral Processing,* vol. 144, pp. 46-49, 2015.

[42]   K. L. Hulse, *Anode Manufacture*, 1st ed. Sierre, Switzerland: R&D Carbon Ltd, 2000.

[43]   D. McNeil, "The physical properties and chemical structure of coal tar pitch," in *Bituminous materials: Asphalts, Tars and Pitches*, vol. 3, A. J. Hoiberg, Ed. New York: John Wilwy & Sons, 1966.

[44]   B. Rand, "Pitch precursors for advanced carbon materials — rheological aspects," *Fuel,* vol. 66, no. 11, pp. 1491-1503, 11// 1987.

[45]   J. Lahaye, P. Ehrburger, J. L. Saint-Romain, and P. Couderc, "Physicochemical characterization of pitches by differential scanning calorimetry," *Fuel,* vol. 66, no. 11, pp. 1467-1471, 11// 1987.

[46]   H. Hatano and T. Torii, "Control of Softening Point and Glass Transition Temperature of Coal Tar Pitch," *Journal of The Japan Petroleum Institute,* vol. 42, no. 1, pp. 52-56, 1999.

[47]   M. D. Guillén, A. Dominguez, M. J. Iglesias, E. Fuente, and C. G. Blanco, "Analysis of coal tar pitch: relations between thermal behaviour and composition.," *Fuel,* vol. 75, no. 9, pp. 1101-1107, 1996.

[48]   R. W. Wallouch, H. N. Murty, and E. A. Heintz, "Pyrolysis of coal tar pitch binders," *Carbon,* vol. 10, no. 6, pp. 729-735, 12// 1972.

[49]   M. Pérez, M. Granda, R. Santamaría, T. Morgan, and R. Menéndez, "A thermoanalytical study of the co-pyrolysis of coal-tar pitch and petroleum pitch," *Fuel,* vol. 83, no. 9, pp. 1257-1265, 6// 2004.

[50]   T. Eidet and Ø. Mikkelsen, "The replacement of coal tar pitch - oppertunities and contraints," in *Silicon for the chemical and solar industry XIV*, Svolvær, Norway, 2018: The Norwegian University of Science and Technology.

[51]   R. Becker and J. Leye, "Developement and application of PAH free electrode paste," in *Silicon for the chemical and solar industry XIV*, Svolvær, Norway, 2018: The Norwegian University of Science and Technology.

[52]   J. P. Beukes *et al.*, "The use of thermomechanical analysis to characterise Söderberg electrode paste raw materials," *Minerals Engineering,* vol. 46-47, pp. 167-176, // 2013.

[53]   T. Vidvei, T. Eidet, and M. Sørlie, "Paste granulometry and soderberg anode properties," in *Light Metals 2003*, 2003, pp. 569-574: TMS.

[54]   O. Bowitz, T. Eftestol, and R. A. Selvik, "New methods for testing raw materials for anode carbon paste," in *Essential Readings in Light Metals: Electrode technology for aluminum production*, vol. 4, A. Tomsett and J. Johnson, Eds. Hoboken, NJ, USA: John Wiley & Sons, 2013, pp. 271-280.

[55]   P. M. Wilkinson, S. Ganguly, P. A. Williams, and L. J. Jensen, "Impact of electrode paste on Söderberg electrode performance," in *INFACON IX*, Quebec, Canada, 2001, pp. 510-517.

[56]   T. Bergstrøm, S. Cowley, A. C. Fowler, and P. E. Seward, "Segregation of Carbon Paste in a Smelting Electrode," *IMA Journal of Applied Mathematics,* vol. 43, no. 1, pp. 83-99, January 1, 1989 1989.

[57]   G. Andersen, R. Innvær, and B. Larsen, "Operation of Søderberg Electrodes - Methods to Avoid and Solve Electrode Failures," in *INFACON IX*, Quebec City, 2001, pp. 494-500: INFACON.

[58]   L. Olsen, A. G. Arnesen, I. Bencze, and R. Innvaer, "Temperature distribution in Søderberg electrodes," in *7th International Congress of Electroheat*, Warzaw, 1972.

[59]   R. Innvær, K. Fidje, and T. Sira, "Three-dimensional calculations on smelting electrodes," *Modeling, Identification and Control,* vol. 8, no. 2, pp. 103-115, // 1987.

[60]   R. Innvær, K. Fidje, and K. Kalgraf, "Expert system for søderberg electrodes," presented at the INFACON VII, Trondheim, Norway, 1995.

[61]   R. Innvær, K. Fidje, and R. Ugland, "Effect of current variations on material properties and thermal stresses in Søderberg electrodes," in *INFACON IV*, Rio de Janeiro, Brazil, 1986, pp. 321-330: Associacao Brasileira dos produtores de ferro-ligas.

[62]   P. Ehrburger, E. Sanseigne, and B. Tahon, "Formation of porosity and change in binder pitch properties during thermal treatment of green carbon materials," *Carbon,* vol. 34, no. 12, pp. 1493-1499, // 1996.

[63]   M. O. Sem, "The Söderberg Self-Baking Electrode," *Journal of The Electrochemical Society,* vol. 101, no. 10, pp. 487-492, October 1, 1954 1954.

[64]   C. R. Ray, P. K. Sahoo, and S. S. Rao, "Electrode management - Investigation into soft breaks at 48MVA FeCr closed furnace," presented at the INFACON XI, New Delhi, India, 2007.

[65]   B. Larsen, H. Feldborg, and S. A. Halvorsen, "Minimizing thermal stress during shutdown of søderberg electrodes," presented at the INFACON XIII, Almaty, Kazakhstan, 2013.

[66]   S. Strydom and I. McDougall, "Developements in advanced furnace control," presented at the INFACON XIII, Almaty, Kazakhstan, 2013.

[67]   B. Larsen, "Electrode models for Søderberg electrodes," presented at the Fifth international platinum Conference, Sun City, South Africa, 17-21 September 2012, 2012.

[68]   R. P. Meyjes, J. Venter, and U. V. Rooyen, "Advanced modelling and baking of electrodes," in *INFACON XII: Sustainable Future*, Helsinki, 2010, 2010.

[69]   I. McDougall, C. F. R. Smith, B. Olmstead, and W. A. Gericke, "A finite element model of a søderberg electrode with an application in casing design," in *INFACON X: Transformation through Technology*, Cape Town, South Africa, 2004, pp. 575-584.

[70]   H. A. Barnes, J. F. Hutton, and K. Walters, *An introduction to rheology* (Rheology series). The Netherlands: Elsevier science, 1989.

[71]   R. B. Bird, W. E. Stewart, and E. N. Lightfoot, *Transport Phenomena*, 2nd ed. New York, USA: John Wiley & Sons, 2007.

[72]   R. P. Chhabra and J. F. Richardson, *Non-Newtonian flow and applied rheology: engineering applications*. Amsterdam: Butterworth-Heinemann/Elsevier, 2008, pp. xiv, 518 s. : ill.

[73]   M. M. Cross, "Rheology of non-Newtonian fluids: A new flow equation for pseudoplastic systems," *Journal of Colloid Science,* vol. 20, no. 5, pp. 417-437, 6// 1965.

[74]   P. J. Carreau, "Rheological Equations from Molecular Network Theories," *Transactions of The Society of Rheology (1957-1977),* vol. 16, no. 1, pp. 99-127, 1972.

[75]   H. A. Barnes, M. F. Edwards, and L. V. Woodcock, "Applications of computer simulations to dense suspension rheology," *Chemical Engineering Science,* vol. 42, no. 4, pp. 591-608, // 1987.

[76]   A. Einstein, "Berichtigung zu meiner Arbeit: Eine neue Bestimmung der Molekuldimension," *Annalen der Physik,* vol. 34, pp. 591-592, 1911.

[77]   A. Einstein, "Eine neue Bestimmung der Molekuldimension," *Annalen der Physik,* vol. 19, pp. 289-306, 1906.

[78]   M. Mooney, "The viscosity of a concentrated suspension of spherical particles," *Journal of Colloid Science,* vol. 6, no. 2, pp. 162-170, 4// 1951.

[79]   I. M. Krieger and T. J. Dougherty, "A Mechanism for Non-Newtonian Flow in Suspensions of Rigid Spheres," *Transactions of The Society of Rheology (1957-1977),* vol. 3, no. 1, pp. 137-152, 1959.

[80]   H. A. Scheraga, "Non-Newtonian Viscosity of Solutions of Ellipsoidal Particles," *The Journal of Chemical Physics,* vol. 23, no. 8, pp. 1526-1532, 1955.

[81]   I. M. Krieger, "Rheology of monodisperse latices," *Advances in Colloid and Interface Science,* vol. 3, no. 2, pp. 111-136, // 1972.

[82]   P. Coussot, *Rheometry of pastes, suspensions, and granular materials*. Hoboken, New Jersey: John Wiley & Sons, 2005.

[83]   R. J. Farris, "Prediction of the Viscosity of Multimodal Suspensions from Unimodal Viscosity Data," *Transactions of The Society of Rheology (1957-1977),* vol. 12, no. 2, pp. 281-301, 1968.

[84]   S. Oka, "Principles of Rheometry," in *Rheology* vol. 3, F. R. Eirich, Ed. New York: Academic Press, 1960, pp. 17-82.

[85]   J. Engmann, C. Servais, and A. S. Burbidge, "Squeeze flow theory and applications to rheometry: A review," *Journal of Non-Newtonian Fluid Mechanics,* vol. 132, no. 1–3, pp. 1-27, 12/15/ 2005.

[86]   K. Tørklep, "Viscometry in paste production," in *AIME Light Metals*, Phoenix, AZ, 1988, pp. 237-244.

[87]   S. J., "Versuche über die scheinbare Adhäsion," (in English), *ANDP Annalen der Physik,* vol. 230, no. 2, pp. 316-318, 1875.

[88]   T. Bergstrøm, "Parallel plate viscometer," Report, Parallel plate viscometer, Elkem, Elkem internal, 1987.

[89]   R. B. Bird, R. C. Armstrong, and O. Hassager, *Dynamics of polymeric liquids*, 2nd ed. New york: John Wiley & sons, 1987.

[90]   G. J. Dienes and H. F. Klemm, "Theory and Application of the Parallel Plate Plastometer," *Journal of Applied Physics,* vol. 17, no. 6, pp. 458-471, 1946.

[91]   A. N. Gent, "Theory of the parallel plate viscometer," *British Journal of Applied Physics,* vol. 11, no. 2, p. 85, 1960.

[92]   J. R. Scott, "Theory and Application of the parallel plate plastometer," *Transactions of the Institution of the Rubber Industry,* vol. 7, pp. 169-186, 1931.

[93]   F. F. Nazem, "Rheology of carbonaceous mesophase pitch," *Fuel,* vol. 59, no. 12, pp. 851-858, 12// 1980.

[94]   M. L. Williams, R. F. Landel, and J. D. Ferry, "The Temperature Dependence of Relaxation Mechanisms in Amorphous Polymers and Other Glass-forming Liquids," *Journal of the American Chemical Society,* vol. 77, no. 14, pp. 3701-3707, 1955/07/01 1955.

[95]   G. W. Collett and B. Rand, "Rheological investigation of coal-tar pitch during its transformation to mesophase," *Fuel,* vol. 57, no. 3, pp. 162-170, 3// 1978.

[96]   F. F. Nazem, "Flow of molten mesophase pitch," *Carbon,* vol. 20, no. 4, pp. 345-354, // 1982.

[97]   E. Fitzer, D. Kompalik, and K. Yudatet, "Rheological characteristics of coal-tar pitches," *Fuel,* vol. 66, no. 11, pp. 1504-1511, 11// 1987.

[98]   X. Li and Q. Li, "Rheological properties and carbonization of coal-tar pitch," *Fuel,* vol. 75, no. 1, pp. 3-7, 1// 1996.

[99]   M. Eie, M. Sørlie, and K. Tørklep, "Rheological characterisation of standard and cut-back anode pitches," in *Carbon '95: 22nd biennial conference on carbon*, San Diego, California, 1995: The American Carbon society.

[100]   M. Sørlie, "The temperature stability of søderberg anode pitch," in *Light Metals*, 1984, pp. 909-921: TMS.

[101]   M. Sakai, "Viscoelastic properties of a pitch and coke-pitch disperse system," *Carbon,* vol. 17, no. 2, pp. 139-144, // 1979.

[102]   J. D. Ferry, *Viscoelastic properties of polymers*. New York; London: Wiley, 1961.

[103]   M. Sakai, "Dependence of viscoelastic properties of a carbon paste on grain size of coke," *Carbon,* vol. 17, no. 2, pp. 145-148, // 1979.

[104]   B. Larsen, J. P. M. Amaro, S. Z. Nascimento, K. Fidje, and H. Gran, "Melting and densification of electrode paste briquettes in søderberg electrodes," in *INFACON X: Transformation through technology*, Cape Town, South Africa, 2004, pp. 405-417.

[105]   J. Gunnlaugsson, J. Halfdanarson, and T. Hannesson, "On the electrode induction shield and its effects," Icelandic Alloys Ltd, Akranes1989.

[106]   *Carbonaceous materials for the production of aluminium - Calcined coke for electrodes - Determination of the electrical resistivity of granules*, 2014.

[107]   C. S. B. Nair, "Chapter 33 - Analysis of Coal Tar Pitches A2 - KARR, CLARENCE," in *Analytical Methods for Coal and Coal Products*: Academic Press, 1978, pp. 495-533.

[108]   D. K. H. Briggs, "Viscosity of coal tar pitch at elevated temperatures," *Fuel,* vol. 59, no. 3, pp. 201-207, 3// 1980.

[109]   H. Mavridis, G. D. Bruce, G. J. Vancso, G. C. Weatherly, and J. Vlachopoulos, "Deformation patterns in the compression of polypropylene disks: Experiments and simulation," *Journal of Rheology,* vol. 36, no. 1, pp. 27-43, 1992.

APPENDIX

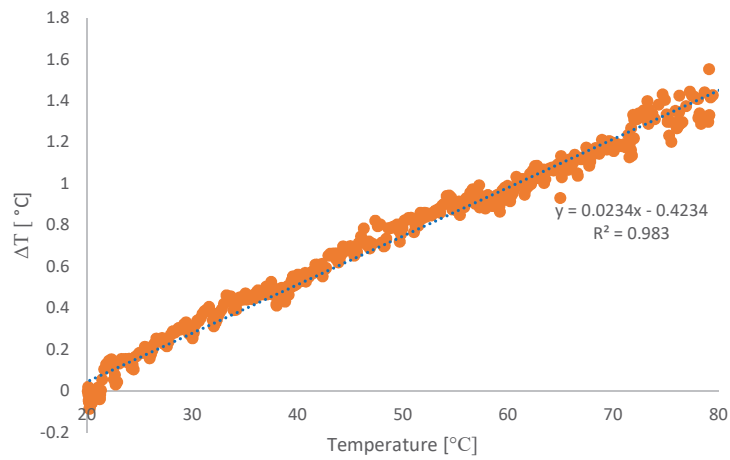## A-1   FLOW MEASUREMENT FURNACE

Figure A - 1: Temperature in the flow measurement furnace corresponds well to a K-type thermocouple in the furnace, shows that temperature measurement from the furnace is in good correspondance to the k-type thermocouple.
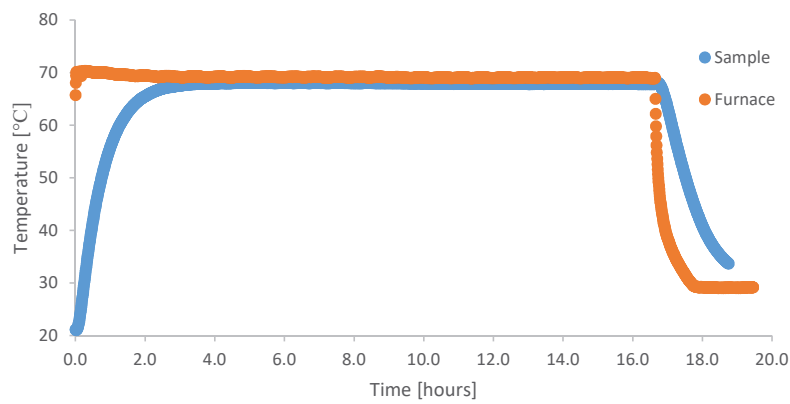

Figure A - 2 Temperature in the sample and in furnace from the sample was put in the furnace at 70° C and up to 16.5 h later when the furnace was turned off. The sample needs 4 hours to reach stable temperature.

A-2   RAW MATERIALS

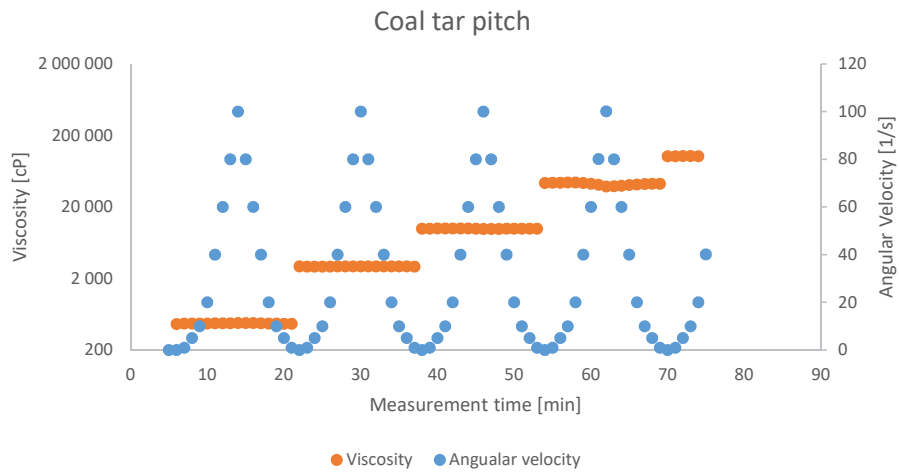Haake Rheometer data are shown in Figure A – 3 and Figure A – 4.

Figure A - 3: Viscosity and the angular velocity for coal-tar pitch in the Haake Rheometer. Viscosity is not dependent on angular velocity
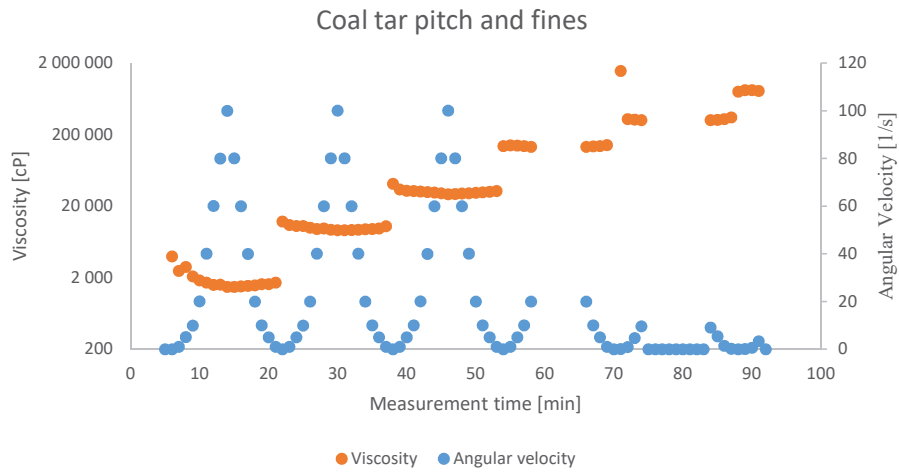

Figure A - 4: Viscosity and the angular velocity for coal-tar pitch and anthracite fines mix in the Haake Rheometer. Viscosity shows some dependence on angular velocity.

A-3   FLOW MEASUREMENTS

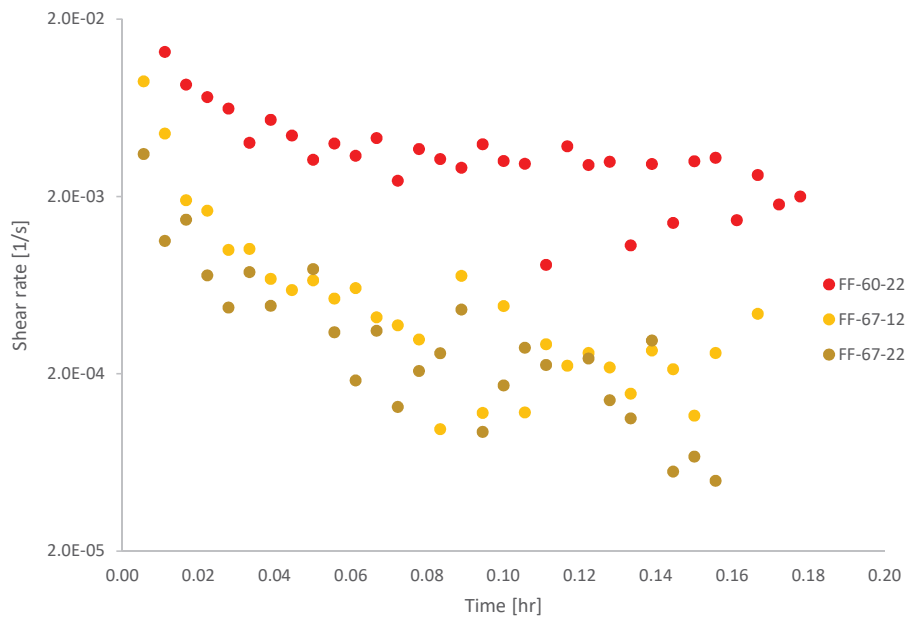Shear rates of fines fraction samples at 50° C are shown in Figure A – 5.

Figure A - 5: Shear rates of isotherm measurements at 50° C decrease during the measurements. Shear rates also decrease with increasing fines content, as compression speed is lower for the high fines content samples.

A-4   VISCOSITY DATA

Example of how viscosity data is extracted from measurement data. As there is some variation in the measurement data the mean of the 5 measurements around each temperature was used to show how apparent viscosity changes with temperature. An example of how the apparent viscosity is given in Figure A – 6, where the red rings show where apparent viscosity data is extracted.
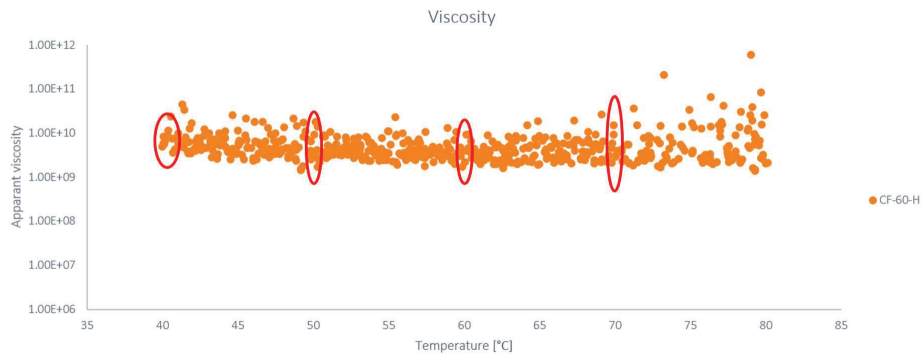

Figure A - 6: Example of how apparent viscosity varies with increasing temperature in the flow measurements of coarse particles.